



**HAL**  
open science

## Late Pleistocene-Holocene right-slip rate and paleoseismology of the Nayband fault, western margin of the Lut block, Iran

Mohammad Foroutan, Bertrand Meyer, Michel Sébrier, H. Nazari, M. Murray, Kristell Le Dortz, M.A. Shokri, Maurice Arnold, G. Aumaître, D. Bourles, et al.

### ► To cite this version:

Mohammad Foroutan, Bertrand Meyer, Michel Sébrier, H. Nazari, M. Murray, et al.. Late Pleistocene-Holocene right-slip rate and paleoseismology of the Nayband fault, western margin of the Lut block, Iran. *Journal of Geophysical Research: Solid Earth*, 2014, 119 (4), pp.3517-3560. 10.1002/2013JB010746 . hal-00992079

**HAL Id: hal-00992079**

**<https://hal.science/hal-00992079>**

Submitted on 16 May 2014

**HAL** is a multi-disciplinary open access archive for the deposit and dissemination of scientific research documents, whether they are published or not. The documents may come from teaching and research institutions in France or abroad, or from public or private research centers.

L'archive ouverte pluridisciplinaire **HAL**, est destinée au dépôt et à la diffusion de documents scientifiques de niveau recherche, publiés ou non, émanant des établissements d'enseignement et de recherche français ou étrangers, des laboratoires publics ou privés.

**Late Pleistocene-Holocene right-slip rate and paleoseismology of the Nayband fault, western margin of the Lut block, Iran**

M. Foroutan<sup>1,2,3</sup>, B. Meyer<sup>1,2</sup>, M. Sébrier<sup>1,2</sup>, H. Nazari<sup>4</sup>, A. S. Murray<sup>5</sup>, K. Le Dortz<sup>1,2</sup>, M. A. Shokri<sup>3</sup>, M. Arnold<sup>6</sup>, G. Aumaître<sup>6</sup>, D. Bourlès<sup>6</sup>, K. Keddadouche<sup>6</sup>, S. Solaymani Azad<sup>3</sup>, and M. J. Bolourchi<sup>3</sup>

<sup>1</sup>Sorbonne Universités, UPMC Univ. Paris 06, UMR 7193, Institut des Sciences de la Terre de Paris (ISTeP), F-75005, Paris, France  
Email: [mohammad.foroutan@upmc.fr](mailto:mohammad.foroutan@upmc.fr), [bertrand.meyer@upmc.fr](mailto:bertrand.meyer@upmc.fr), [michel.sebrier@upmc.fr](mailto:michel.sebrier@upmc.fr), [kristell.ledortz@gmail.com](mailto:kristell.ledortz@gmail.com)

<sup>2</sup>CNRS, UMR 7193, Institut des Sciences de la Terre de Paris (ISTeP), F-75005, Paris, France

<sup>3</sup>Geological Survey of Iran, Azadi Square, Meraj Avenue, PO Box: 13185-1494, Tehran, Iran  
Email: [foroutan@gsi.ir](mailto:foroutan@gsi.ir), [m.shokri@gsi.ir](mailto:m.shokri@gsi.ir), [shahryar.solaymani@gmail.com](mailto:shahryar.solaymani@gmail.com), [mjbolourchi@gmail.com](mailto:mjbolourchi@gmail.com)

<sup>4</sup>Research Institute for Earth Sciences, Geological Survey of Iran, PO Box: 13185-1494, Tehran, Iran  
Email: [h.nazari@gsi.ir](mailto:h.nazari@gsi.ir)

<sup>5</sup>Nordic Laboratory for Luminescence Dating, Department of Geoscience, Aarhus University, Risø DTU, DK-4000 Roskilde, Denmark  
Email: [anmu@dtu.dk](mailto:anmu@dtu.dk)

<sup>6</sup>Aix-Marseille University, CNRS-IRD-Collège de France UM 34 CEREGE, 13545 Aix-en-Provence, France  
Email: [arnold@cerege.fr](mailto:arnold@cerege.fr), [aumaitre@cerege.fr](mailto:aumaitre@cerege.fr), [bourles@cerege.fr](mailto:bourles@cerege.fr), [keddadouche@cerege.fr](mailto:keddadouche@cerege.fr)

This article has been accepted for publication and undergone full peer review but has not been through the copyediting, typesetting, pagination and proofreading process which may lead to differences between this version and the Version of Record. Please cite this article as doi: 10.1002/2013JB010746

## Abstract

The 290-km-long, Nayband strike-slip fault bounds the western margin of the Lut block and cuts across a region thought to have been quiescent during the last few millennia. C1-36 cosmic ray exposure (CRE) and optically stimulated luminescence (OSL) dating of cumulative geomorphic offsets are used to derive the long-term slip rate. The measured offsets at two sites along the fault range between  $9 \pm 1$  m and  $195 \pm 15$  m with ages from  $6.8 \pm 0.6$  ka to  $\sim 100$  ka, yielding minimum and maximum bounds of late Pleistocene and Holocene slip rates of  $1.08$  and  $2.45$  mm yr<sup>-1</sup>, respectively. This moderate slip rate of  $1.8 \pm 0.7$  mm yr<sup>-1</sup>, averaged over several earthquake cycles, is compared to the paleoseismic record retrieved from the first trench excavated across the fault. Combining the paleoseismic evidence with 18 OSL ages obtained from this trench site demonstrates the occurrence of at least four large ( $M_w \sim 7$ ) earthquakes during the last  $17.4 \pm 1.3$  ka and of two older earthquakes, one before  $\sim 23$  ka and another before  $70 \pm 5$  ka. The exposed sediment succession also indicates a significant gap at the end of MIS-2 and the beginning of MIS-1. The age of the most recent regional incision is accurately bracketed between 6.1 ka and 7.4 ka. Sediments from the last  $\sim 7$  ka contain evidence of the three younger earthquakes. Interestingly, the penultimate and antepenultimate events occurred between  $6.5 \pm 0.4$  ka and  $6.7 \pm 0.4$  ka within a time interval lasting at most 1 ka whereas the most recent earthquake occurred within the last millennium. Such an irregular earthquake occurrence suggests the seismic behavior of the Nayband fault is not strictly time dependent but possibly related to clustering. From this and taking into account the occurrence of the most recent earthquake within the last 800 years, the imminence of an earthquake along the Nayband fault cannot be discarded. Although the most recent surface-rupturing event seems to have occurred after AD

1200, this event went unnoticed in the historical records. This provides a marked illustration of the incompleteness of the historical seismic catalogs in Central Iran, challenging any assessment of regional seismic hazard without appropriate geologic and geochronological information. Large and infrequent earthquakes are characteristic of the seismic behavior of the slow-slipping strike-slip faults slicing Central and Eastern Iran. Also, the slip rates summed across Central and Eastern Iran from the Iran Plateau up to the Afghan lowlands appear in agreement with the most recent GPS data.

Accepted Article

## 1. Introduction

Central Iran experiences low GPS deformation rates [Vernant *et al.*, 2004; Masson *et al.*, 2005, 2007] and is commonly described as an area with a very low level of seismicity over the few millennia covered by the instrumental and historical seismic records [e.g., Ambraseys and Melville, 1982; Engdahl *et al.*, 2006]. Nevertheless, this presently aseismic block is cut by several north-striking, right-lateral, intracontinental active faults [e.g., Berberian, 1981; Walker and Jackson, 2004; Meyer and Le Dortz, 2007; Allen *et al.*, 2011, Figure 1a]. These dextral faults are located within a wide zone extending from the western Central Iran Plateau (Dehshir and Anar faults) to the western margin of the Lut block (Nayband and Gowk faults).

Understanding the pattern of faulting and the long-term distribution of deformation across the entire region is critical to our understanding how the deformation induced at the transition between the Zagros collision domain to the west and the Makran subduction zone to the east is accommodated in Central Iran (Figure 1a). Such information is essential for comparing the long-term strain distribution and the present-day geodetic deformation and for assessing the regional seismic hazard. Several geomorphological studies have been undertaken to estimate the long-term slip rates of several of the major strike-slip faults slicing Central Iran. The slip rates are known over a few tens of thousands to a few hundred thousand years for the Dehshir ( $1.2 \pm 0.3 \text{ mm yr}^{-1}$  [Le Dortz *et al.*, 2011]), Anar ( $\geq 0.8 \pm 0.1 \text{ mm yr}^{-1}$  [Le Dortz *et al.*, 2009; Foroutan *et al.*, 2012]), and Gowk ( $3.8\text{-}5.7 \text{ mm yr}^{-1}$  [Walker *et al.*, 2010b; Fattahi *et al.*, 2014]) faults. However, the Nayband fault slip rate of  $1.4 \pm 0.5 \text{ mm yr}^{-1}$  has been averaged over a much longer timescale since 2.25 Ma [Walker *et al.*, 2009] precluding a meaningful comparison between short-term geological ( $10^3\text{-}10^5 \text{ yr}$ ) slip rates and the geodetic displacement field. Some of these studies have been complemented by paleoseismic

investigations [e.g., *Nazari et al.*, 2009; *Fattahi et al.*, 2010; *Foroutan et al.*, 2012]. However, neither the late Pleistocene-Holocene slip rate nor the seismic behavior of the historically silent Nayband fault is known.

This paper aims to provide the critical data required to quantify the late Pleistocene-Holocene slip rate and seismic history of the Nayband fault. First we document cumulative geomorphic offsets and date them with  $^{36}\text{Cl}$  cosmic ray exposure (CRE) and optically stimulated luminescence (OSL) techniques. Then, the first paleoseismic investigation conducted along the Nayband fault is reported. The implications of these results are then discussed both for the distribution of strain and the assessment of seismic hazard in Central and Eastern Iran.

## **2. Geologic Setting and Seismotectonic Background**

The N-striking Nayband fault (Figure 1a) is the eastern edge of the Iran block that drifted northward from Gondwana in the framework of the multiphased Tethys evolution [e.g., *Berberian and King*, 1981; *Besse et al.*, 1998; *Zanchi et al.*, 2009; and recent review by *Agard et al.*, 2011 with references therein].

At the regional scale, the Nayband fault is located between two domains of contrasting topography: the relatively high Tabas block to the west in Central Iran, and the low subdued depression of the Lut block to the east in Eastern Iran. These two blocks differ both in their geology and crustal thickness [e.g., *Kluyver et al.*, 1983; *Dehghani and Makris*, 1984], suggesting that the location of the present-day Nayband fault is partly superimposed on a pre-existing fault zone.

It is commonly accepted that the present-day widespread strike-slip faulting in Iran represents the last stage of the Arabia-Eurasia collision in response to the northward

movement of the Iran block with respect to the Eurasian Afghan block [e.g., *McQuarrie et al.*, 2003]. However, there is continuing debate over the onset of strike-slip tectonics in Iran. Some authors have proposed a time range of 3-7 Ma, based on the time needed to extrapolate present-day GPS-derived slip rates to give the observed total cumulative fault displacement [e.g., *Allen et al.*, 2004; *Walker and Jackson*, 2004]. However, *Hollingsworth et al.* [2008] and *Agard et al.* [2011] proposed an earlier date of 10 Ma, based on extrapolating present-day slip rates derived from GPS to achieve the total cumulative strike-slip offsets in NE Iran and geodynamic reconstructions in SW Iran, respectively. *Meyer and Le Dortz* [2007] proposed a time range between 8-22 Ma based on extrapolating short-term geologic (Holocene) slip rates to give the total cumulative fault offsets in Central and Eastern Iran. Because of the lack of clear evidence of the total cumulative displacement along the Nayband fault, no similar estimates have been determined.

While uncertainties remain about the onset of the strike-slip tectonic regime in Central and Eastern Iran, the current regional velocity field has been well described by GPS campaigns [*Vernant et al.*, 2004; *Masson et al.*, 2005, 2007]. The overall differential motion between Central and Eastern Iran across the Lut block amounts to  $16 \pm 2 \text{ mm yr}^{-1}$  of N-S right-lateral shear at  $\sim 30.5^\circ\text{N}$  (difference between the vectors KERM and ZABO, Figure 1a). But neither the distribution of dextral shear between the eastern and western faulted Lut borders, nor the along-strike evolution of slip rate along each of the Lut borders, is well established. By contrast, west of the Lut, limited internal deformation evidenced by GPS appears to be challenged by the slip rates of faulting inside the Central Iran Plateau. Although a recent modeling [*Masson et al.*, 2014] of these GPS data evidences the possibility for some limited internal deformation west of the Lut, the summed fault-slip rates inside Central Iran exceed the limited internal strain allowed by this new modeling procedure. Indeed, late Quaternary slip rates of the Dehshir, Anar and Rafsanjan strike-slip faults are  $1.2 \pm 0.3 \text{ mm}$

yr<sup>-1</sup> [Le Dortz *et al.*, 2011],  $\geq 0.8 \pm 0.1$  mm yr<sup>-1</sup> [Le Dortz *et al.*, 2009; Foroutan *et al.*, 2012], and close to 0.4 mm yr<sup>-1</sup> [Fattahi *et al.*, 2011], respectively. The dextral slip rate of the more easterly trending Kuh Banan fault is estimated between 1 and 2 mm yr<sup>-1</sup> [Allen *et al.*, 2011; Walker and Allen, 2012] and several active thrust faults have also been documented within the interiors of the Central Iran Plateau [Walker *et al.*, 2010a], although their slip rates are not yet determined.

While the historical and instrumental record does not indicate significant seismicity in the interior of the Central Iran Plateau, several earthquakes have occurred close to or along the eastern border with the Lut desert (Figure 1b and Table 1). North of 33°N, the destructive Tabas earthquake of  $M_w$  7.3 occurred in a region hitherto known to have been quiescent for the last millennium [Berberian, 1979a, 1979b]. This earthquake remained the largest instrumentally recorded event in Iran [Walker *et al.*, 2003, 2013] until the recent (2013 April 16),  $M_w$  7.7 Khash intermediate-depth earthquake, which struck the Makran region [Barnhart *et al.*, 2014]. The Tabas earthquake, which resulted in approximately 20,000 deaths, combined thrust and dextral motions along NNW-striking faults; these may account for a transpressive tectonic regime at the northwestern termination of the N-striking Nayband fault.

Another sequence of earthquakes with associated surface breaks has taken place south of 30.5°N, where NNW-striking sub-parallel thrusts of the Shahdad fault system and the strike-slip Gowk fault are thought to achieve slip partitioning at the southeastern tip of the Nayband fault. The Gowk fault has hosted five destructive earthquakes during a seventeen-year period, possibly resulting from stress transfer [Nalbant *et al.*, 2006]. The sequence started in 1981 with the two destructive earthquakes of  $M_s$  6.7 (Golbaf) and  $M_s$  7.1 (Sirch) on June 11 and July 28, respectively [Berberian *et al.*, 1984]. Both ruptured the Gowk fault to the surface with an overall 70-km-long fault break interrupted by a 10-15-km slip gap further filled during the 1998 March 14 Fandoqa earthquake [Berberian *et al.*, 2001]. The Fandoqa

earthquake of magnitude  $M_w$  6.6 is also known to have re-ruptured a significant portion of the Sirch break and to have triggered slip on the Shahdad thrusts [Berberian *et al.*, 2001; Fielding *et al.*, 2004]. The Fandoqa event was followed by a smaller ( $M_w$  5.4) event, the Chahar Farsakh earthquake, which took place on November 18 of the same year and produced minor surface cracking over 4 km. The south Golbaf  $M_s$  5.7 earthquake took place in 1989 and produced a 19-km-long surface break distributed on two sub-parallel fault strands [Berberian and Qorashi, 1994].

An additional event with magnitude  $M_w$  6.4, the Dahuiyeh event, occurred some 90-km NW of the Gowk fault and 100-km west of the Nayband fault, within the Central Iran Plateau. The event struck the city of Zarand on February 22, 2005 and produced a 13-km long, thrust fault break splaying off the Kuh Banan strike-slip fault [Talebian *et al.*, 2006].

Thus, the Nayband fault seems the only portion of the western Lut border that has not been seismically active in the last few millennia [Ambraseys and Melville, 1982; Ambraseys and Jackson, 1998; Berberian and Yeats, 1999; Engdahl *et al.*, 2006, Figure 1b]. Although the long-term slip rate of the Nayband fault averaged over the entire Quaternary is suggested to be of the order of  $1.4 \pm 0.5$  mm yr<sup>-1</sup> [Walker *et al.*, 2009] neither its short-term slip rate nor its paleoseismic history are known.

The Nayband fault runs for some 290 km along the western margin of the Lut block (Figure 1). The overall fault trace is straight and linear but five first-order segments can be nonetheless identified on the basis of main structural discontinuities such as bend, step over and strike variations.

The northern termination of the linear fault trace lies close to 33°N, where it joins with the E-striking south-dipping Cheshmeh Rostam thrust fault and the Tabas fault system (Figure 1b). The northernmost fault segment strikes N172°E for 78 km and cuts across

Eocene volcanic rocks as well as Pliocene-Quaternary deposits. Near 32.37°N, east of the Nayband village, the northern segment bends westwards and ends east of Dig-e Rostam, where the fault trace takes a right step. The second segment strikes N178°E and continues for 65-km to 31.7°N. There, the fault trace takes another right-step, defining the boundary with a third segment cutting through Neogene sediments, Quaternary alluvial fans and recent playas. This segment has an average strike of N175°E and a length of about 40 km to the north of the Gandom Berian basaltic plateau (Figure 1b); it forms the eastern edge of a 4-km wide pull-apart basin [Walker *et al.*, 2009]. The western edge of this basin is formed by the beginning of a fourth, 50-km-long, N178°E striking segment cutting the Gandom Berian basalts along its northern portion and bounded by a parallel secondary thrust along its southern portion. Farther south, where a secondary thrust dies out at about 31°N, the main strike-slip fault veers eastwards into a fifth segment. This 65-km length southernmost segment has an average strike of N173°E and runs parallel to the mountain front up to the northeast of the Chahar Farsakh village.

The next section reports the observations collected from the second segment of the Nayband fault; geomorphic features, cosmogenic and luminescence dating are then used to determine the late Pleistocene-Holocene slip rate.

### **3. Morphological Offsets and Slip Rate Estimate**

The use of morphological offsets to determine the long-term slip rate on an active fault requires datable morphologic features that were first displaced by the fault motion(s) and then preserved over the observable displacement interval [e.g., Sieh and Jahns, 1984; Weldon and Sieh, 1985; Peltzer *et al.*, 1988]. We document offset alluvial fans, terraces, and stream channels at two sites about 5 km apart along the second segment of the Nayband fault, and

discuss the ages of these geomorphic markers using  $^{36}\text{Cl}$  CRE and OSL dating to derive the slip rate averaged over the late Pleistocene-Holocene.

### 3.1. Site North

Site North is located about 26 km south of the Dig-e Rostam hot springs (Figures 1b and 1c). This site was presented first by *Wellman* [1966] as a sketch map based on aerial photos showing several dextral offset streams along the fault (see Figure 2G of *Wellman* [1966]). Smooth hills made of Triassic rocks outcropping to the west of the fault are overlain by Neogene piedmont sediments outcropping mostly east of the fault (Figure 2). The location of the fault is well constrained both on the Quickbird imagery and in the field by a clear, linear, single trace that offsets several rivers, the longest of which are more displaced than the smallest gullies (Figures 2 and 3a). The largest hectometer-scale offsets are associated with two major rivers that incise into the Triassic shales, sandstones and limestones west of the fault. East of the fault, both rivers feed prominent alluvial fans nested within Neogene marls interbedded with conglomerate strata. The fans and the overbank surfaces display a dark hue on the Quickbird imagery highlighting the dextral along-fault offsets of the river beds (Figures 2 and 3a).

A southwards flowing tributary joins the main overbank surface of the northernmost river, and as a result the streambed widens as it approaches the fault so that the actual upstream width, under confluence, is larger than the original one. Similar situation can be observed on the next major river farther south. Thus, using the widths of the valleys to determine the offsets will necessarily overestimate the true uncertainties. As the offset streams are generally deeply incised, projecting the upstream and downstream gully orientations on the fault trace permits to determine the two piercing points defining the offset. The possible variations of these orientations provide the offset uncertainty. Therefore, the

intersections of the upstream and downstream right banks of the northern stream with the fault define reliable piercing points that indicate a right-lateral offset of  $420 \pm 50$  m (Figure 2). Farther south, the next prominent river has been offset by  $180 \pm 20$  m. These large rivers are no longer feeding the fans they originally emplaced so that these offsets are much older than the recent incision of the latest deposits filling the valleys. Recent incision has resulted in piracy that disconnected the alluvial fans from their upstream tributaries. The piracy P1 that disconnects the northern fan occurred east of and close to the fault trace while that of the southern fan, P2, occurred upstream and west of the fault. The abandonment of the fans is therefore coeval with the beginning of incision by the present-day drainage network of the infilling of the wide flat-floored valleys and related outlet fans. This abandonment (and so the last incision of the fans) is interpreted to be recent as the surfaces of the fans are characterized by a subdued bar-and-swale morphology and a poorly developed desert pavement [e.g., *Frankel and Dolan, 2007*]. Such recent incision relates to the widespread incision documented by *Meyer and Le Dortz [2007]* for the Central Iran Plateau. They interpreted this regional incision to be synchronous and assigned it to the onset of the Holocene.

Several smaller offsets of intermittent streams and channels are preserved. There are many intermittent river-courses that collect gullies draining small catchments within the Triassic rocks; where these cross the fault they incise narrow gorges into the soft and easily erodible Neogene marls, and as a result numerous sharp offsets are visible along the fault. These offsets, ranging between 10 and several tens of meters, are described from the North towards the South. The northernmost is preserved along a tributary close to the outlet of the northern abandoned fan with a sharp offset of  $40 \pm 5$  m (Figures 2, 3a, 3b and 3c). Farther south, a narrow stream is incised  $\sim 15$  m into the poorly-consolidated Neogene marls mantled by remnants of Quaternary colluviums. This intermittent stream is right-laterally offset by

about  $25 \pm 5$  m (Figures 2, 3b and 3d). The smallest cumulative geomorphic offset observed along the fault occurs 50 m to the south of the former offset-stream. There, a very narrow gully is incised by  $\sim 3.3$  m into both the Neogene sediments and a thin alluvial veneer that previously fed the southern fan; this gully is right-laterally offset by  $9 \pm 1$  m (Figures 2, 3b, 3e and 3f). Farther south and a little west of the outlet of the southern alluvial fan, another  $25 \pm 5$  m right-lateral sharp offset on an ephemeral gully is well preserved (Figures 2 and 4a). A larger offset of  $60 \pm 5$  m on an intermittent channel incising obliquely to the fault strike is seen 250 m farther to the south (Figures 2 and 4b).

### 3.2. Site South

This site is located about 5 km south of the site North (Figures 1c and 5a). Two parallel fault strands delineate a 100-m-wide, 1-km-long releasing step-over cutting through the Neogene deposits, Pleistocene and Holocene alluvial fans, and active streams (Figure 5). For most of its length, the trace of the eastern fault strand (EFS) runs near the base of a  $\leq 10$ -m high west-facing steep slope between Neogene marls and Quaternary alluvial deposits. The trace of the western fault strand (WFS) runs at the base of a 30-40-m high, east-facing slope and separates Neogene marls ( $< 10^\circ$  northwest-dipping) from Quaternary deposits. While the trace of the EFS vanishes to the south, the trace of the WFS merges with that of the EFS some 250 m north of the site. The low-relief depression between these two fault strands is filled mainly with Pleistocene alluvial deposits (Figure 5) that have been eroded by two major E-W intermittent streams.

The northern stream (R0) flows into a 50-m-wide valley and trends N110°E west of the fault. Within the fault zone, R0 is deflected to the north into a narrow, N100°E, 10-20-m wide, entrenched valley. The present downstream portion of R0 is building a young alluvial fan at its eastern outlet, close to 610-m above sea level (asl) (Figures 5a and 5b). The next

major stream flows some 500 m to the south and does not show any discernible offset or deflection across the fault zone. A recent fan is building at the outlet of that southern stream along the WFS. This recent fan merges with several overbank beds that feed a broader alluvial fan the apex of which lies ~610-m asl. Between these two major streams the topography is hilly on both sides of the fault zone, and several abandoned or intermittent channels and regressive gullies have incised the Neogene marls.

To the east of the EFS trace, two well-preserved hanging channels (R1 and R2) are incised into the Neogene marls (Figures 5b and 6). These two paleochannels appear as wind-gaps as they have been beheaded by the EFS and further incised by the regressive erosion of some of the many small gullies draining the Neogene marls east of the fault zone. As seen in Figures 5 and 6, the R1 wind-gap is hanging 4-5 m higher than the younger, currently abandoned, alluvial surface to the west. The beheaded streambed of the R1 wind-gap is also a little higher and wider than the R2 wind-gap to the south. The beheaded channels R1 and R2 are much too wide to have been only carved by the small rills now incising them. None of the current intermittent channels standing to the west of the fault between R0 and the next southern major river appears large enough to have fed R1 (Figures 5 and 7). Allowing for dextral motion along the fault zone, the closest upstream river with an appropriate size to match downstream with R1 is R0. The offset between the course of the northern stream R0 on the western side of the fault zone and the course of the stream R1 on the eastern side of the fault zone, shown in Figure 7, amounts to  $195 \pm 15$  m (Figure 8).

The following sections present and discuss the cosmogenic and luminescence dating results that constrain the ages of the displaced geomorphic features at the two sites described above.

### **3.3. Chronological Tools: Cosmic Ray Exposure and OSL Dating**

Although geomorphic features in arid regions are well preserved and offer the possibility to document the amount of fault slip, the scarcity of organic material limits severely the use of radiocarbon dating (which in any case can only be used to date the last ~45 ka). In order to obtain ages for the offset geomorphic features, we undertook both  $^{36}\text{Cl}$  CRE and OSL dating of the abandoned alluvial surfaces. Cl-36 can be produced by two different mechanisms, cosmic ray interactions and radiogenic production by disintegration of U and Th. The analytical procedure and the calculations of cosmic ray exposure ages are identical to that extensively described by *Le Dortz et al.* [2011]. Following a methodology applied for the neighboring Dehshir and Anar faults in Central Iran [*Le Dortz et al.*, 2009, 2011, 2012], 24 surface samples were collected to determine the CRE ages of alluvial surfaces. Since Jurassic Limestone is the dominant source of material in the area, we collected calcite rich pebbles and measured their concentration of *in-situ* produced  $^{36}\text{Cl}$  cosmogenic nuclide. The basic information required for CRE age calculations is summarized in the captions to Tables 2 and 3; these tables provide the concentrations of *in-situ* produced  $^{36}\text{Cl}$  with the corresponding 'no-erosion' ages (Table 2) and the chemical composition of the carbonate samples (Table 3).

In addition, OSL is used to determine the time elapsed since the last exposure of sediments to sufficient sunlight to reset any latent luminescence signal, and so to determine the burial age of the target material. During subsequent burial, energy (dose) is absorbed from environmental ionising radiation, and some of this energy is stored in the form of electrons trapped in meta-stable states. This energy can be released by stimulation with visible light, and some of the released energy is emitted in turn as luminescence [e.g., *Aitken*, 1998]. By calibrating this luminescence in terms of dose using an artificial source of radiation it can be used as a measure of the dose, usually termed the equivalent dose,  $D_e$ . The rate of absorption of energy (dose rate) can be determined from a knowledge of the radioactivity of the surrounding sediment, the water content (water absorbs some energy and so reduces the dose

rate), and from the burial depth (which affects the dose rate from cosmic rays). All these issues are discussed by *Aitken* [1985]. A review of the precision and accuracy of quartz OSL dating on various types of sediment (and using similar analytical protocols to those used here) is given by *Murray and Olley* [2002].

Reliable OSL dates require that any latent OSL signal be sufficiently well bleached before deposition and that apparent residual dose is small compared to the subsequent burial dose. Our equivalent doses were determined using large multi-grain aliquots; because of the inevitable effects of averaging, it is very unlikely that there is any useful information on the degree of bleaching available in an examination of the dose distributions of any particular sample [*Li*, 1994; *Olley et al.*, 1999; *Wallinga*, 2001]. However, some of the equivalent doses here are smaller than, or comparable to, the average of those found in modern, recently-deposited non-aeolian sediments (typically  $2.4 \pm 0.6$  Gy;  $n=67$ , according to the recent summary by *Murray et al.* [2012]). This, coupled with the stratigraphic consistency and the agreement between paired samples (section 4.3), is taken as evidence that, in general, these samples are unusually well-bleached for water-lain material. One unit provides a pair of samples that are exceptions to this (section 4.3, unit 8w, samples NT-XV and NT-XXI) but this unit was identified as atypical in the field (see section 4.2) and does not invalidate our general conclusion. The analytical procedure and the relevant luminescence measurements are summarised in Table 4, together with sample depth and assumed average burial water contents.

### 3.3.1. $^{36}\text{Cl}$ CRE Dating

At the site North, two abandoned alluvial surfaces of the last fan system (see section 3.1) were targeted for  $^{36}\text{Cl}$  sampling (Figure 2, right panel). Six carbonate samples (S13 to S18, see Figure 2 for locations) were collected from the abandoned alluvial surface deposited by

the northern stream, close to the piracy P1 along the valley that is offset by  $420 \pm 50$  m. These provide CRE ages ranging between  $15.9 \pm 1.4$  ka and  $80 \pm 7$  ka (Table 2 and NF on Figure 9). About 800 m farther south, 6 samples (S19 to S24) were collected on the surface emplaced by the southern stream that is offset by  $180 \pm 20$  m. They provide CRE ages ranging from  $24 \pm 2$  ka to  $221 \pm 23$  ka (Table 2 and SF on Figure 9). For both alluvial surfaces, the surface samples display scattered  $^{36}\text{Cl}$  concentrations, hence variable CRE ages. Such scatter suggests the alluvial sampled surfaces are young so that a variable inheritance component predominates over the *in-situ*  $^{36}\text{Cl}$  concentrations, as already observed for alluvial terraces sampled in Central Iran, along the Anar and Dehshir faults [Le Dortz *et al.*, 2009, 2011]. At the Nayband sites, the limited thickness (1.5 m) of the fan conglomerates prevented the sampling of a depth profile deep enough ( $\geq 4$  m) to determine the denudation rate and to apply the rejuvenation profile procedure and so determine the range of inheritance and maximum exposure ages [Le Dortz *et al.*, 2012]. Notwithstanding the inheritance, the outliers (i.e., the oldest samples) can be discarded and weighted mean CRE ages calculated for each fan surface. In this case, weighted mean CRE ages are  $29 \pm 18$  ka (S14-17) and  $28 \pm 8$  ka (S19, S21, S22) for the northern and southern surfaces, respectively (Figure 10). However, these weighted mean ages show very large uncertainties, agreeing with multiple peak distribution for the ages of the northern fan surface. In such a case, several studies [e.g., Mériaux *et al.*, 2005; Vassallo *et al.*, 2007; Le Dortz *et al.*, 2009, 2011] have shown that the average weighted mean age is generally misleading and hence the best age approximation is given by the youngest sample. Therefore, instead of  $\sim 28$  ka, we selected  $15.9 \pm 1.4$  ka for the northern surface and  $24 \pm 2$  ka for the southern one, respectively (Figure 9), as the best CRE approximation for the abandonment ages of the lower fans at the site North. Since the relative elevation above the active network and the surface roughness of the two neighboring fans are similar, they are more likely coeval. Considering the two fans are coeval and keeping in mind

that the youngest sample on a surface may still incorporate some inheritance [Le Dortz *et al.*, 2009], one may retain a CRE abandonment age of at most  $\sim 16$  ka for both fans, hence postulate that the youngest of the sampled pebbles on the southern fan contains more inheritance than that on the northern one. Following this argument, the last fan system aggraded during the LGM (i.e., marine isotope stage 2, MIS-2).

At the site South, two alluvial surfaces deposited during the evolution of the drainage network (Figure 8) are preserved (Figure 5). Fragmentary remnants of the older surface overlie the Neogene marls, some 10-20 m above the active overbank surfaces (Figure 6). The younger surface is well preserved as a lower alluvial terrace and stands only 2-3 m above the active overbank surfaces.

Six samples (S7 to S12) were collected on this well-preserved lower surface. As for the site North, where the alluvial surfaces stand  $\sim 2$  m above the active streams, the scatter in  $^{36}\text{Cl}$  concentrations is significant. The corresponding CRE ages range from  $22.6 \pm 1.8$  ka to  $121 \pm 11$  ka (Table 2 and WF on Figure 9). It seems clear that the two highest  $^{36}\text{Cl}$  concentrations (S7 and S11) are outliers and these are discarded; the resulting weighted mean CRE age for the lower surface is  $29 \pm 13$  ka. Accounting for variable inheritance as for the lower fan surfaces at the site North, one may rather consider that the youngest pebble ( $22.6 \pm 1.8$  ka) provides the best estimate for the abandonment of the surface and so conclude this lower alluvial terrace also aggraded during the LGM.

The older fan stands on the Neogene marls; it was deposited by the northern stream R0 and subsequently abandoned when R0 started to incise its deposits (Figure 8, stages 1a and 1b). The present remnants of the old alluvial surface form a thin ( $\sim 1$ -m thick) layer of cobbles and small boulders (50 cm in diameter) mainly derived from limestone. The material on the surface also includes a few boulders of sandstone and cobbles of reworked

conglomerates from the Neogene deposits. We collected six limestone pebbles (S1-S6) from the best-preserved patches of the old alluvial surface (Figure 6) for the measurement of  $^{36}\text{Cl}$ . Assuming negligible denudation and no inheritance, the  $^{36}\text{Cl}$  CRE ages range from  $58 \pm 5$  ka to  $92 \pm 8$  ka (Table 2 and EF on Figure 9), these are less scattered than those measured on the lower surfaces at the sites North and South and do not suggest significant inheritance (Table 2). Assuming no inheritance and no erosion the two youngest pebbles (S3 and S5) are taken as outliers and the resulting weighted mean age of the surface is  $89 \pm 4$  ka. Alternatively, one may consider the possibility for erosion. Although previous CRE studies have demonstrated that denudation rates are very low ( $\leq 1\text{m/Ma}$ ) on well-preserved alluvial surfaces in Central Iran [Le Dortz *et al.*, 2011, 2012], erosion could be locally higher on less-preserved surfaces. Considering that the Neogene marls are poorly consolidated (and so prone to rapid erosion) and that the topography at the site South is significantly dissected due to the presence of a regional E-facing slope separating the Tabas block from the Lut block, erosion is likely to be locally significant. This has probably been the case for the few remaining outcrops of the higher terrace. Indeed, they result from an almost complete dissection of the old alluvial surface, the remains of which appear as narrow horizontal patches standing 10-20 m above the present-day network. Thus, it is possible that the initial surface of the higher terrace was significantly affected by erosion and subsequent rejuvenation; this would explain the presence of the two younger outliers. To allow for such rejuvenation, the age of the oldest pebble should be considered a proxy for the true age of the alluvial surface [e.g., Brown *et al.*, 2005]. In that case, the oldest possible CRE age of the old surface topping erodible marls should be about 100 ka (Figure 9).

Although the limited thickness of conglomerates at both sites precluded the sampling of a depth-profile and thus prevented the estimation of the minimum range of inheritance [Le Dortz *et al.*, 2012] comparing the surface CRE ages with near-surface OSL ages from the

same alluvial surfaces would provide an estimate of the maximum possible range of inheritance for each surface sample. This is particularly useful if the abandonment age of young alluvial surfaces in arid environments is to be constrained; such surfaces in Mongolia [Vassallo *et al.*, 2007] and Central Iran [Le Dortz *et al.*, 2011] are known to have significant variable inheritance.

### 3.3.2. OSL Dating

At site North, three OSL samples were collected within the last alluvial fan system to better constrain the abandonment ages of the alluvial surfaces incised by young rills and gullies (Figure 2). The first sample, NA-1, was collected half a kilometer west of the fault trace within the upstream end of alluvial deposits, from a fan apex emplaced by the southern stream that fed the major fan east of the fault trace. The sample comes from the 3-m high riser of a young and still active intermittent channel associated with the piracy P2 by a south-flowing stream. This sample was extracted from a loose, fine sandy lens at 174 cm below the fan surface using stainless steel tube (6 cm x 25 cm); both ends were sealed and covered immediately after sample extraction, using both aluminum foil and black tape.

The second sample, NA-2, was collected some 15 m east of the fault trace, nearby an active channel, and close to the outlet of the southern abandoned alluvial fan (Figure 2). Because there was no suitable exposure by the riser of the young channel incising the abandoned fan surface, a pit was directly excavated into the surface of the fan. The sample was collected from the bulk of coarser sediments containing loose, fine-grained sediments following the procedure described below and designed specifically for the arid environments [e.g., Rizza *et al.*, 2011a, 2011b]. The material was extracted at 47-cm depth, within stratified, poorly compacted, sub-angular, fine to very coarse pebbles (1 to 5 cm) within a fine to coarse sandy matrix. To prevent light-induced effects on the OSL signal during the

material extraction, we covered the pit with several layers of dark thick tarpaulins and plastics. Then, in complete darkness, the targeted sampling area (15 cm in diameter) was cleaned by removing around 10 cm of the materials exposed to the sunlight during the pit digging. About 1 kg of the bulk sediment, including silts to coarse pebbles (<3 cm) was collected from this cleaned sediment face. The sampled material is collected in a thick-black plastic bag, doubled by several additional black bags and wrapped with a black tape before exposing to light. This process avoided an unacceptable light exposure during sampling, and preserved as much as possible the field water content.

The third sample, NA-3, was collected close to the fault and nearby the piracy P1 adjacent to a recent and still active E-W flowing channel (Figure 2). As for the NA-2 extraction, a pit was excavated into the surface of the abandoned alluvial fan, some ten meters east of the fault trace. Using the same procedure as above, the sample was extracted at 50-cm depth, within a stratified unit containing fine to coarse pebbles (0.5 to 3 cm) in a fine to coarse sandy matrix.

The NA-1 ( $7.7 \pm 0.5$  ka) and NA-3 ( $6.8 \pm 0.6$  ka) ages are indistinguishable and suggest the most recent aggradation of the last fan system ceased some 6 to 7 ka ago. In contrast, NA-2 has an OSL age of  $22 \pm 3$  ka; in the absence of any evidence for incomplete bleaching (see section 3.3) this would indicate that the aggradation of the last fan system occurred in at least two different episodes: an older one during the LGM, as suggested by the  $22 \pm 3$  ka age and a younger one during the mid-Holocene, as indicated by the  $6.8 \pm 0.6$  ka and  $7.7 \pm 0.5$  ka ages. Hence, the OSL results suggest that at least two periods of channel incision occurred: one at around the LGM and another in the mid-Holocene, the later interpreted as the actual abandonment of the surface of the recent fans.

### 3.4. Interpretation and Possible Range of Slip Rate

At site North, two  $25 \pm 5$  m offset of ephemeral gullies incised within Neogene marls (orange-shaded pedimented surfaces in Figure 2) have been preserved. These  $25 \pm 5$  m offsets are larger (and so hence older) than that  $9 \pm 1$  m offset of a narrow gully incised within the young alluvial fan surface nested within the Neogene marls. The  $9 \pm 1$  m offset has accumulated after the abandonment of that young alluvial surface and its subsequent incision. This youngest surface is too thin close to the  $9 \pm 1$  m offset to be dated by OSL or confidently sampled for cosmogenic analysis. However, we dated a lateral equivalent of this surface at three locations: two (NA-1 and NA-2) within the same catchment and one (NA-3) within the next catchment to the North. Considering that the ages of NA-1 and NA-3 correspond to the most recent fan aggradation prior to incision, they provide a maximum age for the abandonment of the surface. Therefore, the  $9 \pm 1$  m offset cannot be older than NA-3 ( $6.8 \pm 0.6$  ka), the youngest of these two samples, and the slip rate cannot be less than  $1.08 \text{ mm yr}^{-1}$  ( $8 \text{ m}$  in  $7.4 \text{ ka}$ ). It is very unlikely that the neighboring and larger  $25 \pm 5$  m offsets would have accumulated during the same time span as a consequence of along-strike, slip variation. Rather, the larger offsets should have started to accumulate before the most recent fan aggradation and one can thus derive a maximum bound on the slip rate of  $4.16 \text{ mm yr}^{-1}$ , by dividing the maximum amount ( $30 \text{ m}$ ) of the offset by the youngest possible age of the oldest sample of the last phase of fan aggradation ( $7.2 \text{ ka}$ , the youngest possible age of the sample NA-1, collected within the young inset alluvial sediment). Conversely, dividing the minimum amount ( $20 \text{ m}$ ) of that offset by the oldest possible age of the most recent alluvial fan ( $25 \text{ ka}$ , oldest possible age of the sample NA-2) provides a minimum bound on the slip rate of  $0.80 \text{ mm yr}^{-1}$ .

Alternatively, one may contemplate that the youngest CRE age of  $15.9 \pm 1.4$  ka (sample S14), is a proxy for the penultimate phase of aggradation of the youngest fan. Assuming the  $25 \pm 5$  m offset postdate that penultimate aggradation yields a minimum slip rate of  $1.15 \text{ mm yr}^{-1}$  (20 m in 17.3 ka, oldest possible age of the youngest pebble on the surface). This estimate of the minimum slip rate is less robust than the former estimates using OSL dates. One has therefore to retain  $1.08 \text{ mm yr}^{-1}$  as a safe minimum slip rates (upper value of the two minimum estimates previously determined). This indicates that the  $9 \pm 1$  m offset and the incision of the youngest alluvial fan are a little younger than 7.4 ka.

At the site South, the right-lateral offset between the course of the active stream R0 to the west and the R1 wind-gap to the east of the fault zone amounts to  $195 \pm 15$  m (see section 3.2 and Figure 8). Assuming negligible denudation, combining the largest possible offset (210 m) with the youngest possible age of the weighted mean CRE age (86 ka) as a proxy for the abandonment age of the old alluvial surface at this site yields a maximum slip rate estimate of  $2.45 \text{ mm yr}^{-1}$ . Accounting for some denudation and provided one would not find an older pebble than S4, one would consider the oldest CRE age possibility of S4 (100 ka) as the abandonment age of the alluvial surface and the smallest possible offset (180 m) to infer a minimum slip rate of  $1.80 \text{ mm yr}^{-1}$ . Because the small thickness of alluvial deposits did not allow the estimation of the amount of denudation by CRE depth-profiles, one cannot discard the possibility that the surface is older than sample S4 and so the former value cannot be taken as a safe estimate of the minimum slip rate.

In summary, the geomorphic offset markers and their corresponding possible ages indicate the slip rate ranges between  $1.08$  and  $2.45 \text{ mm yr}^{-1}$ , resulting in a mean slip rate on the order of  $1.8 \pm 0.7 \text{ mm yr}^{-1}$  over the last 100 ka (Figure 11). One can notice that, combining the right-lateral offset of  $40 \pm 5$  m preserved along the tributary incising within the poorly-consolidated, pedimented Neogene marls at the site North (Figures 2, 3a, 3b and

3c) with the oldest available age for the young alluvial surfaces ( $22 \pm 3$  ka, sample NA-2) would provide a slip rate of 1.4 to 2.4 mm yr<sup>-1</sup>, consistent with the range of  $1.8 \pm 0.7$  mm yr<sup>-1</sup>.

#### **4. Identification of Past Earthquakes on the Nayband Fault**

The instrumental and historical seismic records [Ambraseys and Melville, 1982; Ambraseys and Jackson, 1998; Berberian and Yeats, 1999; Engdahl et al., 2006] do not mention any destructive earthquake in the vicinity of the Nayband fault (Figure 1b). However, the sharpness of the fault trace across the recent deposits, and the morphological evidence for recent cumulative offset suggest recent, Holocene activity. The following sections document small dextral offsets and relate them to several paleoearthquakes evidenced within a paleoseismic trench.

##### **4.1. Geomorphic Setting of the Trench Site**

South of 31° 57'N, the trace of the fault segment NA2 no longer follows the boundary between basement rocks and Neogene sediments (Figure 1c). The fault extends in a depression with subdued relief, cutting across late Pliocene-Pleistocene deposits as well as Holocene alluvial fans and recent ponds (Figures 1c and 12). The overall fault trace is linear with a few compressional step-overs and several right steps favoring local extension and sediment ponding. Thin layers of silts and clays that often cover the ponds are seen as white hues on the Quickbird imagery. One such pond is located close to 31° 54'N at some 550 m asl and is positioned across a 80-m-wide releasing step-over (Figure 13a). The western and eastern borders of this depression are outlined by two fault scarps, facing each other (Figure 13b).

To the north, a compressional step-over within late Pliocene-Pleistocene alluvial fan conglomerates bounds two narrow ridges up to 604 m asl near 31° 56'N. The step-over is

made of late Pliocene-Pleistocene deposits uplifted and folded. Along the western foothill of the ridges, well-exposed outcrops show layers dipping 15 degrees to the northwest. The uplifted alluvial fan conglomerates of the core of the ridge have been subsequently eroded and incised. The latest incision together with regressive erosion processes have resulted in the formation of small rills and gullies distributed along the fault (Figure 14). These recent channels are incised into older and abandoned alluvial surfaces and have recorded small amounts of right-lateral offset ranging from 3 to 16 m (Figure 15). The offset rills were measured both in the field with a tape and on the high-resolution topographic map obtained by a Real-Time Kinematic (RTK) survey devoted to a systematic survey of offset rills and gullies. The resulting high-resolution topographic map allows one to restore the offset channels to simple linear patterns along the fault. As seen in Figure 15a, by extrapolating the recent channel thalwegs on both sides of the fault to their intersections with the fault the offsets of channels A, B, C and D amount to 3, 3.5, 4 and 10 m, respectively. Furthermore, several other gullies and channels illustrate cumulative dextral offsets along the fault trace on the order of 6, 10, 13 and 16 m (Figures 15b-15d).

Farther south, near 31° 55'N, a small channel has been right-laterally offset at the fault by 16 m (Figure 16). A larger though still ephemeral stream is incised into both the alluvial fan surface and the 2 m-high, east-facing scarp; this channel has been offset by  $35 \pm 5$  m. About 300 m farther south, a small dry pond, approximately 110-m long and 50-m wide, has formed along the fault (Figures 12 and 16). The ephemeral streams to the south and southeast of this dry pond are the primary sources of the sandy and pebbly material infilling this small depression. Smaller gullies surround the pond, draining surficial runoff and delivering the silt and clay materials mantling the pond. This pond is bounded to the west by older and higher alluvial fan surfaces as well as by the round-shaped termination of a fairly flat-topped ridge, gently inclined to the east and composed of late Pliocene-Pleistocene gravelly alluvial

deposits. This ridge, which is about 6 m higher than the pond, may be interpreted as the northern part of a ~600-m wide shutter-ridge that has deflected the pond outlet northward by some 250 m (Figure 16c). This outlet extends northward along a narrow, 10-m-wide channel, and veers westward to bypass the shutter-ridge and reach the active flood plain. The location of the fault is well-constrained both on the Quickbird imagery and in the field by a clear single trace on both sides of the pond (Figure 17). Nonetheless, there is no detectable fault scarp within the part of the depression that is mantled by the pond deposits. Thus, it is probable that the latest fault rupture or scarplet has been sealed under the latest pond sediment aggradation. Given that the well-constrained fault morphology vanishes across the pond and the nature of the pond deposits, this location appeared to be a suitable place to conduct paleoseismic studies along this fault segment.

#### **4.2. Trench Stratigraphy**

The south Dig-e Rostam (SDR) trench was excavated across the fault, within the dry pond (Figures 16 and 17). The trench strikes N90°E, has a length of 59 m, a depth of up to 4.3 m, and a width of some 1.5 m. Once the trench was excavated, the walls were cleaned to remove trench smears and gouges created by the backhoe. A string grid, defining 1 m x 1 m panels, was strung along the length of the trench walls and each grid panel was then photographed by four slightly overlapping shots. The excavation exposes a succession of fine-grained, well-bedded layers interbedded with a few gravelly units. The fine-grained deposits are mostly horizontal and composed of laminated silts, clays, and sands. Based on the grain size and the location of trench excavation within the dry pond, these sediments are presumed to have been deposited in a playa-type environment. Most of the exposed layers are distinctive and laterally continuous (and so easy to correlate) along most of the length of the trench and remain undisturbed away from the fault zone. Several steep fault strands highlight a 10-m-wide fault zone cutting through the exposed deposits. The central part of this zone,

the main fault zone (MFZ), defines three distinctive sections (Figure 18a). The eastern section extends from the eastern tip of the trench up to meters 12-14, the MFZ extends between meters 12 and 17, and the western section is between meter 17 and the western tip of the trench near meter 58. At each section the stratigraphic units are numbered from oldest (smaller number) to youngest (larger number), but the unit designations do not imply correlation between sections. The stratigraphy of the three sections is summarized in the following paragraphs, and a detailed description of all the units is given in Table 5.

The eastern section is composed of a 4-m stack of sediment, mostly fine-grained pond deposits, and can be subdivided into five sets. The deepest (oldest) set contains fine-grained sediments including compact clay and silt strata (units 1e to 4e, Figure 18b). The strata between and next to the fault strands are tilted by 15 to 25 degrees eastward so that the oldest unit (unit 1e) is only exposed to the west. These fine-grained sediments are overlain by untilted, coarse-grained alluvial deposits (unit 5e). Unit 5e has an erosive base into unit 4e and represents the second set of sediments. An abrupt change in sedimentary facies along an erosion surface, between the coarse-grained alluvial deposits (unit 5e) and the fine-grained pond sediments (unit 6e), defines onset of a new set. This third set is mainly composed of compact clays and silts. The lower part of unit 6e, however, incorporates a few cobbles, possible remnants of a desert pavement developed on the underlying alluvial unit. Unit 6e was later disturbed by liquefied sandy sediments (unit 7e), which likely originated from unit 5e. A younger set, the fourth set, is 1.0- to 1.2-m thick and begins with a conspicuous erosion surface subsequently sealed by a thin (few centimeters) sandy-gravelly, possibly sheet flood, layer (unit 8e). This unit 8e is covered by well-bedded clays, silts, and sandy strata (units 9e to 12e) corresponding to pond sediments that remain horizontal except near to the main fault zone. The uppermost set of sediments begins by a facies contact between sandy strata (unit

12e) and compact clays (unit 13e). This fifth set consists of laminated silts and compact clays (units 13e to 16e) capped by the most recent pond deposits (unit 26).

The main fault zone, as shown on Figure 18a, is 3-4 m wide with prominent fault strands defining its western and eastern limits. The MFZ deposits can be subdivided into four sets, where all but one (unit 26) units are cut by several steep fault strands (Figure 18b). The lowest set is composed of fine-grained pond sediments (units 1f to 3f). Bedding, where discernable, is horizontal (between meters 14 and 15) or tilted up to 25° westward. The second set begins with an erosion surface overlain by a 20-cm-thick layer of coarse-grained deposits (unit 4f). Unit 4f contains poorly sorted ungraded gravels with sparse cobbles embedded in clay and silt. This unit 4f is incised and filled by fining-upward alluvial strata (units 5f and 6f). An abrupt change in sedimentary facies between the coarse-grained alluvial strata (unit 6f) and fine-grained sediments (unit 7f) represents the onset of a new set. The third set, unit 7f, incorporates a few cobbles in the lower part similar to the lower part of unit 6e in the eastern section. The uppermost (youngest) set in the MFZ begins with a finely-laminated lens of sandy gravels (unit 10f) that pinches eastward. This fourth set ends up with unit 26, here unconformably on thin-bedded silts and clays (units 11f to 13f), as these later units are gently inclined to the east. Several narrow strips of sheared, matrix-supported gravels (units 1s to 4s) are dislocated along the prominent fault strands and emplaced in the MFZ. They contain gravels that are oriented parallel to the fault planes and increasingly sheared nearest the faults.

The western section is a stack of some 4-m-thick, well-bedded, fine-grained, sediments intercalated by few fanglomerate layers in the lower and upper parts (Figures 18a and 18c). The exposed sediments in this section can be subdivided into six distinctive sets. The oldest set is exposed only close to the western tip of the trench and dominated by loose fine-grained sediments containing scarce ungraded gravels (unit 1w), which likely correspond to a mud

flow deposit. The second set (unit 2w) consists of alluvial deposits (distal fanglomerates) overlying an erosion surface. The first two sets of strata are gently ( $<5^\circ$ ) inclined eastward along the western half of the western section. The third set (units 3w, 4w, and 5w) is a fining upward sequence from coarse sands with some gravel lenses (transition alluvial fan-playa facies) to silt and clay layers (distal playa facies); this sequence corresponds to the development of a pond environment. Several liquefied sandy features, including sandy dikes and pillars (unit 6w), have injected into units 1w to 3w. A thin ( $<15$  cm) layer of coarse sands (unit 7w) is exposed close to the MFZ (between meters 17 and 20) unconformable on top of the compact clays of unit 4w (Figure 18b). This coarser facies forms the fourth set represented by fining-upward alluvial deposits (unit 8w) to the west. Both units 7w and 8w unconformably overlie the older deformed deposits (units 3w, 4w, and 6w). The fifth set dominated by well-bedded, fine-grained strata (units 9w to 12w), aggraded on an erosion surface overlapping the previous units. This fifth set disappears westward by meter 56, at the western end of the trench. The uppermost, sixth set begins with a thin, laminated sandy unit (unit 13w) that incorporates a very thin (few centimeters) layer of gravelly sands at the base with few sparse pebbles ( $<1$  cm) in the middle of the unit. This unit 13w fills mud-cracks distributed on top of unit 12w and is then overlain by a pile of  $\sim 2$ -m-thick, fine-grained sediments (units 14w to 20w). In the central part of the western section, between meters 35 and 44, unit 20w interfingers with ungraded gravelly alluvial deposits (unit 21w) coming from the west. The western part of the trench shows a transition between pond sediments (units 16w and 20w) and coarsening-upward gravelly deposits (units 21w to 25w) so that the maximum extent of the pond occurred during the aggradation of unit 15w. The gravelly units have been covered by the topmost deposits (units 26 and 25w). Unit 26 represents the most recent pond sediments made of laminated clays emplaced in the centre of the pond. Unit 26

interfingers westward with poorly-sorted gravelly debris-flow deposits (unit 25w) coming from the shutter ridge to the west.

### 4.3. OSL Dating and Ages of Stratigraphic Units

The stratigraphic chronology of the deposits exposed in the trench is determined using 18 OSL ages combined with lateral correlation of units along the length of the trench walls. All but one OSL ages are essentially consistent with the stratigraphic order of units (Figure 19). However, sample NT-XV from unit 8w yields an age ( $15.3 \pm 1.0$  ka) significantly older than the lower sample NT-XIV ( $6.4 \pm 0.5$  ka) from unit 3w (Figure 19). To solve this inconsistency, three further samples were collected from as near these two samples as possible and to sample NT-XII from unit 9w ( $6.7 \pm 0.5$  ka). The two samples located above (NT-XX) and below (NT-XXII) unit 8w yielded very similar ages of  $6.3 \pm 0.5$  ka and  $7.3 \pm 0.7$  ka, respectively, while sample NT-XXI from unit 8w yielded an age of  $8.3 \pm 0.6$  ka, again out of stratigraphic sequence although much less discrepant than before. This unit consists of gravelly coarse sands with a significant content of clay, and appears to be mostly reworked material within a distal mudflow. The two unusually old ages (NT-XV and NT-XXI) from unit 8w, when considered together with these field observations suggest that unit 8w sediments were probably incompletely bleached at deposition. As a result, they are dismissed from further discussion.

The available OSL ages indicate that the oldest sediments in the trench are seen within the MFZ. The lower, hence older, units (units 1f to 3f) are older than  $70 \pm 5$  ka (sample NT-IX) while the upper units (units 11f to 26) are younger than  $5.6 \pm 0.4$  ka (sample NT-V). The elapsed time of  $64 \pm 5$  ka between these samples and the sediment thickness between them (<2 m) indicates that the MFZ exposes a discontinuous record of sediments between the end of MIS-5 (~75 ka, [e.g., *Grootes and Stuiver, 1997; Cutler et al., 2003*]) and the late

Holocene. The depositional environment of the oldest trench units (units 1f to 3f) is similar to that of the youngest deposits (units 11f to 26 in the MFZ, units 20w and 26 in the western section, and units 13e to 26 in the eastern section); all appear to be pond sediments (Table 5). The oldest OSL age,  $70 \pm 5$  ka (sample NT-IX) indicates the trench site has been mostly a pond for a long time. Moreover, the pond outlet exhibits a  $\sim 250$  m northward deflection (see section 4.1 and Figure 16c) that results from cumulative right-lateral motion along the Nayband fault. Given the estimated slip rate of  $1.8 \pm 0.7$  mm yr<sup>-1</sup> (see section 3.4), the now dry pond should have been formed against the shutter-ridge at least some  $160 \pm 60$  ka ago.

Two stratigraphic columns with the OSL age constraints, on each side of the MFZ, are given in Figure 19. These OSL ages indicate that the emplacement of nearly all the sediments exposed both to the west and to the east of the MFZ are consistent with MIS-1 and MIS-2 (11-24 ka [e.g., Phillips et al., 2000]). Indeed, to the west of the MFZ, the  $\sim 4$ -m-thick stack of sediments was deposited at least within the last 20 ka (sample NT-XIX) while to the east of the MFZ, the upper 2.4 m of the sediment pile were deposited during the last 17 ka (sample NT-VI). These yield average sedimentation rates of 0.14 and 0.20 mm yr<sup>-1</sup>, respectively east and west of the MFZ (Figure 20).

The deposits in the western section (units 3w to 26) reach a maximum thickness of 4.2 m (near meter 19) and were aggraded within the last  $6.7 \pm 0.4$  ka (weighted average age of samples NT-XIV and NT-XII). A sample collected some 60 cm below (NT-XIX,  $19.7 \pm 1.6$  ka) suggests the stratigraphic record for the intervening 13 ka is missing, or the age of NT-XIX is significantly older than the deposit. Although shorter, a similar missing stratigraphic section is found to the east of the MFZ, where ages of  $10.3 \pm 0.8$  ka (sample NT-XVIII) and  $17.4 \pm 1.3$  ka (sample NT-VI) suggest  $\sim 7$  ka of sediments are missing. In the MFZ, unit 7f is a lateral equivalent of unit 6e (Figure 18b and Table 5); the upper part of unit 6e yields  $17.4 \pm 1.3$  ka and a comparison with the age of  $5.6 \pm 0.4$  ka (sample NT-V within the MFZ) also

indicates a lack of stratigraphic record of  $\sim 12$  ka. Thus, sediment appears to be missing along the whole length of the trench from about 10 ka to 17 ka. This long gap is based on the two older OSL ages of  $17.4 \pm 1.3$  ka and  $19.7 \pm 1.6$  ka (samples NT-VI and NT-XIX) in the eastern and western sections, respectively. If these two samples were partially bleached (as were samples from unit 8w) this could lead to an erroneously long gap in the sediment deposits. However, neither of these sedimentary units contains any evidence for reworking (in contrast to unit 8w) and we so reject this hypothesis, and conclude that there is no sediment record for approximately the upper half of MIS-2 and the early Holocene. This absence may result either from a prominent gap of sedimentation events or from removal of the sediments by subsequent erosion. The second option is less likely, assuming the nearly continuous aggradation during the sediment gap needs at least two erosion phases (Figure 20): one before the deposition of unit 8e and another one after unit 12e. In fact, the difference in gap duration between the eastern and western sections is mainly explained by the fact that aggradation resumes earlier to the east of the fault (before  $10.3 \pm 0.8$  ka) than to the west of it (before  $6.7 \pm 0.4$  ka). Therefore, a prominent gap of sedimentation appears simpler and hence more likely; it suggests that climatic conditions favored sediment transport and erosion rather than aggradation at the end of MIS-2 and beginning of MIS-1.

Comparing the thicknesses of the units younger than  $\sim 7$  ka on both sides of the MFZ indicates a much thicker pile of deposits in the western section than in the eastern one. Indeed, the samples NT-XII and NT-XX (weighted average of  $6.5 \pm 0.4$  ka) collected from the base of unit 9w and the sample NT-III ( $6.1 \pm 0.4$  ka) collected above unit 13e indicate that units 9w and 13e are indistinguishable in age. In addition, the two OSL samples that were collected from the upper parts of unit 16e (sample NT-I,  $0.98 \pm 0.08$  ka and sample NT-II,  $0.74 \pm 0.06$  ka) are in the same age range that the one obtained from the upper part of unit 20w (sample NT-VII,  $0.79 \pm 0.06$  ka). These well-constrained and similar ages acquired from

these three samples indicate that the deposition of unit 16e to the east of the MFZ occurred at about the same time as the deposition of the upper part of unit 20w to the west of the MFZ. Up to 0.9 m of sediment (units 13e to 16e) was deposited east of the MFZ essentially at the same time as 3.3 m (units 9w to 20w) was deposited on the west side (Figure 18). This difference probably results from the initial position of the western section closer to the center of the pond. In addition, renewing of eastward tilting would have occurred between units 8w and 9w to produce downwarping to the west of the Main Fault Zone, hence increasing the accommodation space and allowing more aggradation in this section.

In any event, the continuity of upward aggradation from unit 9w provides an upper bound for the last regional incision (6.1 ka, minimum possibility of the weighted average age of samples NT-XII and NT-XX). Combining with the lower bound of that incision provided by the oldest possible age of the youngest sediments aggraded at site North (7.4 ka, sample NA-3), indicates the age of the most recent regional incision is accurately bracketed between 6.1 ka and 7.4 ka.

#### **4.4. Seismic Event Identification**

The recognition of seismic events in the SDR trench is based on direct (structural observations) as well as secondary (earthquake-induced sedimentary features) evidence of ground rupture and shaking. There is evidence for at least four surface faulting events within the last  $17.4 \pm 1.3$  ka and two older earthquakes, one before  $\sim 23$  ka and another before  $70 \pm 5$  ka. The identification of these six seismic events, designated as A, B, C, D, E and F from the youngest to the oldest (Figure 18) is reported below.

The recognition of the most recent earthquake, **event (A)**, is based on three independent lines of evidence. First, the abrupt upward terminations of several fault strands, capped by the most recent pond deposit (unit 26, Figures 18a and 18b), provide the primary line of

evidence. One such clear fault termination is exposed near meter 20, where the well-bedded deposits resting below unit 26 are vertically offset by 20-25 cm. Two other fault strands, one near meter 12 and another one near meter 15, resulted in the offset of several layers by 10-15 cm (units 13e to 16e in the eastern section corresponding to units 11f to 13f in the MFZ section) lying below the undisturbed unit 26 (Figure 21). Second, locally tilted units 10f to 13f (between meters 12 and 16) are unconformably covered by flat-lying unit 26. Additionally, the drag folding of unit 20w against a prominent steep fault strand near meter 16.5 is also unconformably overlain by unit 26, testifying for event A (Figure 22). Third, the occurrence of several sandy dikes (units 23w and 24w) disrupting the upper strata are sealed by unit 25w (Figures 18c and 23), testifying for the same event in the western section of the trench. These dikes have apparent widths ranging from a few up to 40 cm and consist of loose, unsorted, sands injected from the underlying strata containing scarce pebbles from the host layers.

Although the upward termination of a fault strand is sometimes difficult to relate with a given seismic event of a series of paleoearthquakes [Bonilla and Lienkaemper, 1990], the fact that displacements of several centimeters occur just below the abrupt truncation of the fault by the sealing horizon provides confidence for the interpretation of event A. Similarly, the narrow fault zone near meter 20, with vertical displacements almost constant through the four-meter-thick pile of units 3w to 20w, sealed by unit 26, indicates that the base of unit 26 must correspond to an event horizon. Furthermore, the dragged layers and sandy dikes are sealed by the same stratigraphic horizon (units 26 and 25w) as the fault terminations. Therefore, event A has occurred after the deposition of units 16e, 13f, 20w, 22w and prior to the deposition of the most recent sediments (units 26 and 25w). Consequently the lower limit of units 26 and 25w represents the event horizon of the most recent earthquake. The layers from which samples NT-I ( $0.98 \pm 0.08$  ka), NT-II ( $0.74 \pm 0.06$  ka) and NT-VII ( $0.79 \pm 0.06$

ka) were collected define the lower bound of the event-A horizon (EH-A in Figures 18b and 18c). The reliability of these ages is supported by that of the closest to the surface sample, sample NT-XXIII, collected 7 cm below the ground surface. This gives an age of  $0.07 \pm 0.03$  ka, confirming that these sediments are likely to have been well-bleached at deposition. Thus, the minimum and maximum time intervals for event A are respectively 0.68 ka - 0.1 ka and 0.8 ka - 0.04 ka (youngest/oldest possible age of sample NT-II versus oldest/youngest possible age of sample NT-XXIII). Therefore, the most recent earthquake (event A) occurred more recently than eight hundred years ago.

The penultimate and antepenultimate earthquakes, **event B** and **event C**, are less easy to identify because they occurred in a narrow stratigraphic window. Their respective event horizons are only separated in the western section of the trench where preserved evidence allows us to distinguish unambiguously two unconformable erosion boundaries that should correspond to two earthquakes and to date them very precisely.

To the west of the MFZ, the most conclusive evidence for **event B** is subtle. Its event horizon, EH-B, corresponds mainly to an erosion surface prior to the deposition of unit 9w, which overlies unit 8w and its eastward lateral equivalent unit 7w as well as older units (4w, 3w, and 1w). All these older units dip eastward while unit 9w is horizontal, and so stands unconformably and onlapping westward onto underlying units. Locally, event B also produced small vertical faults affecting units 3w to 7w (meters 16.5 to 20) that are sealed by unit 9w (Figures 18b and 24).

Unambiguous evidence for **event C** is seen in the western section of the trench. From meter 42 westward, several liquefaction features (unit 6w) disrupt units 1w to 3w and are covered by undisturbed alluvial deposits of unit 8w (Figures 18c and 25). The liquefied features range in width from a few centimeters to as much as 180 cm, and in height up to

more than 110 cm, they consist of sand-filled feeder dikes and pillars. These liquefied features are sealed by unit 8w indicating an event horizon below this unit. Unit 7w a lateral equivalent of unit 8w seals small faults (near meter 17.5) disrupting the underlying units (Figure 24). Consequently, the lower limit of units 7w and 8w also delineates the event horizon, EH-C, of the third paleoearthquake. EH-C corresponds to an unconformable erosion boundary between unit 8w and underlying east-dipping units 4w, 3w, 2w, and 1w (Figure 18c).

To constrain accurately the respective ages of events B and C, a total of six OSL samples were taken from units 3w (NT-XIV and NT-XXII), 8w (NT-XV and NT-XXI), and 9w (NT-XII and NT-XX) so that each unit sampling was duplicated (see section 4.3). Unit 8w yielded quite different ages and these are discarded for the reasons discussed above. Unit 3w yielded overlapping ages of  $6.4 \pm 0.5$  ka and  $7.3 \pm 0.7$  ka from which a weighted average age of  $6.7 \pm 0.4$  ka was calculated. Unit 9w also yielded very similar ages of  $6.7 \pm 0.5$  and  $6.3 \pm 0.5$  ka, which give a weighted average of  $6.5 \pm 0.4$  ka. Thus, the ages of units 3w and 9w are indistinguishable. As the ~25-cm thick unit 8w stands between these two units, the weighted average age of the two bounding units,  $6.6 \pm 0.3$  ka, provides the age of unit 8w. Therefore, events B and C occurred between  $6.7 \pm 0.4$  and  $6.5 \pm 0.4$  ka, suggesting that in a short period of at most ~1 ka the following events occurred: the end of the aggradation of unit 3w, event C and subsequent erosion, the deposition of unit 8w, event B and subsequent erosion, and finally the onset of accumulation of unit 9w. The occurrence of two seismic events within a short time interval may indicate that the seismic behavior of the Nayband fault can be characterized by clustering of earthquakes. Alternatively, event B might be a large aftershock of event C.

In the eastern section of the trench and the MFZ, events B and C cannot be distinguished from each other. The contact between units 12e and 13e defines the mixed event horizon

(EH-B+C) of the penultimate and antepenultimate events. There, two fault strands, one near meter 9 and another near meter 11, terminate upward at the same stratigraphic horizon, at the base of unit 13e (Figures 18b and 26). The capped faults cut through units 1e to 12e, offsetting the entire sequence by more than 15 cm, at the base of unit 12e. The fine-grained sediments of unit 13e overlie these fault strands. Using OSL samples collected below (NT-IV) and above (NT-III) the EH-B+C, the age of this horizon is bracketed between  $8.4 \pm 0.6$  ka and  $6.1 \pm 0.4$  ka. Interestingly, the short time span for the occurrence of events B and C, which is determined in the western section, fits within the time interval determined for the sealing of these faults. Units 9e to 12e have been preserved only to the east of the MFZ and they abruptly disappear against the eastern prominent fault strand of the MFZ (around meter 12). Therefore, the western extension of that thick (up to 1 m), fine-grained, and flat-lying sequence should have been initially tapering off onto the MFZ and subsequently eroded after earthquakes B and C and before the deposition of unit 10f, i.e., prior to  $5.6 \pm 0.4$  ka (NT-V, Figures 19 and 20, see section 4.3).

The recognition of a fourth paleoearthquake, **Event D**, is based on several abrupt upward fault terminations and earthquake-induced sedimentary features that are only seen in the eastern part of the trench. Several distinct upward terminations of fault splays, of which the ones observed close to meters 9 and 10 are the most demonstrative, provide evidence for event D (Figures 18b and 27). To the east of the MFZ (Figure 27), two west-dipping faults cut up through units 1e to 6e and abruptly terminate at the base of unit 8e. Units 1e-6e are associated with vertical displacements along the eastern fault strand that range from 120 cm (at the base of unit 6e) to 140 cm (at the base of unit 2e). Unit 6e is much thicker to the east than to the west of the eastern fault (near meter 9), where its upper part has been removed by erosion after event D. Additional evidence for event D comes from the recognition of liquefaction features emplaced within units 6e and 7f. These features, to the east of the MFZ,

consist of rather loose sands that originate from the lower sandy-gravelly strata, mainly from unit 5e, and are sealed by unit 8e. The liquefied features are sealed by the same stratigraphic horizon as the abrupt fault terminations; this makes the possibility of a site effect caused by a remote earthquake unlikely. Therefore, the event horizon of the fourth paleoearthquake (EH-D) has to be set at the base of unit 8e (Figure 27). This event D occurred after the deposition of unit 6e; hence it postdates  $17.4 \pm 1.3$  ka (sample NT-VI, collected from the top of unit 6e). Since the units immediately above EH-D consist of a very thin sandy-pebbly layer (unit 8e) topped by compact clays (unit 9e), unsuitable for OSL dating, sample NT-XVIII ( $10.3 \pm 0.8$  ka) was collected from sandy layers at the base of unit 10e. Thus, the fourth event on this vertical section occurred between  $10.3 \pm 0.8$  and  $17.4 \pm 1.3$  ka.

Liquefaction features in the MFZ (unit 9f) are unconformably covered by a sandy lens (unit 10f) that yielded an OSL age of  $5.6 \pm 0.4$  ka (sample NT-V). The long time span between units 10f and 7f (corresponding to the lower part of unit 6e) overlaps the occurrence of events B, C, and D and hence does not permit to determine what are the respective contributions of these three earthquakes within the MFZ.

The recognition of a fifth paleoearthquake, **event E**, is based on several abrupt upward terminations of fault strands located within the MFZ and a fissure fill localized at the base of unit 6e to the east of the MFZ (Figure 18). In the MFZ, near meter 15, a nearly vertical fault strand cut through sediments up as far as unit 6f, for which the lower limit is downthrown westward by  $\sim 50$  cm (Figure 18b). Upwards, this fault is sealed both by unit 7f and the liquefied feature (unit 9f) produced by event D, indicating a fault displacement occurred between deposition of units 6f and 7f. Similarly, two superposed, low-dipping fault strands, close to meter 13, offset the entire sequence up to unit 6f. The upper one is sealed by unit 7f while the lower one, which shows a vertical throw of  $\sim 1$  m at the base of unit 6f, is characterized by a steeper upward prolongation that displaces the base of unit 7f by less than

10 cm. This difference indicates that there should be a faulting event between units 6f and 7f. Additionally, to the east of the MFZ near meter 10, the western strand of a west-dipping faulted wedge shows different vertical displacements between units 6e and lower units (Figure 18b). Indeed, the lower units are displaced by ~140 cm (measured at the base of unit 4e) while the base of unit 6e is displaced by only 35 cm. As the displacement of the base of unit 6e must have occurred during event D, the remaining vertical displacement of ~1 m is presumably associated with an older faulting event. This later displacement, and all the upward fault terminations discussed above, occurred before the deposition of unit 6e or its lateral equivalent, unit 7f. Thus, the lower limit of these two units must correspond to an event horizon (EH-E on Figure 18b).

Additional evidence for event E comes from the fact that the oldest units exposed in the eastern section (units 1e to 5e) have been tilted eastward by ~15° between meters 10 and 14 whereas these older units are unconformably covered by the horizontal unit 6e (Figure 18b). Moreover, a fissure, with a depth of 40 cm, between meters 4 and 5 (Figure 18a) has affected unit 5e and was subsequently filled with the fine-grained sediments of unit 6e, consistent with a fifth paleoearthquake before deposition of unit 6e. The age of this event E is poorly constrained as there is no direct age control below the EH-E. However, one can combine the estimated average sedimentation rate of the eastern section (0.14 mm yr<sup>-1</sup>, Figure 20) with the sediment thickness between sample NT-VI and EH-E to suggest that event E should have occurred sometime before ~23 ka.

There is also evidence for an older paleoearthquake, **event F**, in the MFZ. Several sub-vertical fault strands, between meters 13.5 and 15.5, offset units 1f to 3f by ~40 cm and are sealed by unit 4f. This implies the occurrence of a paleoearthquake (event F) prior to the deposition of unit 4f (Figure 18b), hence before  $70 \pm 5$  ka (sample NT-IX).

Therefore, discarding the old F event, a maximum of 5 earthquakes can be identified during approximately the last 23 ka (Figure 28). A rough approach might suggest an average time interval between subsequent earthquakes of some 6 ka. However, this first-order reasoning could be biased as sedimentation has not been continuous during the last 17-20 ka.

## **5. Discussion and conclusions**

### **5.1. Seismic Behavior of the Nayband Fault**

The smallest right-lateral offsets preserved less than 1 km to the north of the trench site are on the order of 3-4 m (Figure 15a). Considering these smallest right-lateral displacements occurred during the most recent earthquake, the magnitude of event A should be on the order of  $M_w \sim 7$ . The nearby right-lateral offsets ranging between 6 and 16 meters (Figures 15b-15d) must incorporate the displacements of former events, including the events B, C, and possible older events. Offsets of 6 m, which is twice the smallest measured value, should sum the displacements of the two last events (A and B?) while the 10 m offsets might incorporate the displacements of the three last events. If so, a  $\sim 3$  m displacement per event suggests that the corresponding magnitudes were on the order of  $M_w \sim 7$  [e.g., Wells and Coppersmith, 1994].

Although the amount of lateral displacement during an event is not accessible in a single trench, there are some additional indicators that one can use to estimate the magnitudes of the identified earthquakes. The event horizon of the penultimate and antepenultimate earthquakes (EH-B+C), near meter 12 is downthrown to the west by 20 cm during the most recent earthquake (event A, Figure 18b). Restoration of this vertical throw suggests a vertical displacement on the event horizon of the fourth paleoearthquake (EH-D) of more than a meter during events B+C. Taking into consideration that the Nayband fault is a primary strike-slip fault, one meter of vertical displacement should be associated with several meters

of right-lateral displacement. Thus, the magnitude of the penultimate and antepenultimate earthquakes (events B and C) should be also on the order of  $M_w \sim 7$ , in agreement with a 3 m average displacement as postulated above.

The vertical displacement associated with event D is even larger than the ones for events B and C. Indeed, on the fault strand close to meter 9, the vertical throw of event D is on the order of 120 cm (Figures 18b and 27). This vertical displacement would also be compatible with several meters of right-lateral slip during event D and a magnitude of  $M_w \sim 7$  or greater. Such a magnitude would be in agreement with the prominent sand-filled feeder dikes and pillars observed along the eastern trench exposures and sealed by event horizon D. If one removes the estimated vertical throws during events A, B, C, and D, a vertical displacement of approximately 200 cm occurred during event E, distributed on several fault strands between meters 10 and 15 (see section 4.4). These observations suggest a magnitude  $M_w \sim 7$  or greater for the fifth paleoearthquake.

The rough estimates of the magnitude of events A, B, C, D, and E all suggest that the 65-km-long NA2 strike-slip fault segment can produce  $M_w \sim 7$  earthquakes, in agreement with the empirical relationships linking surface rupture lengths and moment magnitudes for strike-slip faults as well as with the assessed 3 m displacement per event [Wells and Coppersmith, 1994].

The long-term slip rate averaged over the last 100 ka of  $1.8 \pm 0.7$  mm yr<sup>-1</sup> for the NA2 segment (Figure 11) and a 3 m displacement per event yield a time duration between 1200 and 2800 years to cumulate such a potential displacement. This does not match the mean time interval of  $\sim 6$  ka calculated over the last  $\sim 23$  ka (see section 4.4) between two subsequent seismic events. Considering the four earthquakes that have occurred within the last  $17.4 \pm 1.3$  ka (OSL sample NT-VI) and the age of the fourth one, event D bracketed between 18.7 ka

(maximum age of sample NT-VI) and 9.5 ka (minimum age for sample NT-XVIII), a recurrence interval of 3-6 ka for surface rupturing earthquakes can also be estimated. As there is a lack of sediment between  $10.3 \pm 0.8$  ka (NT-XVIII) and  $17.4 \pm 1.3$  ka, the paleoseismic record may be incomplete; then, the lower bound of the former range might be closer to the actual recurrence interval. A 3 ka recurrence interval would nearly match with the 2800 years roughly estimated by dividing a 3 m slip per event by the slip rate.

Focusing on the last 6-7 ka may provide a better estimate of the recurrence interval as this time range is characterized by nearly continuous sedimentation in the western section of the trench. It should be nonetheless noted that, between event B and event A, there is a set of small fissures observed below the base of units 12w and 14w, where 12w is lacking. These fissures, which are filled by an aeolian sandy deposit, could be interpreted either as desiccation cracks or tentatively as features induced by an additional earthquake. This set of fissures occurred before  $4.1 \pm 0.3$  ka (sample NT-XI in unit 12w). These small fissures are evenly distributed and at least some can be unambiguously attributed to desiccation cracks that should result from the late Holocene drought cycles following 4.2 ka evidenced farther east [Staubwasser *et al.*, 2003]. It is thus very unlikely that an earthquake postdating event B and predating event A has taken place before  $4.1 \pm 0.3$  ka. We conclude that three major events only, A, B, and C, are identified within the time interval of 5.3-7 ka (respectively minimum and maximum time intervals between events A and C). Although three earthquakes (A, B, and C) are identified during the last 6-7 ka, events B and C occurred within a maximum time span of 1 ka so that event B may be interpreted either as a large aftershock of event C or as an actual event indicating the Nayband fault does not exhibit time-dependent earthquake behavior. The first option would imply that two main earthquakes only have occurred during the last 6-7 ka, the recurrence interval for large earthquakes being then close to the one calculated for the last  $\sim 23$  ka. In that case, a significant percentage of the strain

should have to be released by creep. The second option would indicate large earthquakes occur randomly (i.e., Poisson behavior with at most 1 ka, probably less, between events B and C versus  $6.2 \pm 0.9$  ka between events A and B). Such a random behavior could be characterized by clustering events, hence making useless estimating an average recurrence time interval. In the absence of microseismic activity delineating the Nayband fault trace, we favor clustering but further studies will have to settle which of creep or clustering options stands for the Nayband fault.

## **5.2. The Most Recent Earthquake on the Nayband Fault Versus the Historical Records**

The most recent of the paleoearthquakes found on the Nayband fault occurred during the last 800 years (i.e., after AD 1200) in a remote and uninhabited desert land. Although this event occurred during the time span covered by the historical seismic records [*Ambraseys and Melville*, 1982; *Ambraseys and Jackson*, 1998; *Berberian and Yeats*, 1999], none of the available catalogs provides evidence for an historical earthquake on the Nayband fault.

Either the earthquake has been unnoticed or it was reported with an inaccurately located epicenter, perhaps because of the anarchy prevailing during and after the Mongol invasions (from AD 1220 by the end of the Saljuq Empire until the fall of Baghdad in AD 1258 [e.g., *Boyle*, 1968]). The historical catalogs indicate that several large earthquakes occurred after AD 1200, to the north and northeast of the Nayband fault. To the north, five earthquakes occurred in AD 1209, AD 1251, AD 1270, AD 1389 and AD 1405, all located close to the city of Neyshabur, 400 km to the north of the Nayband fault. To the northeast, two earthquakes occurred in AD 1336 and AD 1549, in the cities of Khaf and Qa' en, 300 and 180 km to the northeast of the Nayband fault, respectively. All these events can be associated with active faults (Neyshabur fault system, Doruneh fault or Jangal thrust, and Sistan fault system) in the vicinity of their epicentral regions. The AD 1549 (Qa'en) earthquake , that

closest to the Nayband fault, is related either to the Abiz fault [Berberian and Yeats, 1999] or to the North Birjand fault [Berberian and Yeats, 2001]. Thus, it is very unlikely that one of the known historical earthquakes in Central Iran can be associated to the Nayband fault; rather it is more likely that the earthquake that took place on the fault within the last 800 years went unreported. This conclusion, combined with the fact that there are other strike-slip faults known to have produced destructive earthquakes with recurrence interval of several thousands of years in Central Iran [Nazari et al., 2009; Fattahi et al., 2010; Foroutan et al., 2012] challenges the reliability of assessing the regional seismic hazard using historical seismic catalogs alone.

### **5.3. Implications for Seismic Hazard and Kinematics in Central and Eastern Iran**

This paleoseismic investigation along the Nayband fault demonstrates the occurrence of several large, infrequent, and irregular earthquakes during MIS-1, and possibly part of MIS-2. Indeed, the fault hosted at least four large ( $M_w \sim 7$ ) earthquakes within the last  $17.4 \pm 1.3$  ka and two older earthquakes one probably before some 23 ka and another before  $70 \pm 5$  ka. The occurrences of three large earthquakes during the last  $\sim 7$  ka suggest that the Nayband fault could be characterized by a clustering of events; two events occurred close to  $6.6 \pm 0.3$  ka, separated by a maximum time interval of 1 ka, and the youngest earthquake (after AD 1200) is separated from the penultimate by  $\sim 6$  ka. Although the most recent earthquake occurred less than 800 years ago, the long seismic cycle of some 6 ka preceding this most recent event should not be interpreted as evidence that the hazard is low. Seismic clustering is recorded over the last decades on the more southerly fault section. Overlapping segments of the Gowk fault hosted two destructive earthquakes within seventeen years by the end of the 20th century (the 1998 March 14,  $M_w$  6.6, Fandoqa earthquake [Berberian et al., 2001; Fielding et al., 2004] and the 1981 July 28,  $M_s$  7.1, Sirch earthquake [Berberian et al., 1984]).

The data for the Nayband fault complement the paleoseismic information already available for the Central Iran Plateau (Figure 29). For the Dehshir fault [Nazari *et al.*, 2009], the most recent earthquake (EH-A) occurred shortly before  $2.0 \pm 0.2$  ka [Fattahi *et al.*, 2010]; the available historical seismic catalogs provide no evidence for an historical earthquake in the vicinity of the Dehshir fault. The revised OSL ages (green numbers on Figure 29b) indicate the Dehshir fault hosted at least three earthquakes within the last  $20.2 \pm 0.8$  ka. Considering the age of the most recent event ( $2.0 \pm 0.2$  ka) yields an average recurrence interval of large earthquakes at most between 5700 and 6400 years. Similarly, the paleoseismic records of the Anar fault document the occurrence of at least three large earthquakes (EH-A, EH-B and EH-C on Figure 29b) within the last 15 ka [Foroutan *et al.*, 2012]. There, the most recent earthquake occurred sometime between 3.6 and 5.2 ka ago, and the average recurrence interval of the large earthquakes ranges between 2.4 and 5 ka. It seems that large and infrequent earthquakes appear to typify the seismic behavior of the slow-slipping, intracontinental, strike-slip fault systems slicing Central and Eastern Iran. The limited data available, however, fail to document any distance interactions between the seismic behavior of the neighboring fault systems. Both the fact that the recurrence intervals on these faults exceed the time span covered by historical catalogs and the fact that some of these faults have produced large unrecorded earthquakes during the time span covered by these catalogs suggests caution in the regional seismic hazard assessment.

The observed geomorphic offset markers and their corresponding  $^{36}\text{Cl}$  and OSL ages provide the long-term slip rate of the Nayband fault averaged over the last 100 ka. This short-term geologic estimated slip rate of  $1.8 \pm 0.7$  mm yr<sup>-1</sup> is consistent with the long-term geologic slip rates previously reported ( $1.5$  mm yr<sup>-1</sup> [Walker and Jackson, 2002] and  $1.4 \pm 0.5$  mm yr<sup>-1</sup> [Walker *et al.*, 2009]). These results suggest that the slip rate remained constant through the entire Quaternary.

This rate matches with an overall late Pleistocene and Holocene right-slip rate along the western margin of the Lut block and along the transfer zone between Zagros and Makran decreasing from south to north (Figure 29a). This northward decrease (Minab-Zendan fault system,  $4.7 \pm 2.0 \text{ mm yr}^{-1}$  or  $6.3 \pm 2.3 \text{ mm yr}^{-1}$ , depending on the age attributed to the offset markers on the Zendan fault [Regard *et al.*, 2010]; Sabzevaran-Jiroft fault system,  $5.7 \pm 1.7 \text{ mm yr}^{-1}$  [Regard *et al.*, 2005]); Gowk,  $\geq 3.8 \pm 0.7 \text{ mm yr}^{-1}$  [Walker *et al.*, 2010b] further refined to  $3.8\text{-}5.7 \text{ mm yr}^{-1}$  [Fattahi *et al.*, 2014]; and Nayband,  $1.8 \pm 0.7 \text{ mm yr}^{-1}$  faults) appears consistent with the general pattern of the GPS horizontal velocities related to stable Eurasia (Figure 1b) [Vernant *et al.*, 2004]. While the long-term slip rate across the Lut block appeared difficult to reconcile with the hitherto limited available GPS data, recent results from a dense network across Eastern Iran [Walpersdorf *et al.*, 2014] appear in good agreement with our knowledge of the geological rates (Figure 29). The new set of GPS data demonstrates significant internal deformation west of the Lut block, in Central Iran and a dextral shear equally partitioned on the both eastern and western Lut borders. The modeling of these recent GPS data [Walpersdorf *et al.*, 2014] yields slip rates in agreement with most of the well-constrained geological rates (e.g., Dehshir, Anar, and Gowk faults) and many of the roughly estimated ones (e.g., East Lut fault system). However, the well-constrained Late Pleistocene-Holocene geological rate of the Nayband fault ( $1.8 \pm 0.7 \text{ mm yr}^{-1}$ , this study) is discrepant with the GPS-rate ( $4.4 \pm 0.4 \text{ mm yr}^{-1}$ ) derived from this new GPS deformation field. A comprehensive geomorphological study of the East Lut fault system is therefore needed to establish well-constrained geological slip rates and further test the consistency between geologic and geodetic rates.



## Acknowledgments

This study, conducted in the frame of Mohammad Foroutan PhD thesis, benefited of the logistic and financial assistance of the Geological Survey of Iran. Université Pierre et Marie Curie provided complementary funding for the fieldwork and the  $^{36}\text{Cl}$  measurements. The  $^{36}\text{Cl}$  measurements were performed at the ASTER AMS national facility supported by the INSU/CNRS, the French Ministry of Research and Higher Education, IRD, and CEA. OSL dating has been performed at the Nordic Laboratory for Luminescence Dating of Aarhus University and funded by GSI and an INSU-CNRS specific grant. MF acknowledges a grant from the French Embassy in Tehran for part of his PhD thesis and complementary support from UPMC-ISTeP. Pierre-André Lhôte, Attaché Scientifique et Culturel, is thanked for his support to the cooperation between UPMC and GSI. We thank R. Sohbaty and the technical staff at the Nordic Laboratory for Luminescence Dating for helping with OSL-measurements and acknowledge E. R. Engdahl for giving us access to his updated EHB catalog. A. Rashidi and M. Nazem Zadeh from Kerman GSI office helped with the logistics of the fieldwork. We thank M. Adhami, H. Bani Assadi, and H. Mokhtari for their safe driving in the field. We are grateful to Andrea Walpersdorf for sending us the accepted version of a publication providing new GPS results. We acknowledge helpful and detailed reviews by Richard Walker and an anonymous reviewer. We thank the Editor, Tom Parsons, for helping us to clarify two specific points of the revised version.

## References

- Agard, P., Omrani, J., Jolivet, L., Whitechurch, H., Vrielynck, B., Spakman, W., Monié, P., Meyer, B., and R. Wortel (2011), Zagros orogeny: a subduction-dominated process, *Geol. Mag.*, *148*(5-6), 692-725, doi:10.1017/S001675681100046X.
- Aghanabati, A. (1974), Geological map of Tabas, Quadrangle *I7*, scale 1:250,000, Geol. Surv. of Iran, Tehran.
- Aghanabati, A. (1993), Geological map of Bam, Quadrangle *J11*, scale 1:250,000, Geol. Surv. of Iran, Tehran.
- Aitken, M. J. (1985), *Thermoluminescence Dating*, 359 pp., Academic Press, London.
- Aitken, M. J. (1998), *An Introduction to Optical Dating*, 267 pp., Oxford Univ. Press, Oxford.
- Alavi-Naini, M., and Griffis, R. (1981a), Geological map of Naybandan, Quadrangle *J8*, scale 1:250,000, Geol. Surv. of Iran, Tehran.
- Alavi-Naini, M., and Griffis, R. (1981b), Geological map of Lakar Kuh, Quadrangle *J9*, scale 1:250,000, Geol. Surv. of Iran, Tehran.
- Allen, M., Jackson, J., and R. Walker (2004), Late Cenozoic reorganization of the Arabia-Eurasia collision and the comparison of short-term and long-term deformation rates, *Tectonics*, *23*, TC2008, doi:10.1029/2003TC001530.
- Allen, M. B., Kheirkhah, M., Emami, M. H., and S. J. Jones (2011), Right-lateral shear across Iran and kinematic change in the Arabia-Eurasia collision zone, *Geophys. J. Int.*, *184*, 555-574, doi:10.1111/j.1365-246X.2010.04874.x.

Ambraseys, N. N., and J. A. Jackson (1998), Faulting associated with historical and recent earthquakes in the Eastern Mediterranean region, *Geophys. J. Int.*, *133*, 390-406.

Ambraseys, N., and C. Melville (1982), *A History of Persian Earthquakes*, 219 pp., Cambridge Univ. Press, Cambridge.

Baker, C. (1993), Active seismicity and tectonics of Iran, *PhD thesis*, University of Cambridge, Cambridge.

Barnhart, W. D., Hayes, G. P., Samsonov, S. V., Fielding, E. J., and L. E. Seidman (2014), Breaking the oceanic lithosphere of a subducting slab: The 2013 Khash, Iran earthquake, *Geophys. Res. Lett.*, *41*, 1-5, doi:10.1002/2013GL058096.

Berberian, M. (1979a), Tabas-e-Golshan (Iran) catastrophic earthquake of 16 September 1978; a preliminary field report, *Disasters*, *2*, 207-219.

Berberian, M. (1979b), Earthquake faulting and bedding thrust associated with the Tabas-e-Golshan (Iran) earthquake of September 16, 1978, *Bull. Seismol. Soc. Am.*, *69*, 1861-1887.

Berberian, M. (1981), Active faulting and tectonics of Iran, in *Zagros, Hindu Kush, Himalaya Geodynamic Evolution*, edited by Gupta, H. K. and F. M. Delnay, *Geodyn. Ser.*, *3*, 33-69.

Berberian, M., and G. C. P. King (1981), Towards a paleogeography and tectonic evolution of Iran, *Can. J. Earth Sci.*, *18*, 210-265.

Berberian, M., and M. Qorashi (1994), Coseismic fault-related folding during the South Golbaf earthquake of November 20, 1989, in southeast Iran, *Geology*, *22*, 531-534.

Berberian, M., and R. S. Yeats (1999), Patterns of historical earthquake rupture in the Iranian plateau, *Bull. Seismol. Soc. Am.*, *89*(1), 120-139.

Berberian, M., and R. S. Yeats (2001), Contribution of archaeological data to studies of earthquake history in the Iranian Plateau, *J. Struct. Geol.*, *23*, 563-584.

Berberian, M., Jackson, J. A., Qorashi, M., and M. H. Kadjar (1984), Field and teleseismic observations of the 1981 Golbaf-Sirch earthquakes in SE Iran, *Geophys. J. R. astr. Soc.*, *77*, 809-838.

Berberian, M., Jackson, J. A., Fielding, E., Parsons, B. E., Priestly, K., Qorashi, M., Talebian, M., Walker, R., Wright, T. J., and C. Baker (2001), The 1998 March 14 Fandoqa earthquake ( $M_w$  6.6) in Kerman province, southeast Iran: re-rupture of the 1981 Sirch earthquake fault, triggering of slip on adjacent thrusts and the active tectonics of the Gowk fault zone, *Geophys. J. Int.*, *146*, 371-398.

Besse, J., Torcq, F., Gallet, Y., Ricou, L. E., Krystyn, L., and A. Saidi (1998), Late Permian to Late Triassic palaeomagnetic data from Iran: constraints on the migration of the Iranian block through the Tethyan Ocean and initial destruction of Pangaea, *Geophys. J. Int.*, *135*, 77-92.

Bonilla, M. G., and J. J. Lienkaemper (1990), Visibility of fault strands in exploratory trenches and timing of rupture events, *Geology*, *18*, 153-156.

Bøtter-Jensen, L., Thomsen, K. J., Jain, M. (2010), Review of optically stimulated luminescence (OSL) instrumental developments for retrospective dosimetry, *Radiat. Meas.*, *45*, 253-257, doi:10.1016/j.radmeas.2009.11.030.

Boyle, J. A. (1968), *The Cambridge History of Iran*, vol. 5: *The Saljuq and Mongol periods*, 763 pp., Cambridge Univ. Press, Cambridge.

Braucher, R., Merchel, S., Borgomano, J., Bourlès, D. L. (2011), Production of cosmogenic radionuclides at great depth: A multi element approach, *Earth Planet. Sci. Lett.*, 309, 1-9, doi:10.1016/j.epsl.2011.06.036.

Brown, E. T., Molnar, P., Bourlès, D. L. (2005), Comment on “Slip-rate measurements on the Karakorum fault may imply secular variations in fault motion”, *Science*, 309, 1326, doi:10.1126/science.1112508.

Cutler, K. B., Edwards, R. L., Taylor, F. W., Chen, H., Adkins, J., Gallup, C. D., Cutler, P. M., Burr, G. S., Bloom, A. L. (2003), Rapid sea-level fall and deep-ocean temperature change since the last interglacial period, *Earth Planet. Sci. Lett.*, 206, 253-271, doi:10.1016/S0012-821X(02)01107-X.

Dehghani, G. A., and J. Makris (1984), The gravity field and crustal structure of Iran, *N. Jb. Geol. Paläont. Abh.*, 168, 215-229.

Desilets, D., Zreda, M., Almasi, P. F., Elmore, D. (2006), Determination of cosmogenic  $^{36}\text{Cl}$  in rocks by isotope dilution: innovations, validation and error propagation, *Chem. Geol.*, 233, 185-195, doi:10.1016/j.chemgeo.2006.03.001.

Engdahl, E. R., van der Hilst, R., and R. Buland (1998), Global teleseismic earthquake relocation with improved travel times and procedures for depth determination, *Bull. Siesmol. Soc. Am.*, 88(3), 722-743.

Engdahl, E. R., Jackson, J. A., Myers, A. C., Bergman, E. A., and K. Priestley (2006), Relocation and assessment of seismicity in the Iran region, *Geophys. J. Int.*, 167, 761-778, doi:10.1111/j.1365-246X.2006.03127.x.

Fattahi, M., Nazari, H., Bateman, M. D., Meyer, B., Sébrier, M., Talebian, M., Le Dortz, K., Foroutan, M., Ahmadi Givi, F., Ghorashi, M. (2010), Refining the OSL age of the last

earthquake of the Dshir fault, Central Iran, *Quat. Geochronol.*, 5, 286-292, doi:10.1016/j.quageo.2009.04.005.

Fattahi, M., Walker, R. T., Talebian, M., Sloan, R. A., and A. Rasheedi (2011), The structure and late Quaternary slip rate of the Rafsanjan strike-slip fault, SE Iran, *Geosphere*, 7(5), 1159-1174, doi:10.1130/GES00651.1.

Fattahi, M., Walker, R. T., Talebian, M., Sloan, R. A., Rasheedi, A. (2014), Late Quaternary active faulting and landscape evolution in relation to the Gowk Fault in the South Golbaf Basin, S.E. Iran, *Geomorphology*, 204, 334-343.

Fielding, E. J., Wright, T. J., Muller, J., Parsons, B. E., Walker, R. (2004), Aseismic deformation of a fold-and-thrust belt imaged by synthetic aperture radar interferometry near Shahdad, southeast Iran, *Geology*, 32(7), 577-580, doi:10.1130/G20452.1.

Foroutan, M., Sébrier, M., Nazari, H., Meyer, B., Fattahi, M., Rashidi, A., Le Dortz, k., and M. D. Bateman (2012), New evidence for large earthquakes on the Central Iran plateau: palaeoseismology of the Anar fault, *Geophys. J. Int.*, 189(1), 6-18, doi:10.1111/j.1365-246X.2012.05365.x.

Frankel, K. L., and J. F. Dolan (2007), Characterizing arid region alluvial fan surface roughness with airborne laser swath mapping digital topographic data, *J. Geophys. Res.*, 112, F02025, doi:10.1029/2006JF000644.

Gosse, J. C., Phillips, F. M. (2001), Terrestrial in situ cosmogenic nuclides: theory and application, *Quat. Sci. Rev.*, 20, 1475-1560.

Grotes, P. M., and M. Stuiver (1997), Oxygen 18/16 variability in Greenland snow and ice with  $10^3$ - to  $10^5$ -year time resolution, *J. Geophys. Res.*, 102(C12), 24,455-26,470.

Guérin, G., Mercier, N., and G. Adamiec (2011), Dose-rate conversion factors: update, *Ancient TL*, 29(1), 5-8.

Hollingsworth, J., Jackson, J., Walker, R., Nazari, H. (2008), Extrusion tectonics and subduction in the eastern South Caspian region since 10 Ma, *Geology*, 36(10), 763-766, doi:10.1130/G25008A.1.

Kluyver, H. M., Tirrul, R., Chance, P. N., Johns, G. W., and H. M., Meixner (1983), Explanatory text of the Naybandan Quadrangle map, Quadrangle J8, scale 1:250,000, Geol. Surv. of Iran, Tehran.

Le Dortz, K., Meyer, B., Sébrier, M., Nazari, H., Braucher, R., Fattahi, M., Benedetti, L., Foroutan, M., Siame, L., Boulès, D., Talebian, M., Bateman, M. D., and M. Ghoraishi (2009), Holocene right-slip rate determined by cosmogenic and OSL dating on the Anar fault, Central Iran, *Geophys. J. Int.*, 179, 700-710, doi:10.1111/j.1365-246X.2009.04309.x.

Le Dortz, K., Meyer, B., Sébrier, M., Braucher, R., Nazari, H., Benedetti, L., Fattahi, M., Boulès, D., Foroutan, M., Siame, L., Rashidi, A., and M. D. Bateman (2011), Dating inset terraces and offset fans along the Dehshir Fault (Iran) combining cosmogenic and OSL methods, *Geophys. J. Int.*, 185, 1147-1174, doi:10.1111/j.1365-246X.2011.05010.x.

Le Dortz, K., Meyer, B., Sébrier, M., Braucher, R., Boulès, D., Benedetti, L., Nazari, H., Foroutan, M. (2012), Interpreting scattered *in-situ* produced cosmogenic nuclide depth-profile data, *Quat. Geochronol.*, 11, 98-115, doi:10.1016/j.quageo.2012.02.020.

Li, S.-H. (1994), Optical dating: insufficiently bleached sediments, *Radiat. Meas.*, 23(2/3), 563-567.

Mahdavi, M. A. (1996), Geological map of Ravar, Quadrangle I9, scale 1:250,000, Geol. Surv. of Iran, Tehran.

- Masson, F., Chéry, J., Hatzfeld, D., Martinod, J., Vernant, P., Tavakoli, F., and M. Ghafory-Ashtiani (2005), Seismic versus aseismic deformation in Iran inferred from earthquakes and geodetic data, *Geophys. J. Int.*, *160*, 217-226, doi:10.1111/j.1365-246X.2004.02465.x.
- Masson, F., Anvari, M., Djamour, Y., Walpersdorf, A., Tavakoli, F., Daignières, M., Nankali, H., and S. Van Gorp (2007), Large-scale velocity field and strain tensor in Iran inferred from GPS measurements: new insight for the present-day deformation pattern within NE Iran, *Geophys. J. Int.*, *170*, 436-440, doi:10.1111/j.1365-246X.2007.03477.x.
- Masson, F., Lehujeur, M., Ziegler, Y., and C. Doubre (2014), Strain rate tensor in Iran from a new GPS velocity field, *Geophys. J. Int.*, doi:10.1093/gji/ggt509, in press.
- McQuarrie, N., Stock, J. M., Verdel, C., and B. P. Wernicke (2003), Cenozoic evolution of Neotethys and implications for the causes of plate motions, *Geophys. Res. Lett.*, *30*(20), 2036, doi:10.1029/2003GL017992.
- Mériaux, A.-S., Tapponnier, P., Ryerson, F. J., Xiwei, X., King, G., Van der Woerd, J., Finkel, R. C., Haibing, L., Caffee, M. W., Zhiqin, X., and C. Wenbin (2005), The Aksay segment of the northern Altyn Tagh fault: Tectonic geomorphology, landscape evolution, and Holocene slip rate, *J. Geophys. Res.*, *110*, B04404, doi:10.1029/2004JB003210.
- Meyer, B., and K. Le Dortz (2007), Strike-slip kinematics in Central and Eastern Iran: Estimating fault slip-rates averaged over the Holocene, *Tectonics*, *26*, TC5009, doi:10.1029/2006TC002073.
- Murray, A. S., and J. M. Olley (2002), Precision and accuracy in the optically stimulated luminescence dating of sedimentary quartz: a status review, *Geochronometria*, *21*, 1-16.
- Murray, A. S. and A. G. Wintle (2000), Luminescence dating of quartz using an improved single-aliquot regenerative-dose protocol, *Radiat. Meas.*, *32*, 57-73.

- Murray, A. S. and A. G. Wintle (2003), The single aliquot regenerative dose protocol: potential for improvements in reliability, *Radiat. Meas.*, *37*, 377-381, doi:10.1016/S1350-4487(03)00053-2.
- Murray, A. S., Marten, R., Johnston, A., Martin, P. (1987), Analysis for naturally occurring radionuclides at environmental concentrations by gamma spectrometry, *J. Radioanal. Nucl. Chem. Art.*, *115*(2), 263-288.
- Murray, A. S., Thomsen, K. J., Masuda, N., Buylaert, J. P., Jain, M. (2012), Identifying well-bleached quartz using the different bleaching rates of quartz and feldspar luminescence signals, *Radiat. Meas.*, *47*, 688-696, doi:10.1016/j.radmeas.2012.05.006.
- Nalbant, S. S., Steacy, S., and J. McCloskey (2006), Stress transfer relations among the earthquakes that occurred in Kerman province, southern Iran since 1981, *Geophys. J. Int.*, *167*, 309-318, doi:10.1111/j.1365-246X.2006.03119.x.
- Nazari, H., Fattahi, M., Meyer, B., Sébrier, M., Talebian, M., Foroutan, M., Le Dortz, K., Bateman, M. D., and M. Ghorashi (2009), First evidence for large earthquakes on the Deshir Fault, Central Iran Plateau, *Terra Nova*, *21*, 417-426, doi:10.1111/j.1365-3121.2009.00892.x.
- NIOC (1977), Geological map of Iran, *Sheet 6, south-east Iran*, scale 1:1,000,000, Natl. Iran. Oil Co., Explor. and Prod., Tehran.
- Olley, J. M., Caitcheon, G. G., Roberts, R. G. (1999), The origin of dose distributions in fluvial sediments, and the prospect of dating single grains from fluvial deposits using optically stimulated luminescence, *Radiat. Meas.*, *30*, 207-217.

- Peltzer, G., Tapponnier, P., Gaudemer, Y., Meyer, B., Guo, S., Yin, K., Chen, Z., and H. Dai (1988), Offsets of late Quaternary morphology, rate of slip, and recurrence of large earthquakes on the Chang Ma fault (Gansu, China), *J. Geophys. Res.*, *93*, 7793-7812.
- Phillips, W. M., Sloan, V. F., Shroder Jr., J. F., Sharma, P., Clarke, M. L., Rendell, H. M. (2000), Asynchronous glaciation at Nanga Parbat, northwestern Himalaya Mountains, Pakistan, *Geology*, *28*(5), 431-434.
- Prescott, J. R., and J. T. Hutton (1994), Cosmic ray contributions to dose rates for luminescence and ESR dating: large depths and long-term time variations, *Radiat. Meas.*, *23*(2/3), 497-500.
- Regard, V., Bellier, O., Thomas, J. -C., Bourlès, D., Bonnet, S., Abbassi, M. R., Braucher, R., Mercier, J., Shabanian, E., Soleymani, Sh., and Kh. Fegghi (2005), Cumulative right-lateral fault slip rate across the Zagros-Makran transfer zone: role of the Minab-Zendan fault system in accommodation Arabia-Eurasia convergence in southeast Iran, *Geophys. J. Int.*, *162*, 177-203, doi:10.1111/j.1365-246X.2005.02558.x.
- Regard, V., Hatzfeld, D., Molinaro, M., Aubourg, C., Bayer, R., Bellier, O., Yamini-Fard, F., Peyret, M., and M. Abbassi (2010), The transition between Makran subduction and the Zagros collision: recent advances in its structure and active deformation, in *Tectonic and Stratigraphic Evolution of Zagros and Makran during the Mesozoic-Cenozoic*, edited by Leturmy, P., and Robin, C., *Geol. Soc. Lond. Spec. Publ.*, *330*, 43-64, doi:10.1144/SP330.4.
- Rizza, M., Mahan, S., Ritz, J.-F., Nazari, H., Hollingsworth, J., Salamati, R. (2011a), Using luminescence dating of coarse matrix material to estimate the slip rate of the Astaneh fault, Iran, *Quat. Geochronol.*, *6*, 390-406.

- Rizza, M., Ritz, J.-F., Braucher, R., Vassallo, R., Prentice, C., Mahan, S., McGill, S., Chauvet, A., Marco, S., Todbileg, M., Demberel, S., and D. Bourlès (2011b), Slip rate and slip magnitudes of past earthquakes along the Bogd left-lateral strike-slip fault (Mongolia), *Geophys. J. Int.*, 186, 897-927, doi:10.1111/j.1365-246X.2011.05075.x.
- Sahandi, M. R. (1992), Geological map of Kerman, Quadrangle *J10*, scale 1:250,000, Geol. Surv. of Iran, Tehran.
- Schimmelpfennig, I., Benedetti, L., Finkel, R., Pik, R., Blard, P.-H., Bourlès, D., Burnard, P., Williams, A. (2009), Sources of in-situ  $^{36}\text{Cl}$  in basaltic rocks. Implication for calibration of production rates, *Quat. Geochronol.*, 4, 441-461, doi:10.1016/j.quageo.2009.06.003.
- Schimmelpfennig, I., Benedetti, L., Garreta, V., Pik, R., Blard, P.-H., Burnard, P., Bourlès, D., Finkel, R., Ammon, K., Dunai, T. (2011), Calibration of cosmogenic  $^{36}\text{Cl}$  production rates from Ca and K spallation in lava flows from Mt. Etna (38°N, Italy) and Payun Matru (36°S, Argentina), *Geochim. Cosmochim. Acta*, 75, 2611-2632, doi:10.1016/j.gca.2011.02.013.
- Sieh, K. E., and Jahns, R. H. (1984), Holocene activity of the San Andreas fault at Wallace Creek, California, *Geol. Soc. Am. Bull.*, 95, 883-896.
- Soheili, M. (1995), Geological map of Sirjan, Quadrangle *III*, scale 1:250,000, Geol. Surv. of Iran, Tehran.
- Staubwasser, M., Sirocko, F., Grootes, P.M., and M. Segl (2003), Climate change at the 4.2 ka BP termination of the Indus valley civilization and Holocene south Asian monsoon variability, *Geophys. Res. Lett.*, 30(8), 1425, doi:10.1029/2002GL016822.
- Stöcklin, J., and Nabavi, M. H. (1969), Geological map of Boshruyeh, Quadrangle *J7*, scale 1:250,000, Geol. Surv. of Iran, Tehran.

Stone, J. O., Allan, G. L., Fifield, L. K., and R. G. Cresswell (1996), Cosmogenic chlorine-36 from calcium spallation, *Geochim. Cosmochim. Acta*, 60(4), 679-692.

Stone, J. O., Evans, J. M., Fifield, L. K., Allan, G. L., and R. G. Cresswell (1998), Cosmogenic chlorine-36 production in calcite by muons, *Geochim. Cosmochim. Acta*, 62(3), 433-454.

Talebian, M., Biggs, J., Bolourchi, M., Copley, A., Ghassemi, A., Ghorashi, M., Hollingsworth, J., Jackson, J., Nissen, E., Oveisi, B., Parsons, B., Priestley, K., and A. Saiidi (2006), The Dahuiyeh (Zarand) earthquake of 2005 February 22 in central Iran: reactivation of an intramountain reverse fault, *Geophys. J. Int.*, 164, 137-148, doi:10.1111/j.1365-246X.2005.02839.x.

Vahdati Daneshmand, F. (1992), Geological map of Rafsanjan, Quadrangle 110, scale 1:250,000, Geol. Surv. of Iran, Tehran.

Vassallo, R., Ritz, J.-F., Braucher, R., Jolivet, M., Carretier, S., Larroque, C., Chauvet, A., Sue, C., Todbileg, M., Bourlès, D., Arzhannikova, A., and S. Arzhannikov (2007), Transpressional tectonics and stream terraces of the Gobi-Altay, Mongolia, *Tectonics*, 26, TC5013, doi:10.1029/2006TC002081.

Vernant, Ph., Nilforoushan, F., Hatzfeld, D., Abbassi, M. R., Vigny, C., Masson, F., Nankali, H., Martinod, J., Ashtiani, A., Bayer, R., Tavakoli, F., and J. Chéry (2004), Present-day crustal deformation and plate kinematics in the Middle East constrained by GPS measurements in Iran and northern Oman, *Geophys. J. Int.*, 157, 381-398, doi:10.1111/j.1365-246X.2004.02222.x.

Walker, F., and M. B. Allen (2012), Offset rivers, drainage spacing and the record of strike-slip faulting: The Kuh Banan Fault, Iran, *Tectonophysics*, 530-531, 251-263, doi:10.1016/j.tecto.2012.01.001.

Walker, R., and J. Jackson (2002), Offset and evolution of the Gowk fault, S.E. Iran: a major intra-continental strike-slip system, *J. Struct. Geol.*, 24, 1677-1698.

Walker, R., and J. Jackson (2004), Active tectonics and late Cenozoic strain distribution in central and eastern Iran, *Tectonics*, 23, TC5010, doi:10.1029/2003TC001529.

Walker, R., Jackson, J., and C. Baker (2003), Surface expression of thrust faulting in eastern Iran: source parameters and surface deformation of the 1978 Tabas and 1968 Ferdows earthquake sequences, *Geophys. J. Int.*, 152, 749-765.

Walker, R. T., Gans, P., Allen, M. B., Jackson, J., Khatib, M., Marsh, N., and M. Zarrinkoub (2009), Late Cenozoic volcanism and rates of active faulting in eastern Iran, *Geophys. J. Int.*, 177, 783-805, doi:10.1111/j.1365-246X.2008.04024.x.

Walker, R. T., Talebian, M., Saiffori, S., Sloan, R. A., Rashidi, A., MacBean, N., Ghassemi, A. (2010a), Active faulting, earthquakes, and restraining bend development near Kerman city in southeastern Iran, *J. Struct. Geol.*, 32, 1046-1060, doi:10.1016/j.jsg.2010.06.012.

Walker, R. T., Talebian, M., Sloan, R. A., Rashidi, A., Fattahi, M., and C. Bryant (2010b), Holocene slip-rate on the Gowk strike-slip fault and implications for the distribution of tectonic strain in eastern Iran, *Geophys. J. Int.*, 181, 221-228, doi:10.1111/j.1365-246X.2010.04538.x.

Walker, R. T., Khatib, M. M., Bahroudi, A., Rodés, A., Schnabel, C., Fattahi, M., Talebian, M., Bergman, E. (2013), Co-seismic, geomorphic, and geologic fold growth associated

with the 1978 Tabas-e-Golshan earthquake fault in eastern Iran, *Geomorphology*, doi:10.1016/j.geomorph.2013.02.016, in press.

Wallinga, J. (2001), The Rhine-Meuse system in a new light: optically stimulated luminescence dating and its application to fluvial deposits, *PhD thesis*, 180 pp., Faculty of Geographical Sciences, Utrecht University, Utrecht, Netherlands.

Walpersdorf A., Manighetti, I., Mousavi, Z., Tavakoli, F., Vergnolle, M., Jadidi, A., Hatzfeld, D., Aghamohammadi, A., Bigot, A., Djamour, Y., Nankali, H., and M. Sedighi (2014), Present-day kinematics and fault slip rates in Eastern Iran, derived from 11 years of GPS data, *J. Geophys. Res.*, doi:10.1002/2013JB010620, in press.

Weldon, R. J., and Sieh, K. E. (1985), Holocene rate of slip and tentative recurrence interval for large earthquakes on the San Andreas fault, Cajon Pass, southern California, *Geol. Soc. Am. Bull.*, 96, 793-812.

Wellman, H. W. (1966), Active wrench faults of Iran, Afghanistan and Pakistan, *Geol. Rundsch.*, 55(3), 716-735.

Wells, D. L., and K. J. Coppersmith (1994), New empirical relationships among magnitude, rupture length, rupture width, rupture area, and surface displacement, *Bull. Seismol. Soc. Am.*, 84(4), 974-1002.

Zanchi, A., Zanchetta, S., Garzanti, E., Balini, M., Berra, F., Mattei, M., and G. Muttoni (2009), The Cimmerian evolution of the Nakhlak-Anarak area, Central Iran, and its bearing for the reconstruction of the history of the Eurasian margin, in *South Caspian to Central Iran Basins*, edited by Brunet, M.-F., Wilmsen, M., and J. W. Granath, *Geol. Soc. Lond. Spec. Publ.*, 312, 261-286.

Zreda, M. G., Phillips, F. M., Elmore, D., Kubik, P. W., Sharma, P., and R. I. Dorn (1991),

Cosmogenic chlorine-36 production rates in terrestrial rocks, *Earth Planet. Sci. Lett.*, 105, 94-109.

Accepted Article

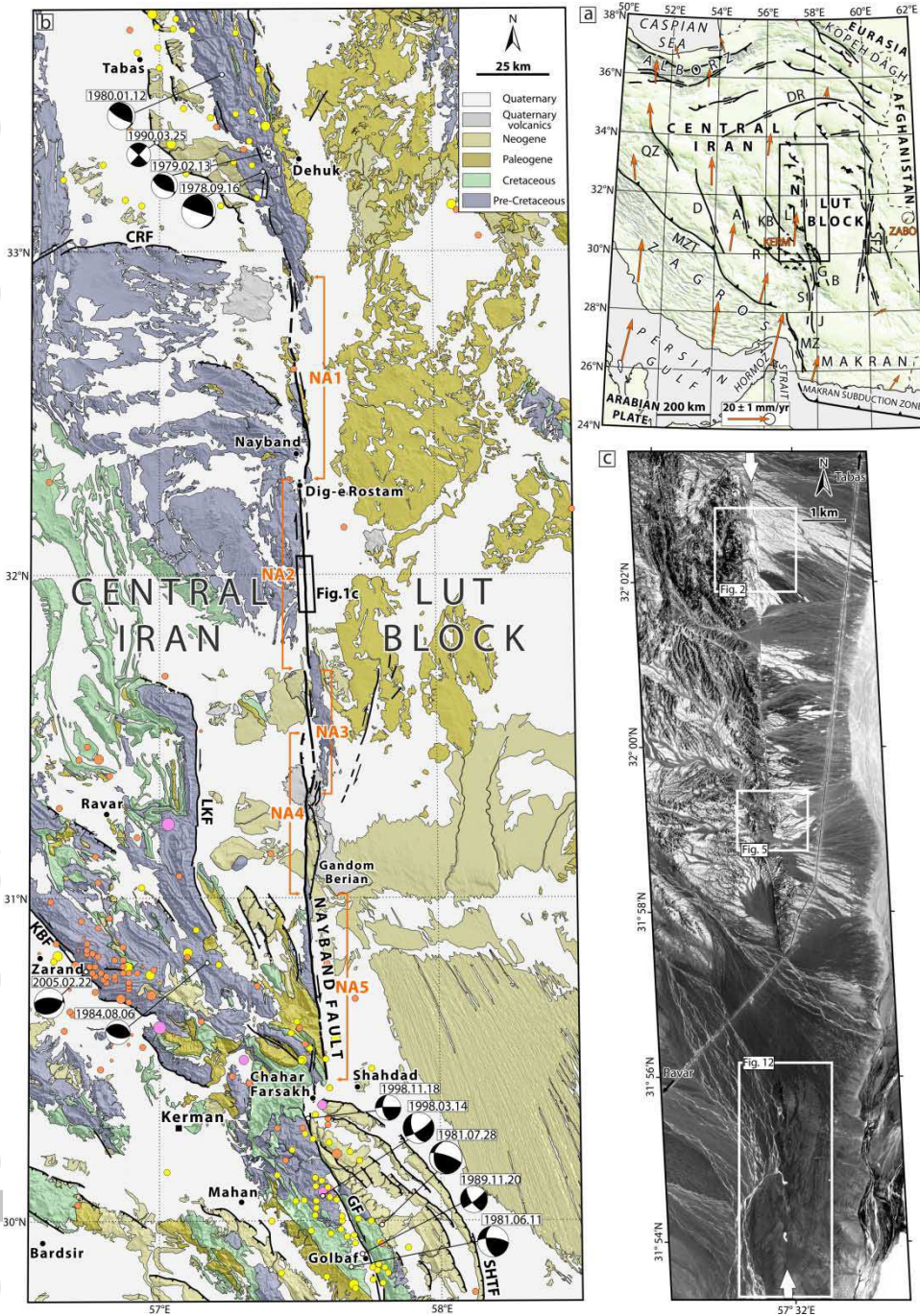


**Figure 1.** (a) Map of the major active faults in Central and Eastern Iran superimposed on the shaded DEM map. A, Anar fault; B, Bam fault; D, Dehshir fault; DR, Doruneh fault; G, Gowk fault; J, Jiroft fault; KB, Kuh Banan fault; L, Lakar Kuh fault; MZ, Minab-Zendan fault system; MZT, Main Zagros Thrust fault; QZ, Qom-Zefreh fault; R, Rafsanjan fault; S, Sabzevaran fault; and SFZ, Sistan Fault Zone. GPS velocities (orange arrows) in Eurasian-fixed reference frame with 95 per cent confidence ellipse for ZABO site from *Vernant et al.*

[2004] and *Masson et al.* [2007]. The velocity of ZABO site does not present significant motion relative to Eurasia. Black box shows the location of Figure 1b. (b) Simplified seismotectonic map of east-Central Iran and western Lut Block. Regional geology compiled from *Stöcklin and Nabavi* [1969], *Aghanabati* [1974, 1993], *NIOC* [1977], *Alavi-Naini and Griffis* [1981a, 1981b], *Vahdati Daneshmand* [1992], *Sahandi* [1992], *Soheili* [1995], and *Mahdavi* [1996], overlain on shaded relief 90-m SRTM Digital Elevation Model. Active fault traces (dashed where inferred) from Landsat, SPOT, Quickbird imageries and field observations. CRF, Cheshmeh Rostam Fault; GF, Gowk Fault; KBF, Kuh Banan Fault; LKF, Lakar Kuh Fault; and SHTF, Shahdad Thrust Faults. Orange circles are epicenters of most recent (2004-2012) earthquakes ( $m_b > 3$ ) from the NEIC catalog (<http://earthquake.usgs.gov/earthquakes/eqarchives/epic/>). Yellow circles are epicenters of recent (1918-2004) earthquakes from *Engdahl et al.* [2006]. Violet circles are historical epicenters of older (before 1918) earthquakes from *Ambraseys and Melville* [1982]. Well-constrained fault-plane solutions are indicated (see Table 1 for source parameters). Note the lack of instrumental and historical seismicity in the neighborhood of the Nayband fault trace. Black box shows the location of Figure 1c. (c) Raw Quickbird imagery (pixel-size, 60 cm) showing the trace of the Nayband fault (white arrows) cutting mostly across Pleistocene-Holocene alluvial fans and Neogene marls (whitish parts). Streams and gullies incised within alluvial fans show right-lateral offsets ranging from several meters to several hundred meters. Boxes show the locations of site North (Figure 2, along single straight fault portion), site South (Figure 5, along a 100-m-wide step-over) and paleoseismic trench site (Figure 12).

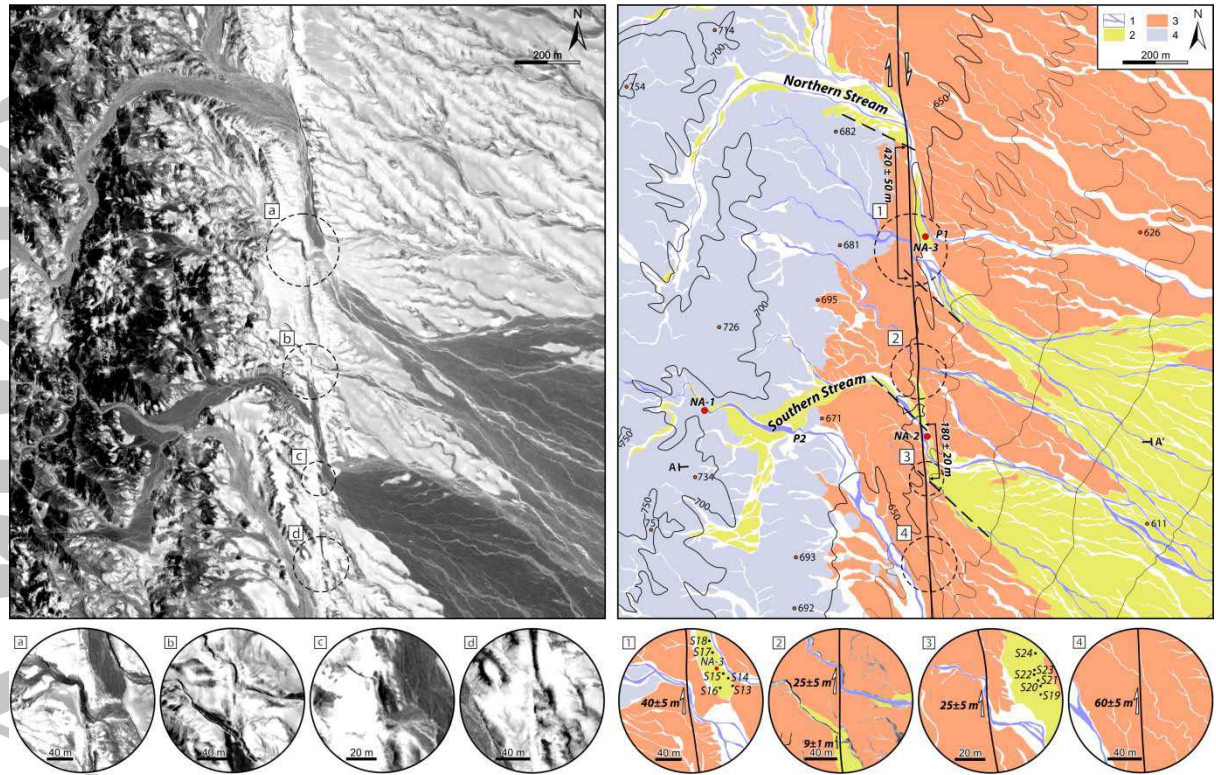


**Figure 2.** Site North. (Left) Quickbird imagery of the Nayband fault across the Quaternary alluvial deposits and Neogene marls. Dashed circles indicate recent right-lateral offset streams. (Right) Corresponding geologic map adapted from Quickbird imagery, field observations and regional geology [Alavi-Naini and Griffis, 1981a]. Contour lines and elevation points in meters, asl, derived from 1:25,000 topographic map (National Cartographic Center of Iran; Sheet No. 7554-III SW). Main contour interval is 50 m. Intermediate contours, every 10 m are represented east of the fault. Red dots locate the OSL samples collected from the abandoned alluvial fans and the most recent risers of incised stream. P1 and P2 are Recent stream piracies. 1, active channels; 2, Recent alluvial fans and terraces of Holocene and late-Pleistocene ages; 3, poorly consolidated Neogene marls and sandstones; 4, Triassic shales and sandstones. Dashed circles denote locations of raw (a, b, c, d) and interpreted (1, 2, 3, 4) Quickbird enlargements. Black dots locate the  $^{36}\text{Cl}$  samples collected on the surface of the alluvial fans (see text for discussion).

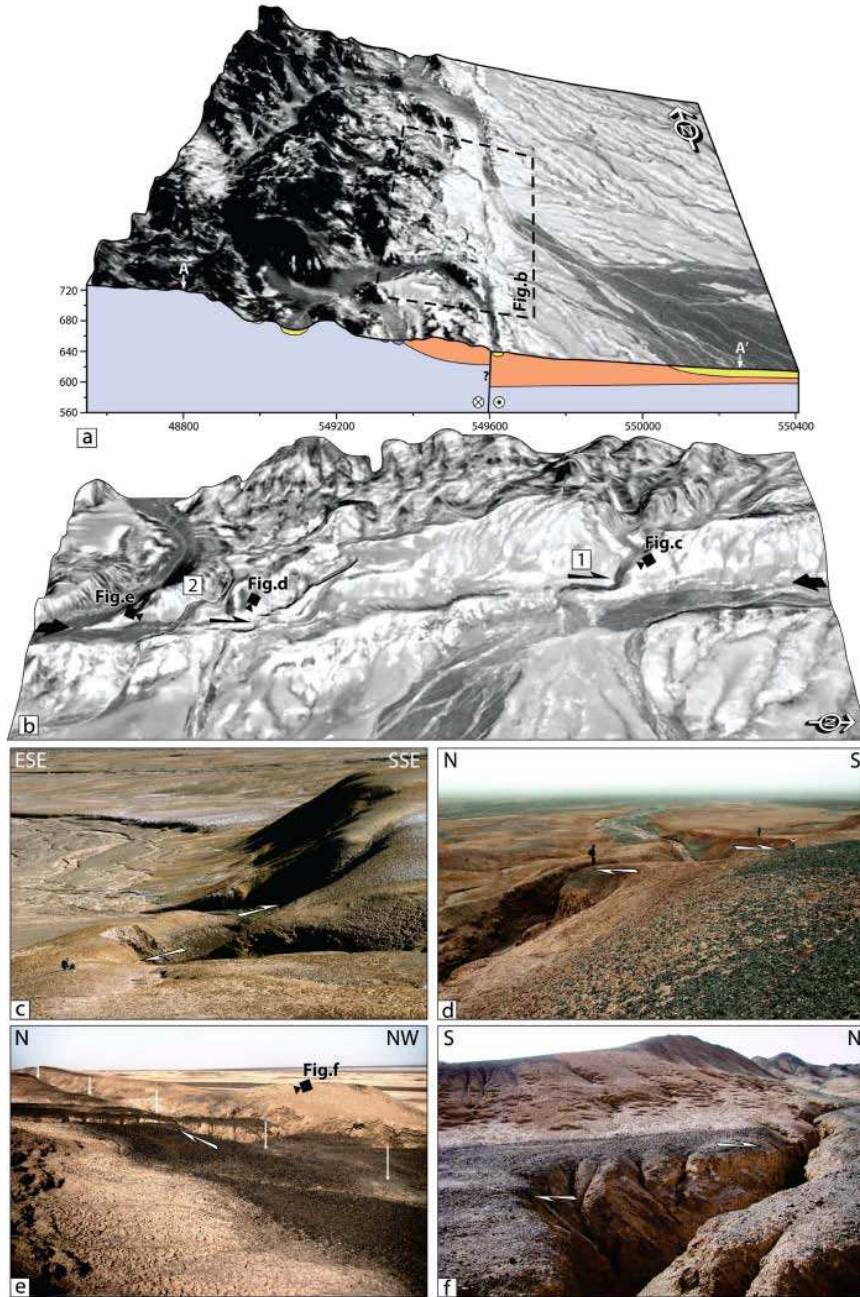


**Figure 3.** (a) 3D perspective diagram (vertical exaggeration=2) of site North and surrounding area obtained by draping the Quickbird imagery over the shaded relief Digital Elevation Model extracted from 1:25,000 topographic data. The Nayband fault trace makes the transition between Quaternary alluvial fans and Neogene piedmont deposits, east of smoothed hills made of Triassic rocks. Simplified cross-section schematizes the relations between units (see Figure 2 for location). Color codes as in Figure 2. (b) Perspective view

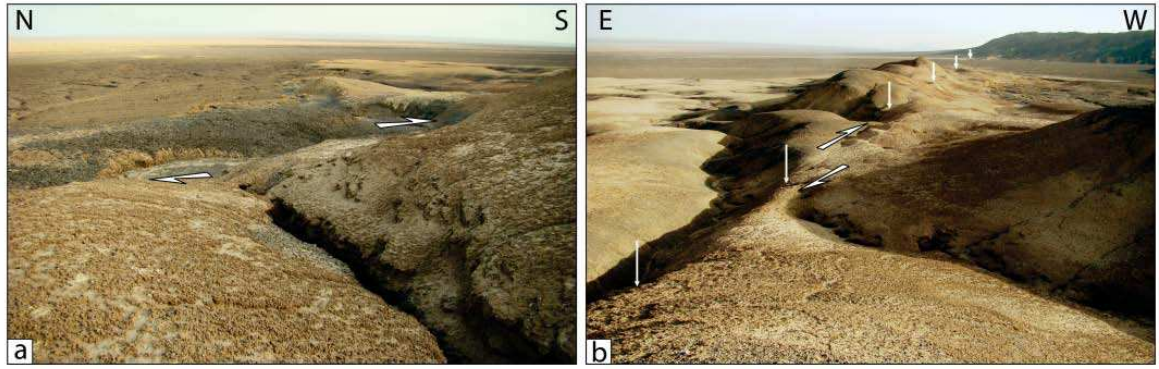
highlights the recent offset streams 1 and 2 by the fault trace (see Figure 2 for location). (c-f)

Field photographs of three dextral offsets; c: right-lateral dogleg offset of  $40 \pm 5$  m (square 1

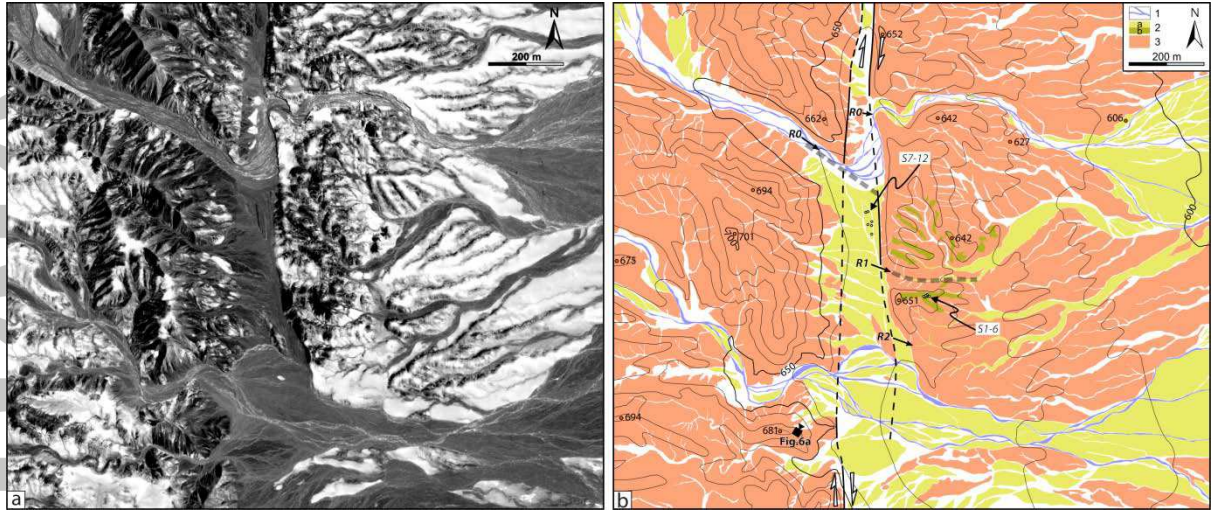
on Figure 2); d: right-lateral offset of an incised ( $\sim 15$  m) channel by  $25 \pm 5$  m (square 2 on

Figure 2); e-f: different views of  $9 \pm 1$  m offset preserved by an incised ( $\sim 3.3$  m) gully.

Accepted Article



**Figure 4.** Field photographs of two offset channels at the site North (see squares 3 and 4 on Figure 2 for locations). (a) View to the east of an ephemeral gully incised into poorly consolidated Neogene marls that are partially covered by younger alluvial fan deposits. Its offset amounts to  $25 \pm 5$  m (square 3 on Figure 2). (b) View to the south of right-lateral offset of an intermittent channel by  $60 \pm 5$  m, which is incised within poorly consolidated Neogene marls (square 4 on Figure 2).



**Figure 5.** Site South. (a) Raw Quickbird imagery of a 100-m wide step-over along the segment NA2 of the Nayband fault. (b) Corresponding geologic map adapted from Quickbird imagery, field observations and regional geology [Alavi-Naini and Griffis, 1981b]. 1, active channels; 2, Recent alluvial fans and terraces of (2a) Holocene, and (2b) late-Pleistocene ages; 3, poorly consolidated Neogene marls and sandstones. Contour interval from 1:25,000 topographic data is 10 m. White dots locate the  $^{36}\text{Cl}$  surface samples. R1 and R2 designate two wind-gaps on the eastern side of the fault trace.

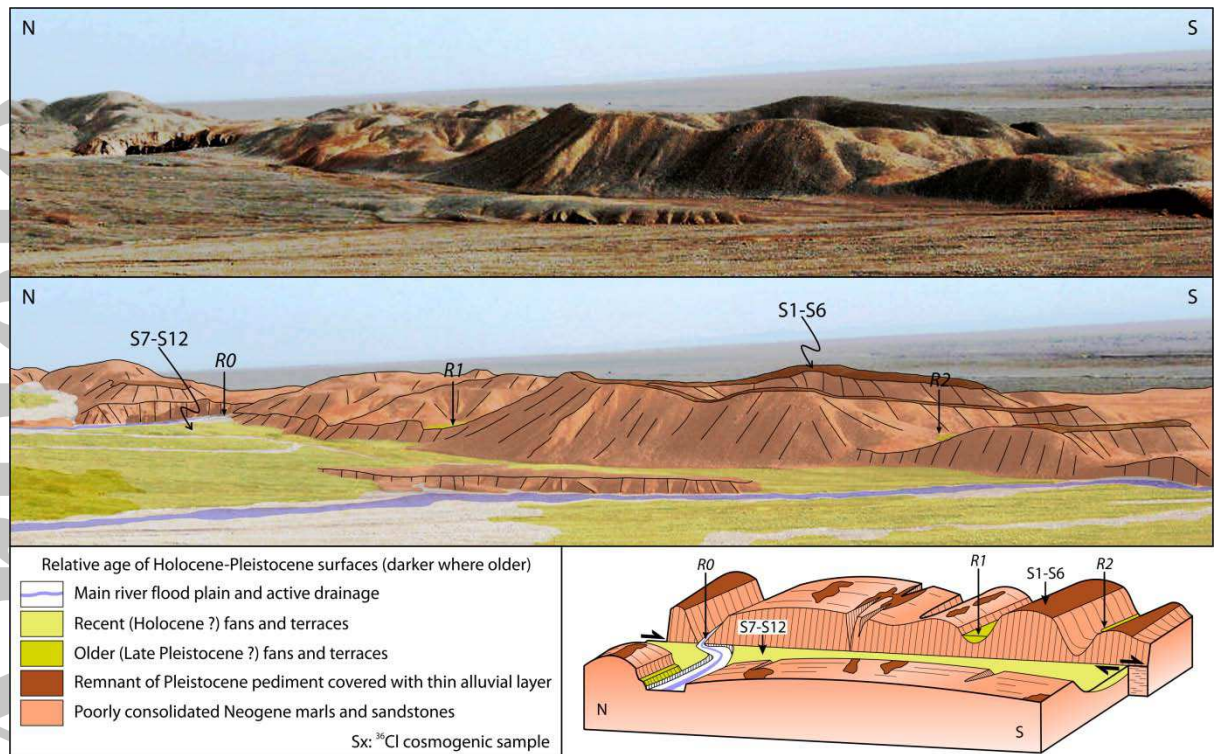


**Figure 6.** (a) A panoramic view of eastern part of site South, looking northeast (see Figure 5b for location). The fault trace runs nearby the base of a scarp between Neogene marls and Quaternary alluvial deposits. (b) Interpretative sketch shows remnants of Pleistocene alluvial surface (green shading) locally preserved on top of Neogene deposits (orange shading). The Neogene deposits are incised by two main channels (R1 and R2) on the eastern side of the fault trace. Recent alluvial fans and terraces (light-yellow shading) are incised by flood plain active rivers (white-blue shading). Locations of <sup>36</sup>Cl surface samples are shown by black curvy-arrows. (c) Schematic diagram highlights two beheaded wind-gaps (R1 and R2) south of the ongoing incision of active river (R0).

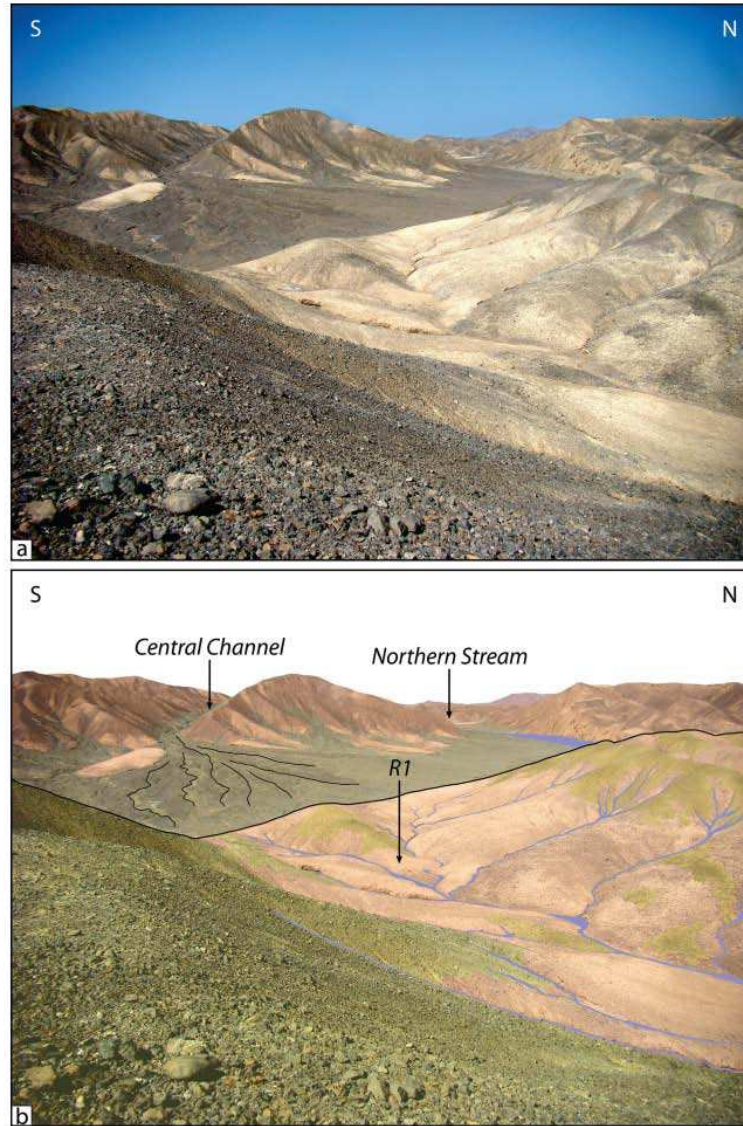


**Figure 7.** Field photograph (a) and interpretative sketch (b) of the northern stream (R0) west of the fault zone taken from R1 east of the fault zone. The central channel, west of the fault, is located almost in front of R1. Thick black line denotes the top of the scarp pointing to the trace of EFS. Pink and gray shadings are for Neogene marls and Quaternary alluvial fans, respectively. East of the fault, scarce remnants of late Pleistocene alluvial fan deposits (green shading) are preserved on top of the Neogene marls.

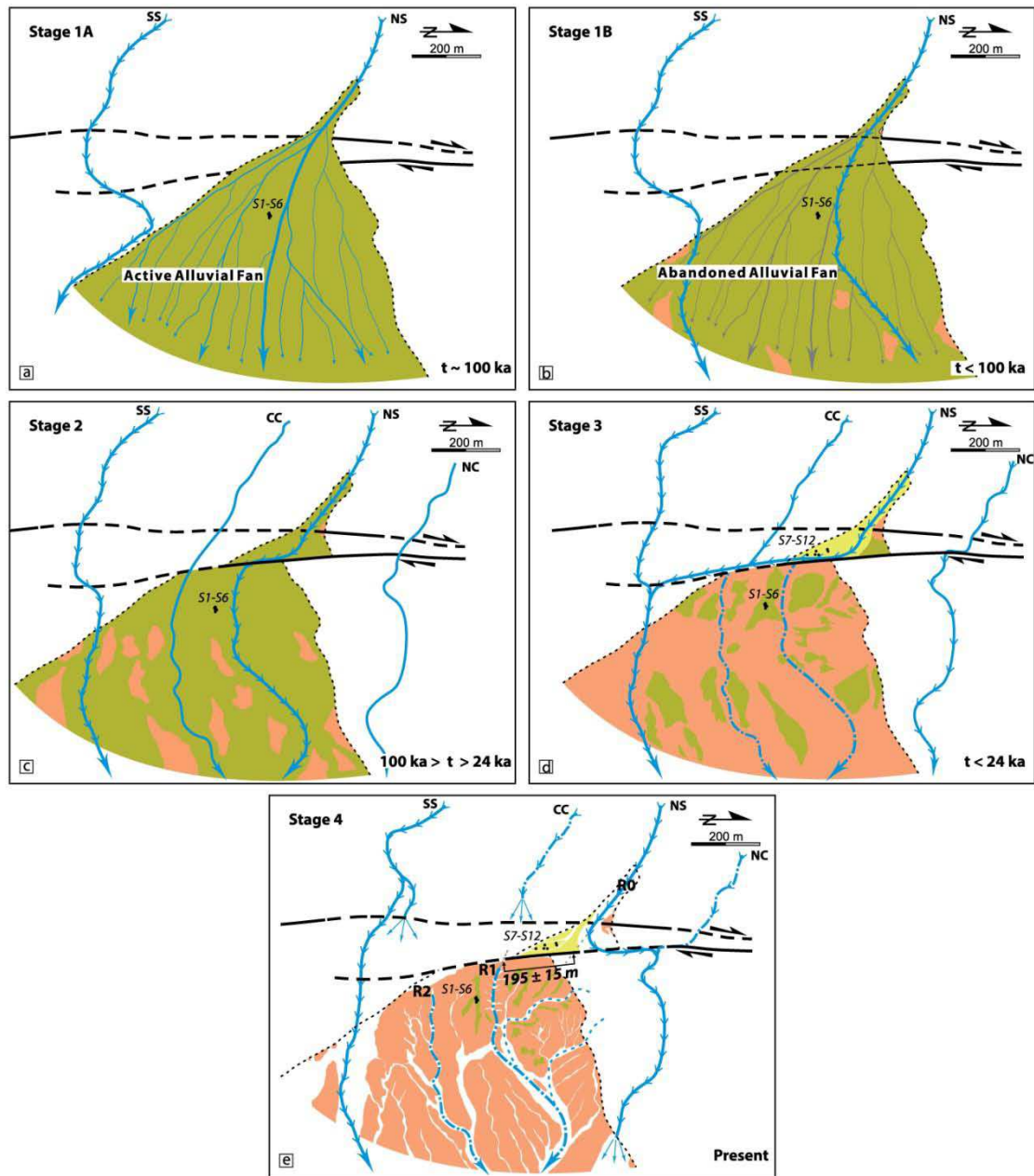


**Figure 8.** Late Pleistocene-Holocene morphotectonic evolution of the landform of site South. Stage (1A): Emplacement of a large alluvial fan at the outlet of a northern stream (NS), close to the fault zone. The fault traces are buried by the fan aggradation covering the uppermost layers of Neogene marls during a phase of sedimentary discharge (~100 ka, see section 3.3.1). A southern stream (SS) flows along the southern edge of the alluvial fan. Black dots (S1-S6) indicate the locations where the corresponding  $^{36}\text{Cl}$  samples will be

collected. Stage (1B): By the end of the aggradation of the fan, an erosion phase coeval with incision of the northern stream, piracy of the southern stream, abandonment of the fan surface and progressive exposure of patches of Neogene marls (orange shading) due to regressive erosion within small rills and channels (gray lines). Stage (2): Ongoing erosion processes and regressive erosion coeval with the formation of central (CC) and northern (NC) channels and the increase of the cumulative right-lateral offsets of the northern (NS) and southern (SS) stream courses. The progressive offset of the northern stream shifts the down-fault course towards the South. Stage (3): Further right-lateral slip and coeval incision produces larger cumulative offsets and the abandonment of the CC, NS and NC downstream from the fault zone (dashed blue lines). As the downstream courses of the central channel and northern stream are defeated, the remaining stream to the south (SS) captures the upstream courses of the defeated streams. A younger alluvial fan (yellow shading) has emplaced (after 24 ka, oldest possible age of the youngest pebble, sample S12, see section 3.3.1) in the small depression sited between the western and eastern fault strands. Black dots (S7-S12) indicate the locations where the corresponding  $^{36}\text{Cl}$  samples will be collected. Stage (4): Present-day situation. The northern stream has registered  $195 \pm 15$  m of right-lateral offset. Lowering of the local base level, coeval incision and right-lateral motion along the fault resulted in the piracy of its upstream course now flowing into the downstream course of NC. The erosion processes reduced the exposures of the older fan which scarce remnants cap the Neogene marls.

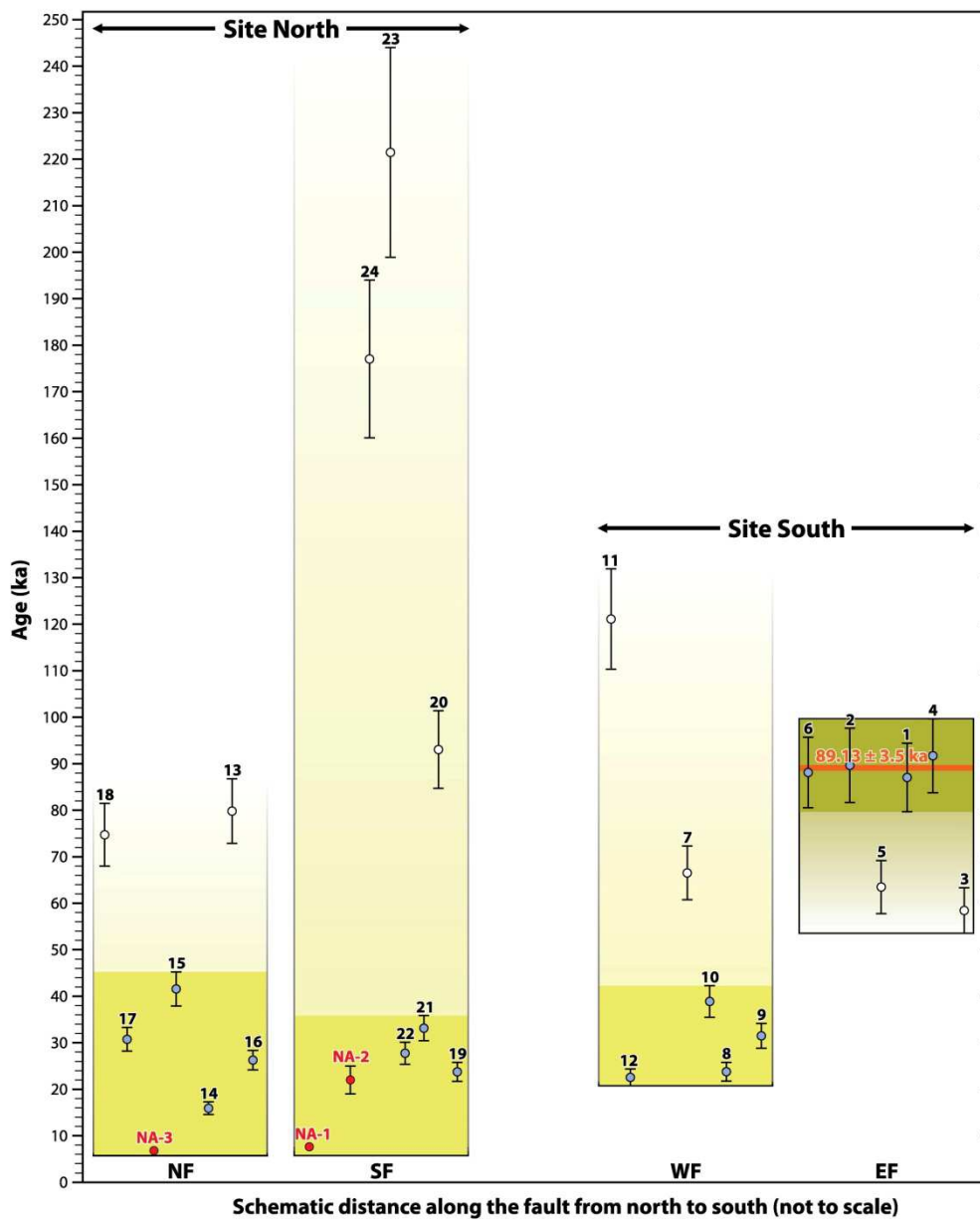


**Figure 9.** Plot of  $^{36}\text{Cl}$  and OSL ages for alluvial surfaces at the sites North and South, in schematic position from north to south. Dots and error bars are in blue and red for  $^{36}\text{Cl}$  and OSL, respectively. Dark-shaded areas pointing the average standard deviation for the  $^{36}\text{Cl}$  retained samples. Thick orange line represents the average age of eastern, older, surface at the site South after excluding outliers (white dots and lighter-shaded areas).

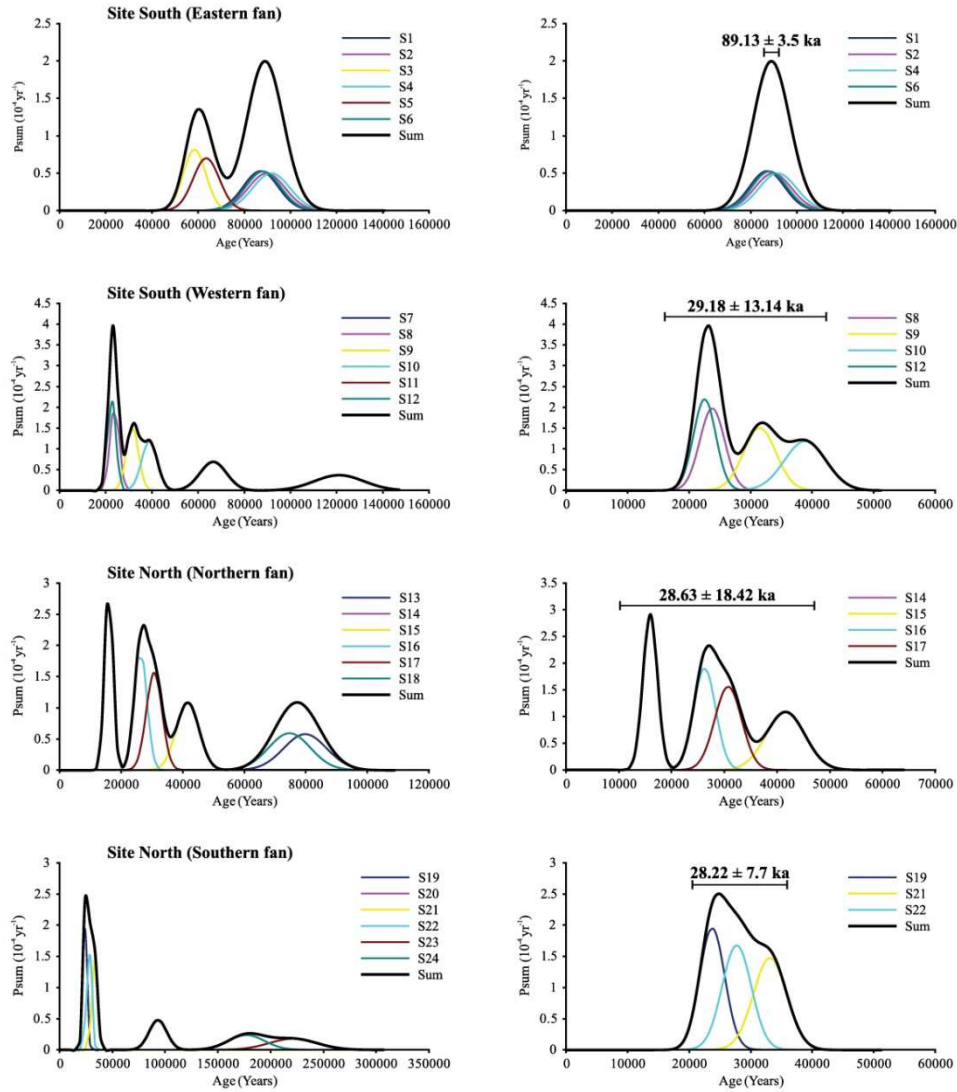


**Figure 10.** Distribution of *in-situ*  $^{36}\text{Cl}$  CRE ages, modeled with no erosion and no inheritance, for the surface samples collected on the alluvial fan surfaces at the sites North and South, including (left panel) and discarding (right panel) outlier samples. The thin colored curves represent the CRE age probability as Gaussian distribution for each sample while the thick black curves correspond to the summed Gaussian probability density function. The weighted mean CRE ages for each alluvial fan surface are obtained with errors equal to two standard deviations ( $2\sigma$ ).

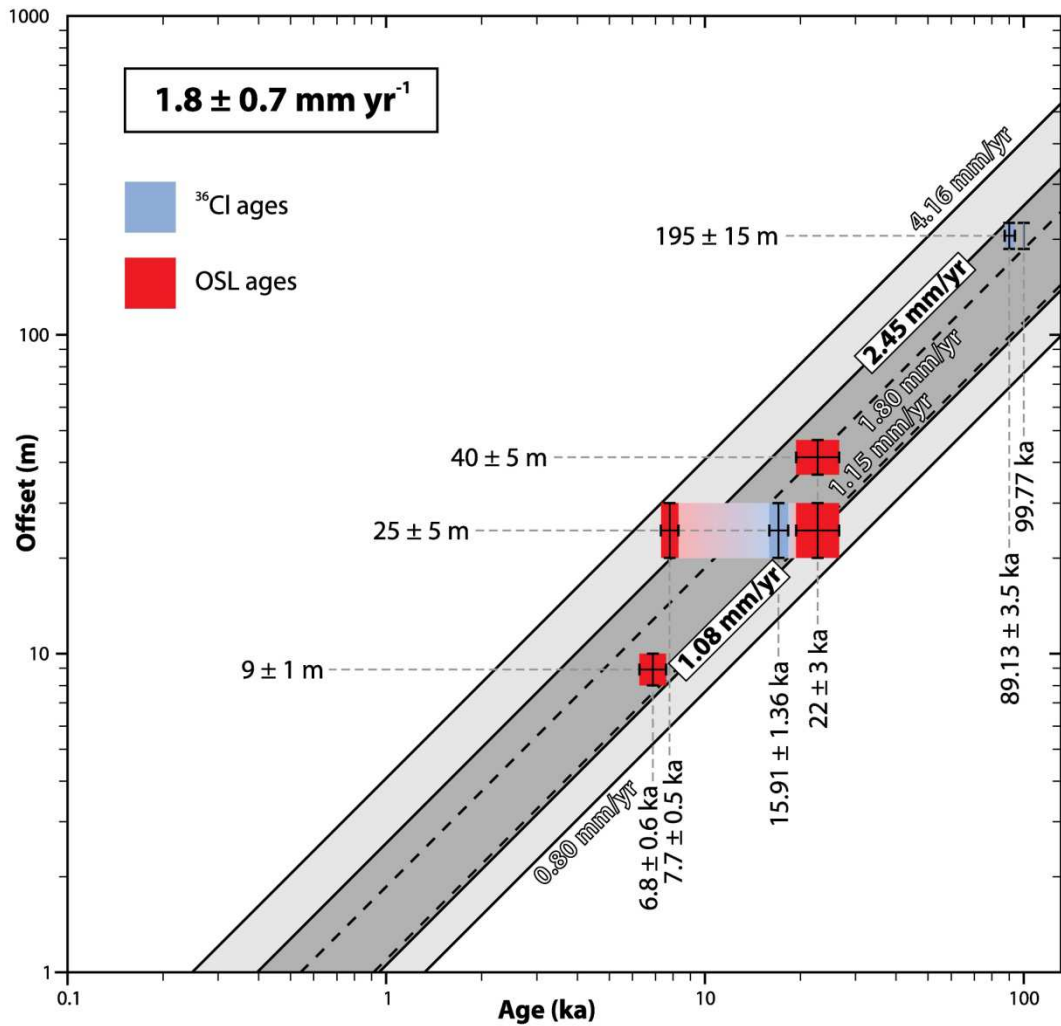


**Figure 11.** Summary of right-slip rates deduced from geomorphic offsets combined with cosmogenic and OSL dating at the sites North and South. Red and blue boxes based on the OSL and  $^{36}\text{Cl}$  CRE ages, respectively. The light gray domains denote maximum and minimum slip rates based on the OSL dating. The dark gray domain that refines the minimum and maximum rates is based on  $^{36}\text{Cl}$  CRE dating. The slip rate averaged over the last 100 ka is  $1.8 \pm 0.7 \text{ mm yr}^{-1}$  (see section 3.4 for discussion).

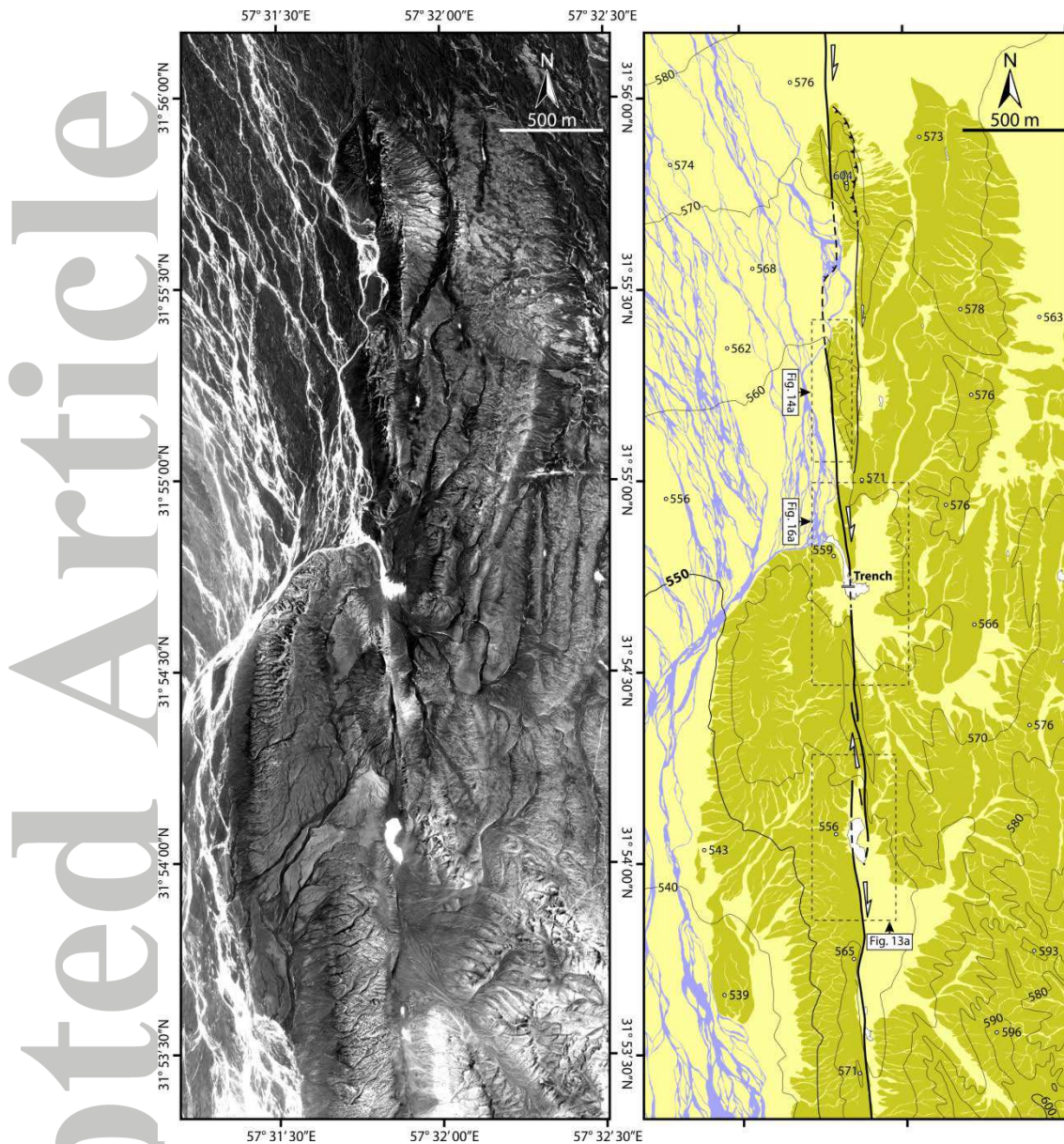


**Figure 12.** Central portion of the Nayband fault. Raw Quickbird imagery (a) and interpretation (b) (see Fig. 1c for location). Regional geology adapted from field observations and geological map [Alavi-Naini and Griffis, 1981b]. Contour lines with 10-m-interval and elevation points in meters (asl) derived from 1:25,000 topographic map (National Cartographic Center of Iran; Sheet No. 7553-IV NW). Recent ponds (white areas) located across releasing bend and step-over geometries. A compressional step-over within older deposits (dark yellow) to the north delineates a narrow ridge peaking at 604 m (asl). Boxes show the locations of Figures 13a, 14a and 16a.

Accepted Article

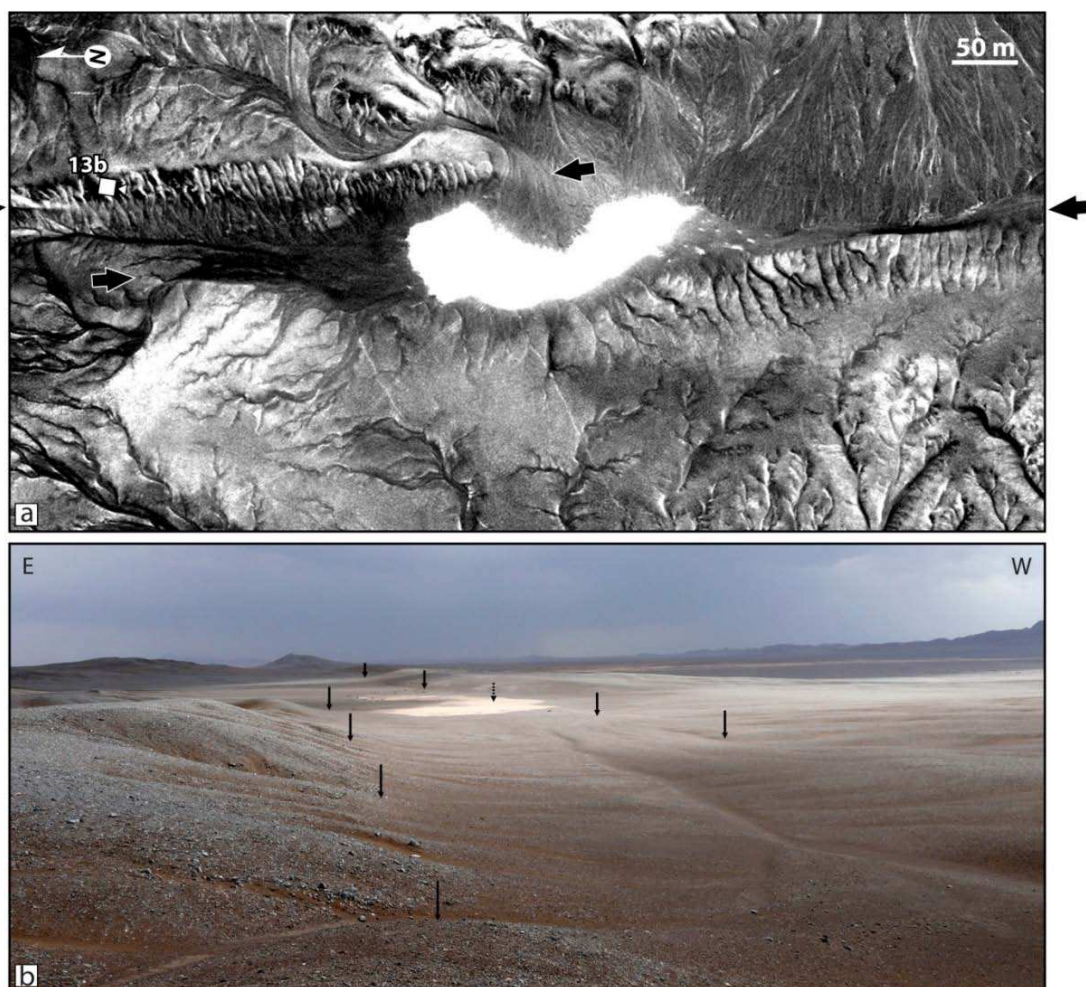


**Figure 13.** (a) Raw Quickbird imagery of a local pull-apart within releasing step-over along the Nayband fault. See Figure 12b for location. Black arrows delineate the fault traces north and south of the step-over. (b) Photograph looking south along W-facing scarp in the foreground and E-facing scarp farther south. Pond area in between is denoted by whitish silts and clays.

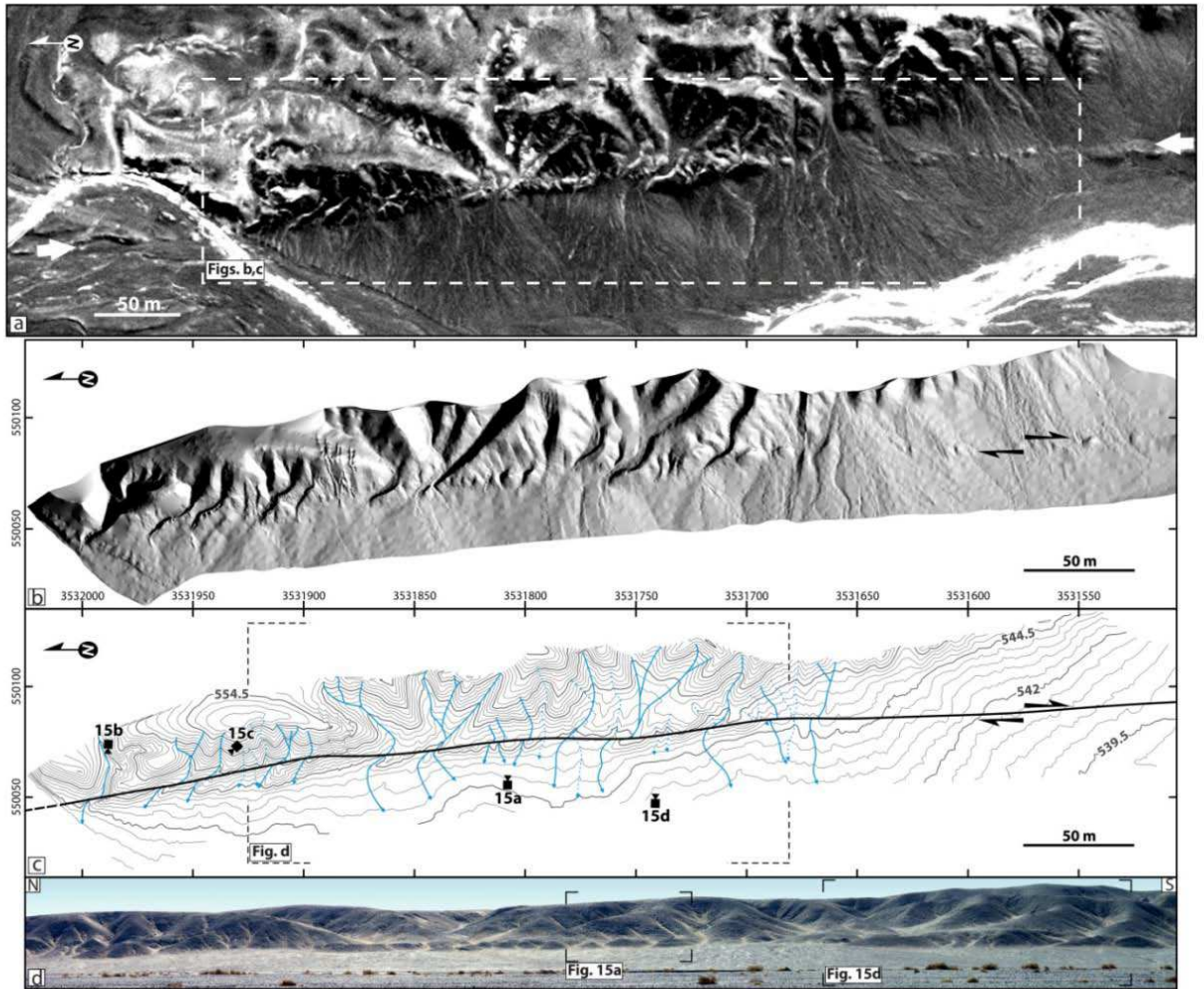


**Figure 14.** Fault trace north of the trench site (see Figure 12b for location). (a) Raw Quickbird imagery showing fault scarp (white arrows) across the late Pliocene-Pleistocene (central part) and late Pleistocene-Holocene (northern and southern parts) deposits. Rectangle denotes the outline of (b) and (c). (b) High-resolution shaded relief map from a DGPS survey, illuminated under a SSW-oriented 40°-inclined sun. (c) Corresponding topographic map. Contour interval is 50 cm (survey data not tied to absolute elevation). The longest gullies (thick blue lines) display right-lateral offset ranging from several meters to more than 10 meters. The smallest gullies (dashed blue lines) cross the fault without detectable offset. Dashed corners correspond to the outline of (d). Locations of photographs in Figure 15 are indicated. (d) Photograph toward east. Panoramic view of the fault trace along the western

flank of smoothed hills made of late Pliocene-Pleistocene deposits. Intermittent gullies are partly filled by aeolian sediments (whitish sands and silts). Black corners denote the outlines of Figures 15a and 15d.

Accepted Article

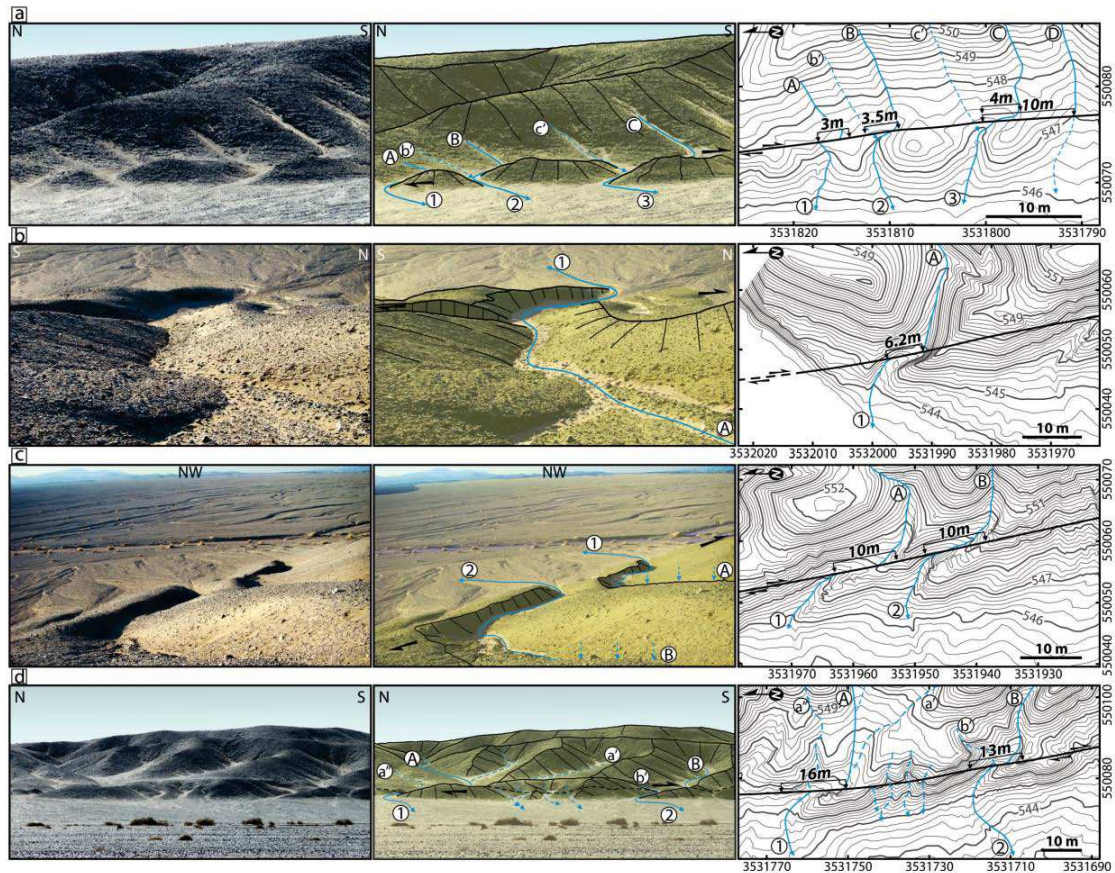


**Figure 15.** Recent right-lateral offsets north of the trench site. Field photographs (left panels), interpretative sketches (central panels) and corresponding topographic maps (right panels). See Figures 14c and 14d for locations. Contour interval is 20 cm (survey data not tied to absolute elevation). Lettered (A, B, C) gullies up-fault drain through outlets (1, 2, 3) down-fault highlighting recent offsets. Small regressive gullies (a', b', c') show no recent offset.

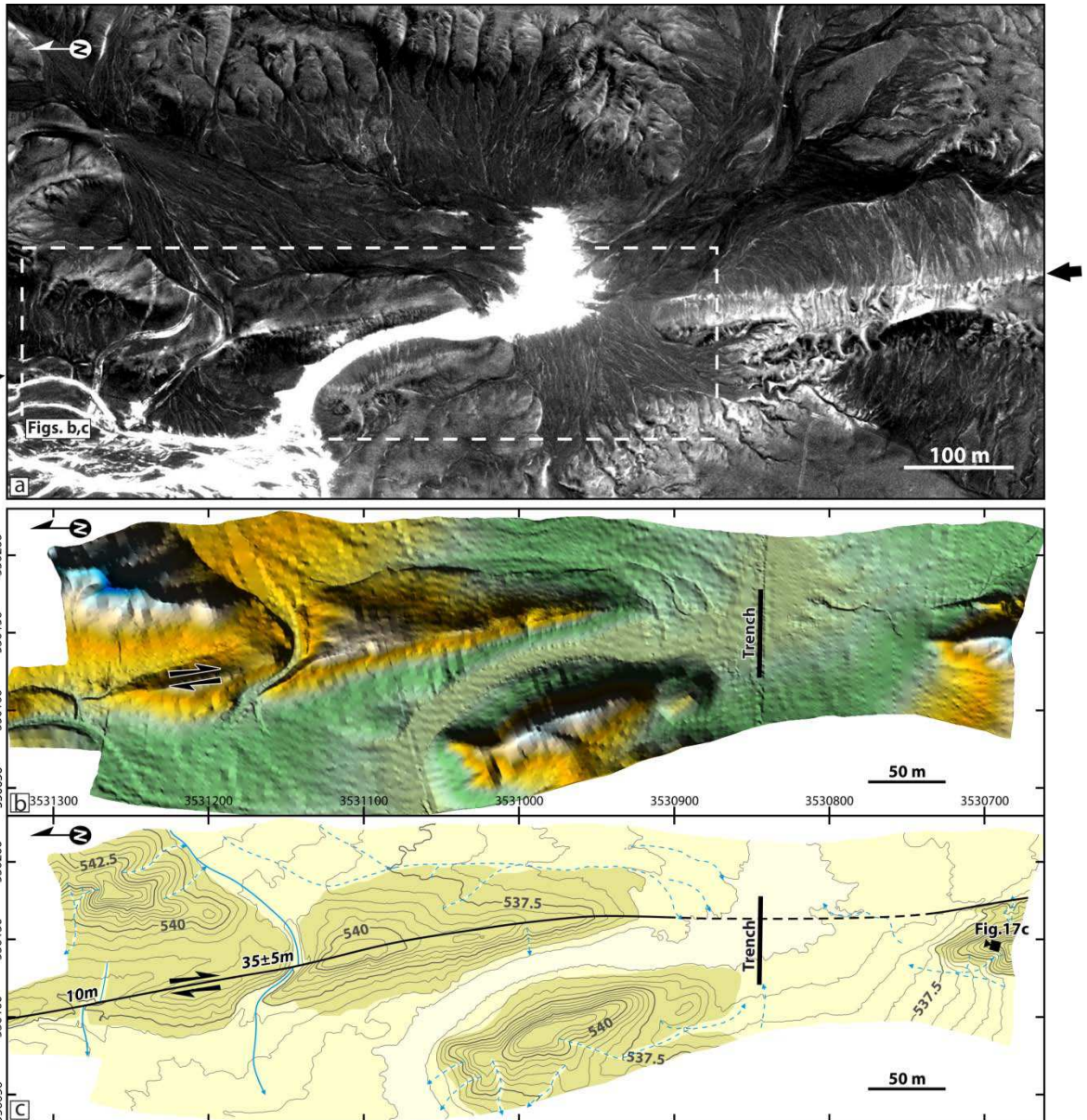


**Figure 16.** (a) Raw Quickbird satellite image showing the fault trace (black arrows) south of the trench site (see Figure 12b for location). Fault cuts across late Pliocene-Pleistocene (northern and southern parts) and late Pleistocene-Holocene (central part) deposits. White pixels in the center of image indicate a local pond draining westwards. Rectangle denotes the outline of (b) and (c). (b) High-resolution colored shaded relief map extracted from the DGPS survey of the trench site. (c) Corresponding topographic map. Contour interval is 50 cm (survey data not tied to absolute elevation). Geology adapted from field observations and geological map [Alavi-Naini and Griffis, 1981b]. Fault scarp is clear on both sides of the

local pond and not discernable within the pond. Fault trace is extrapolated towards the main fault strand in the trench (see Figure 18). Two gullies (thick blue lines) 300 and 400 m north of the trench display right-lateral offsets on the order of  $35 \pm 5$  and 16 m, respectively.

Dashed blue lines denote small tributaries and regressive gullies.

Accepted Article

Accepted

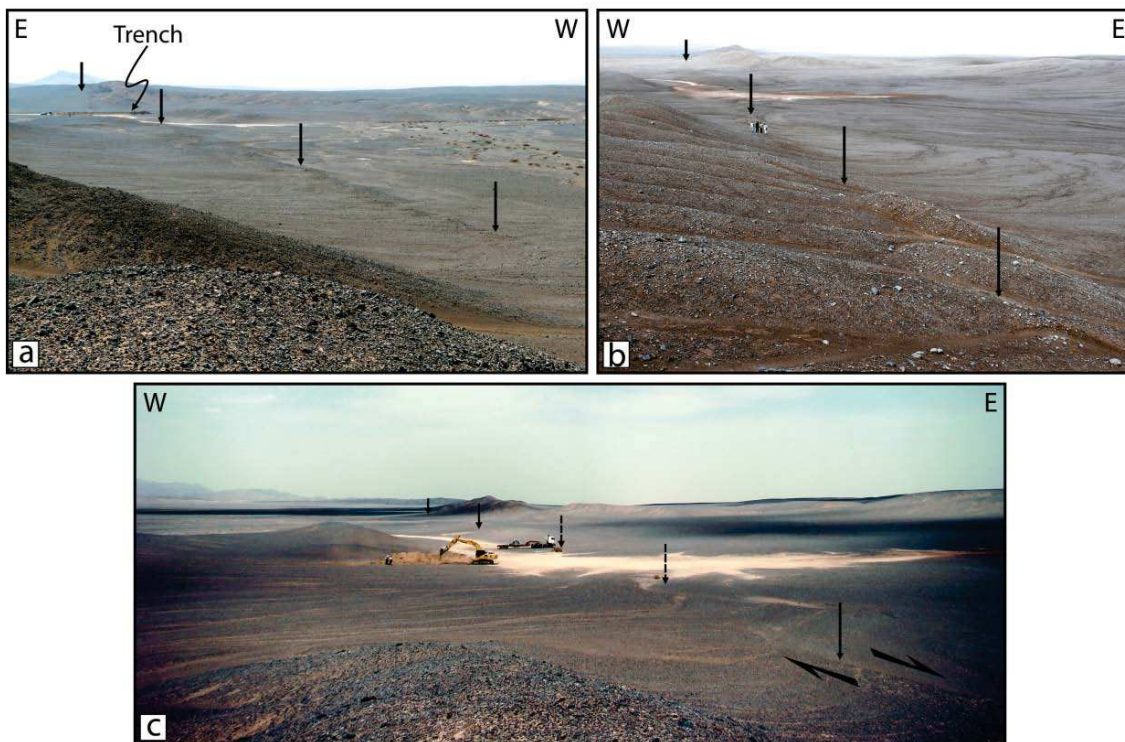


**Figure 17.** Field photographs of the fault showing clear scarps north (a) and south (b) of the pond and no discernable scarp (c) within the pond.

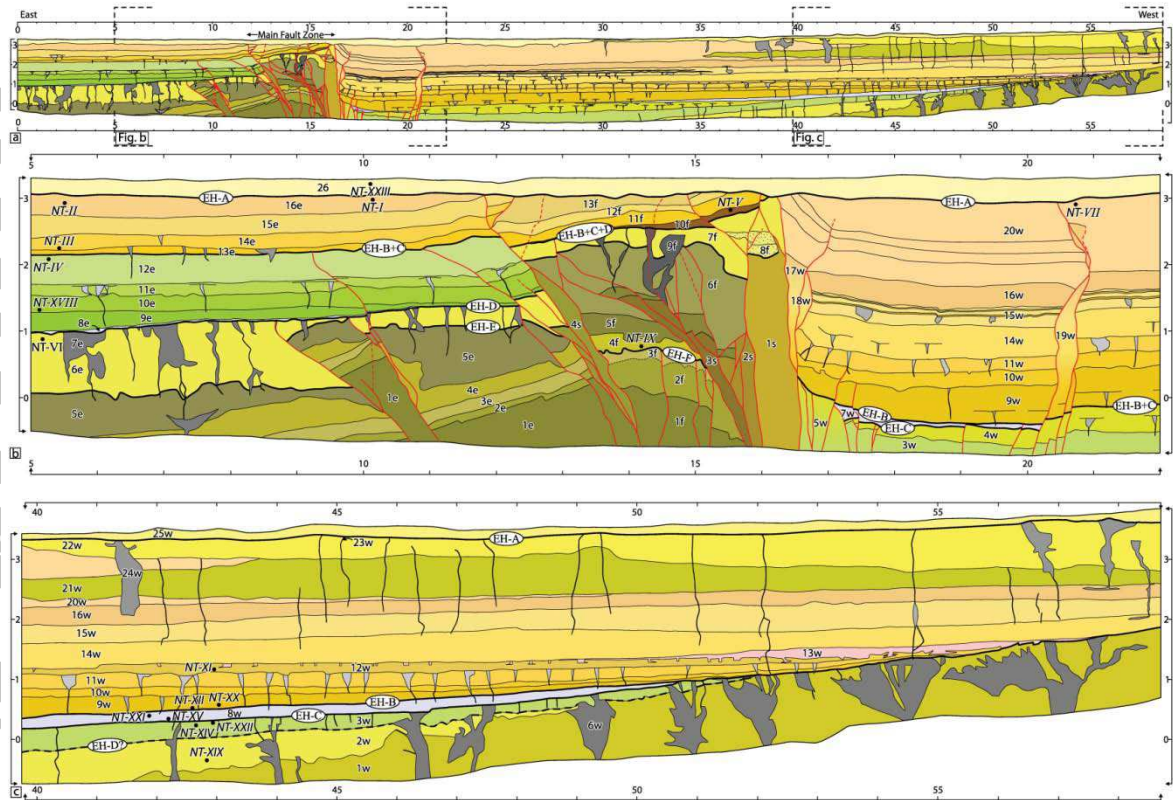


**Figure 18.** Log of the southern wall of the trench excavated across the Nayband fault ( $31^{\circ} 54.74'N$ ,  $57^{\circ} 31.84'E$ , 535m above sea level). (a) Faults and fractures are shown with red and dashed red lines, respectively. Three distinctive sections are distinguished; the western, the main fault zone (MFZ) and the eastern sections. (b) and (c) Highlight details of the cross-cutting and depositional relationships in the eastern and western portions of the trench, respectively. See Table 5 for a detailed description of the units in each section. White labeled ellipses point to six distinctive event horizons (EH-A to EH-F, see text for discussion). Labeled black dots locate the OSL samples (see Table 4 for corresponding ages).

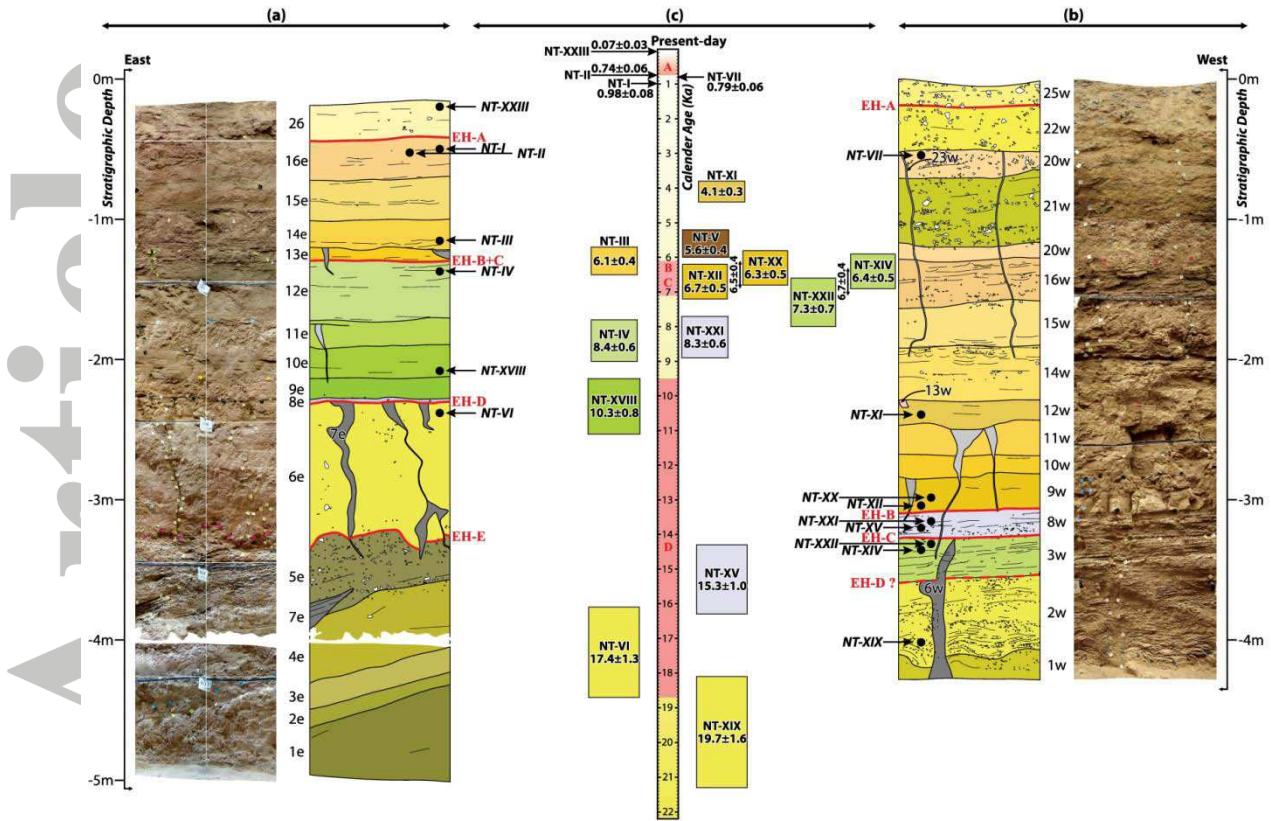


**Figure 19.** Photo mosaics and corresponding stratigraphic logs of the sediments exposed in the trench excavation, with vertical positions of dated OSL samples (see exact locations in Figures 18b and 18c) and event horizons of five past earthquakes (see section 4.4). (a) Section east of the MFZ, near meters 8 (top 4 m) and 12 (bottom 1 m). (b) Section west of the MFZ, between meters 42-43. (c) Corresponding OSL ages (colored boxes) are given in thousands of years before present (ka B.P.). Pink colored intervals denote the maximum time windows for the last four paleoearthquakes (see section 4.4). Two vertical arrows denote weighted mean ages of the samples collected from units 3w and 9w. Note the ages of samples NT-XV and NT-XXI, which are older than the immediate below samples (NT-XIV and NT-XXII).

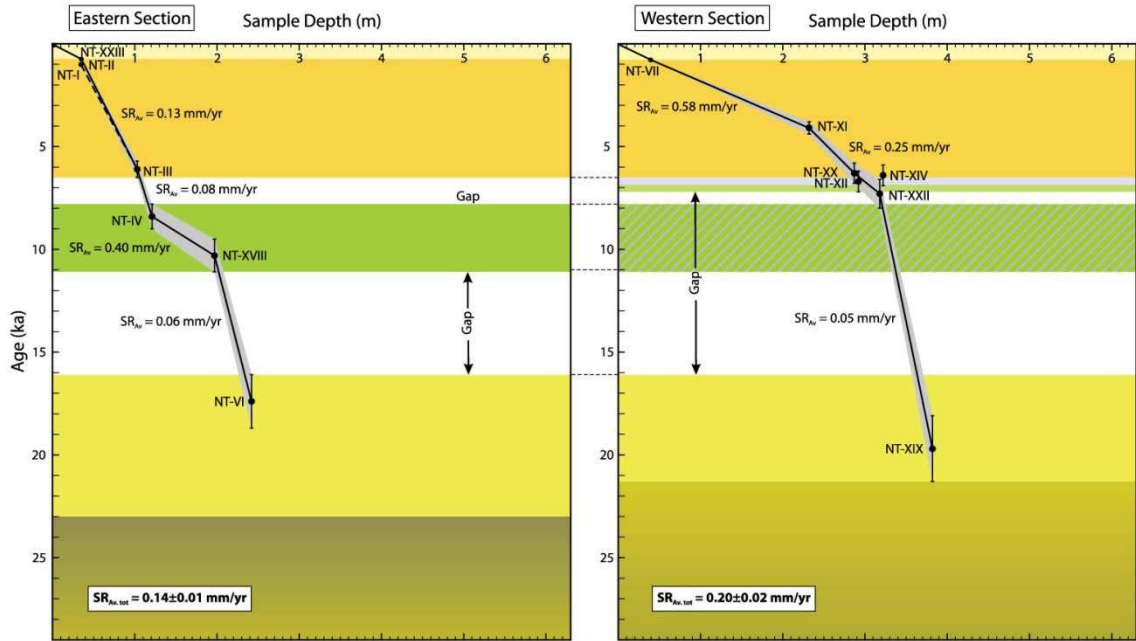


**Figure 20.** Sedimentation rates calculated for the eastern and western stratigraphic logs.

Colors are as for units displayed on Figures 18 and 19 and figure out the duration of the preserved units (hatched where extrapolated). Note the pile of sediments younger than 7 ka is much thicker in the western section than in the eastern one. Very low ( $<0.1 \text{ mm yr}^{-1}$ ) sedimentation rates characterize sediment gaps. The single gap evidenced in the western section splits into two gaps flanking units 9e to 12e (green color) in the eastern section.

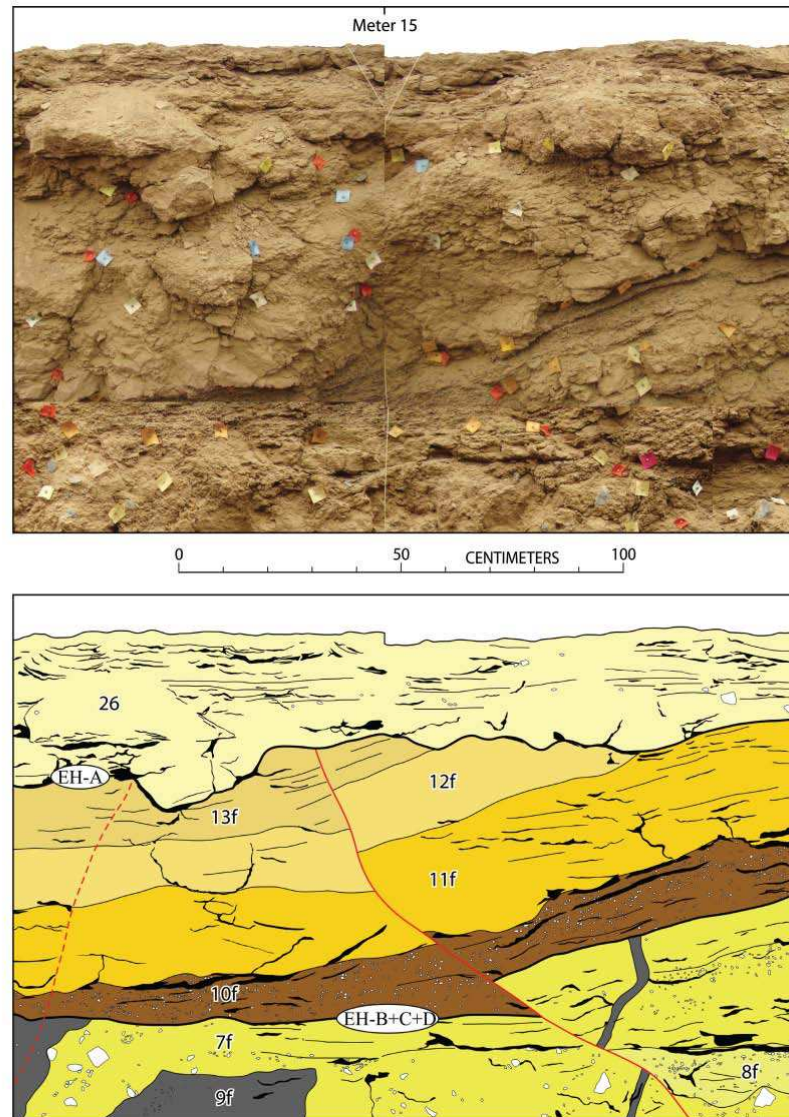


**Figure 21.** Evidence for the most recent earthquake (event A). Photomosaic (top) and interpretation (bottom) showing a west-dipping fault strand near meter 15 offsetting units 7f and 10f to 13f as well as the older event horizon (EH-B+C+D), which abruptly terminates upward, at the base of the most recent undisturbed deposits (unit 26).

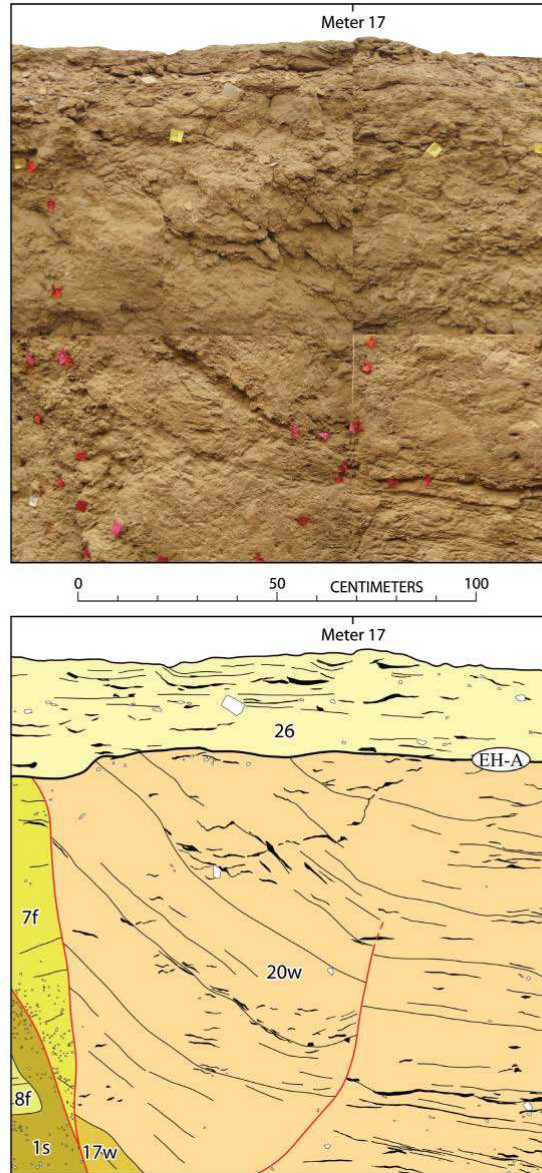


**Figure 22.** Photomosaic (top) and interpretive sketch (bottom) close to the western limit of the MFZ. The young fine-grained sediments of units 20w are dragged up against a prominent steep fault near meter 16.5 and unconformably overlain by the flat-lying unit 26. An east-dipping secondary fault displaces the lower part of unit 20w along the hinge of folded strata and gradually terminates upward as folding is less effective away from the prominent fault strand.

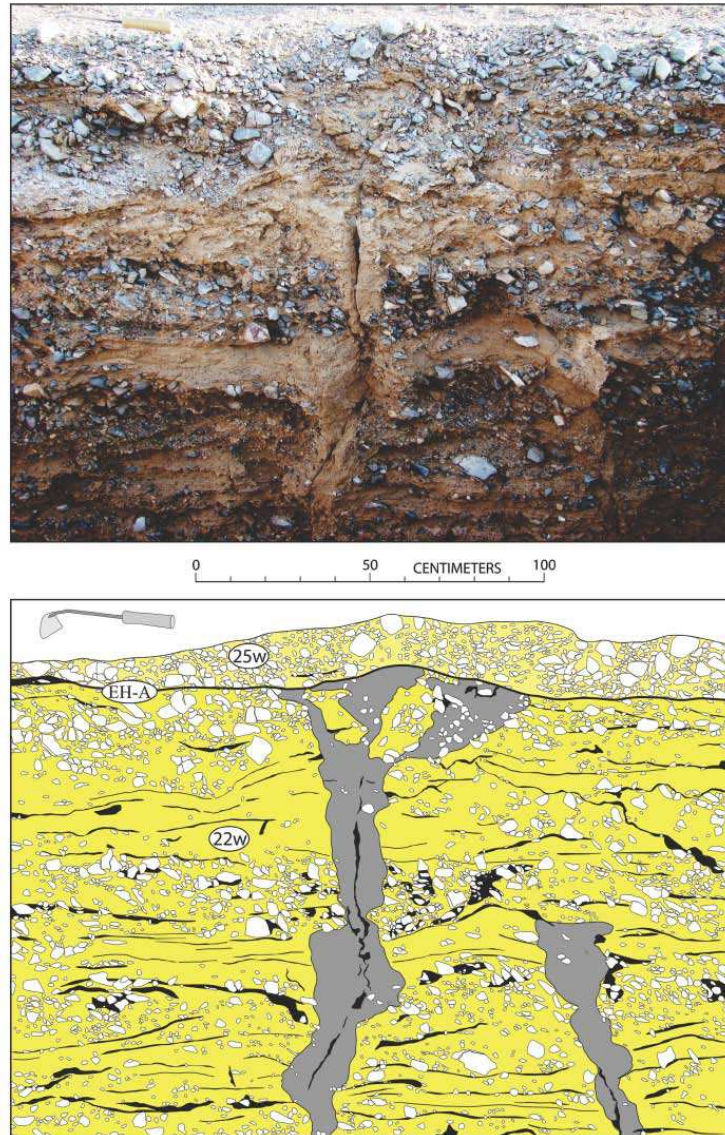


**Figure 23.** Oblique photograph (top) and interpretive sketch (bottom) of two sandy dikes formed during event A, at the western end of the trench. These steep sandy dikes are made of loose sandy material with scarce pebbles from the host layers (unit 22w) and cut through the flat-lying, coarse-grained strata with fine-grained inter-beds of unit 22w. The cone-shaped larger dike is covered by gravelly deposits (unit 25w) while the smaller one abutting against a coarse-grain layer of the host unit did not reach the ground surface at the time of the most recent earthquake (EH-A).

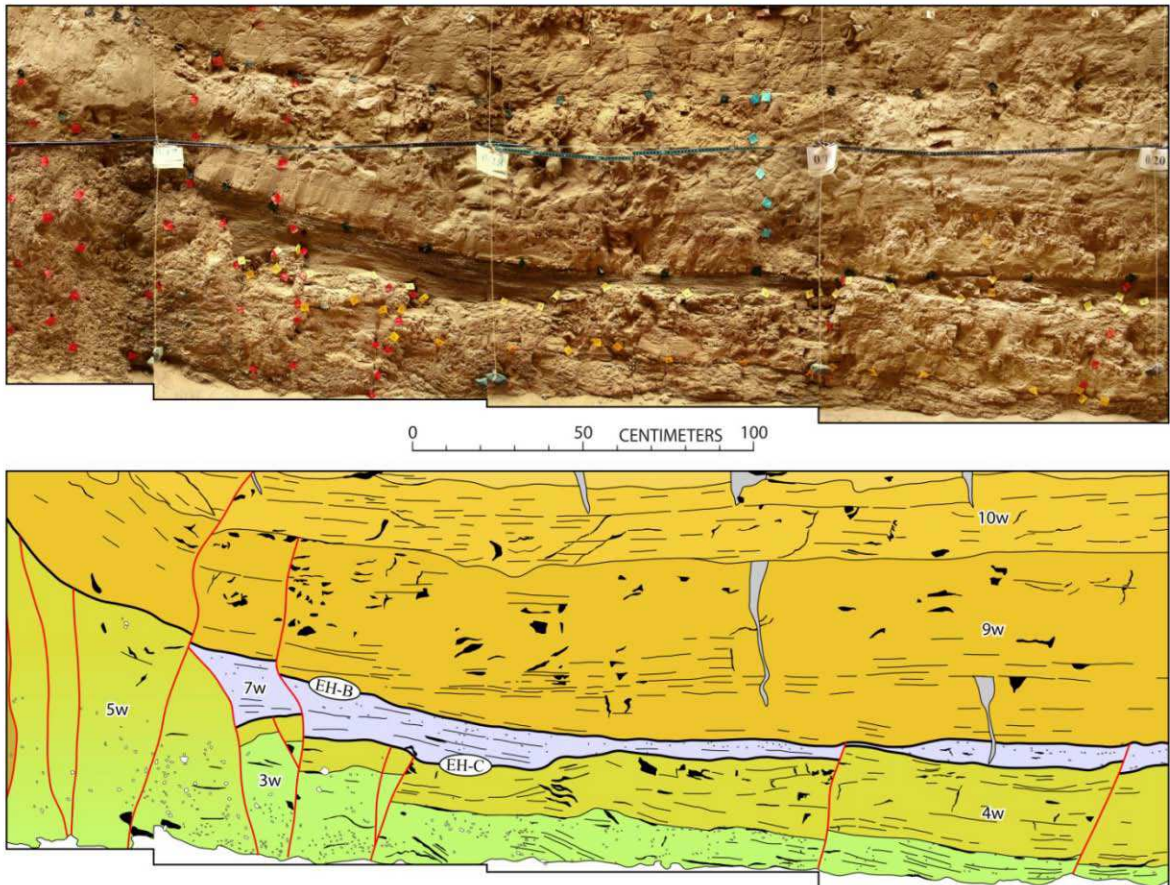


**Figure 24.** Evidence for penultimate earthquake (event B). Photomosaic (top) and interpretive sketch (bottom), between meters 16.5 and 20, showing several steep fault strands cutting through the lower units (units 3w, 4w, 5w, and 7w) and abruptly terminating upward at the base of unit 9w; the eastern tip of unit 7w, near meter 17, is seen faulted and the corresponding displacement is not transfer upward. The event horizon of the penultimate earthquake (EH-B) is displaced by two fault strands, close to meter 17, during a younger earthquake (event A). Two small fault strands and a tiny fracture, between meters 17 and 18, capped by a thin layer of sandy-gravelly material (unit 7w), testify for the event horizon of an older earthquake (event C).

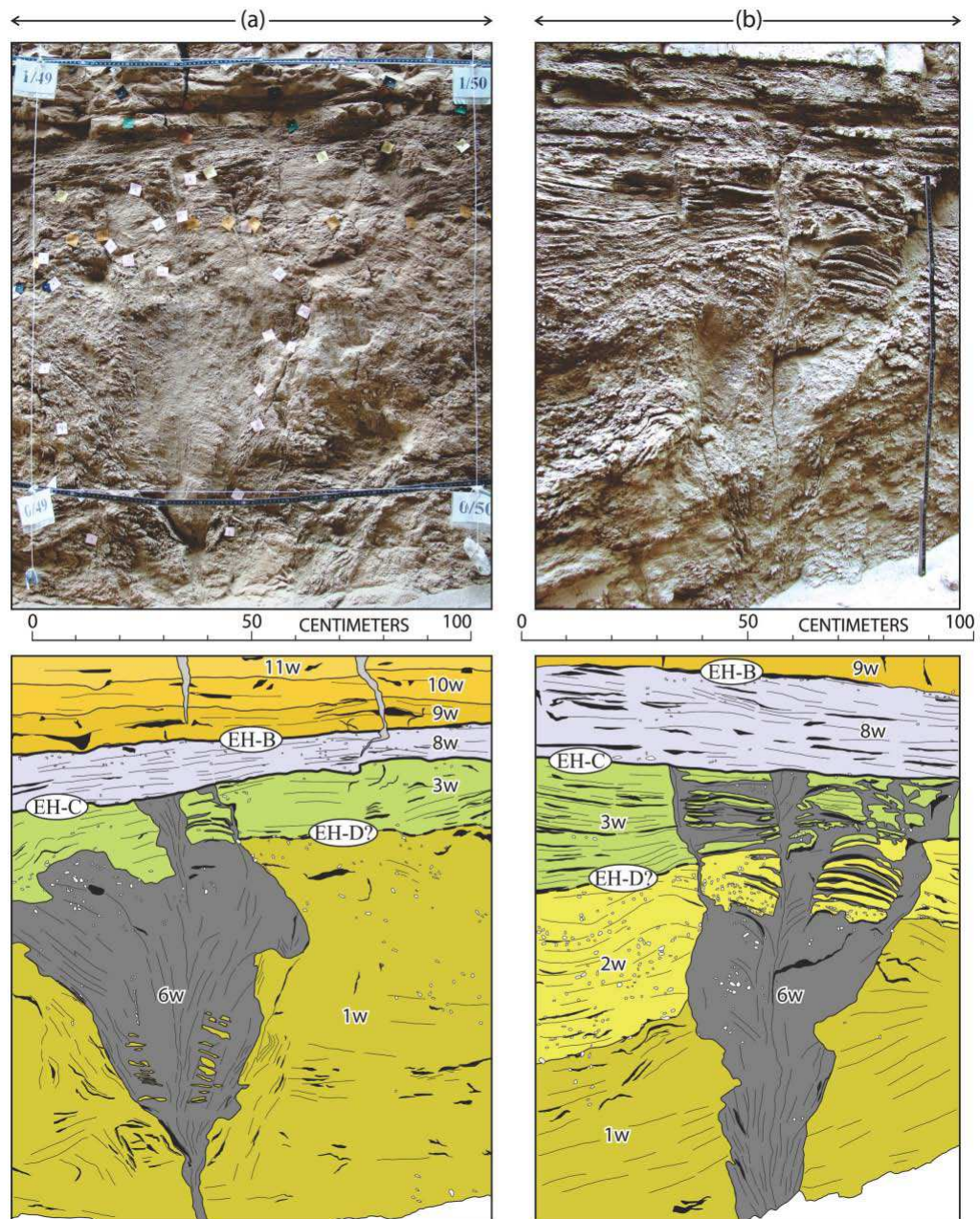


**Figure 25.** Liquefaction features on the southern (left) and the northern (right) walls of the western section of the trench giving evidence for event C. (Left) Photomosaic and interpretive sketch of a sand blow (unit 6w) between meters 49 and 50. The sandy material coming from older layer(s) than 1w, and the intruded materials are overlain by an undisturbed alluvial layer (unit 8w). Some remnants of the host sediments (units 1w and 3w) remain away from the central pillar. (Right) Oblique photograph and interpretive sketch of another sand

blow (unit 6w) between meters 47 and 48. The base of unit 9w corresponds to a lateral equivalent of the event horizon of the penultimate earthquake (EH-B).

Accepted Article

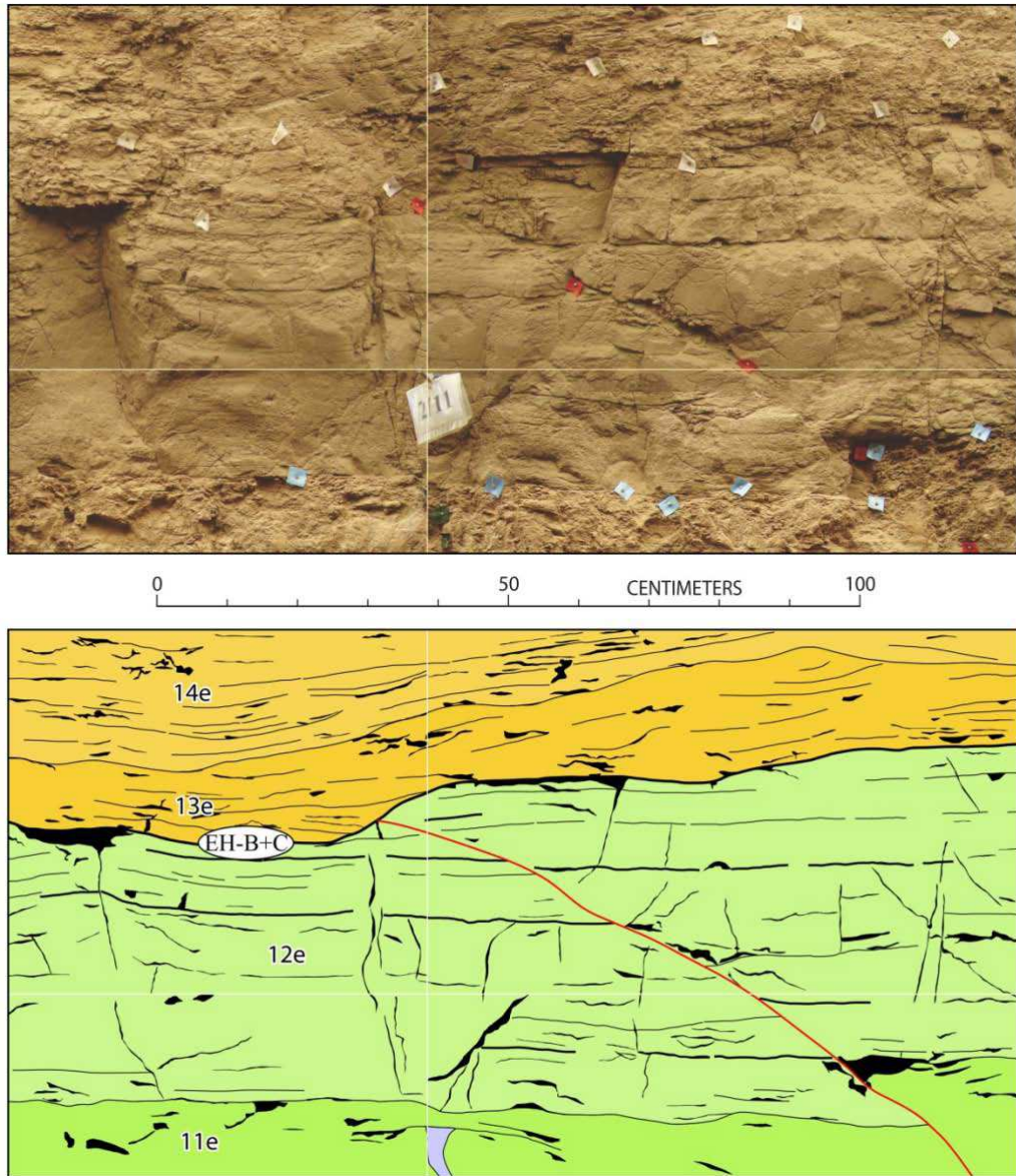


**Figure 26.** Evidence for the penultimate and antepenultimate earthquakes (events B+C), east of the main fault zone around meter 11. A west-dipping fault strand displaces the well-bedded, fine-grained pond sediments (units 11e and 12e) and forms a 10-15-cm high E-facing buried scarplet. Note the similar vertical displacements (15 cm) across the strata from the base of unit 12e up to the event horizon (EH-B+C). Both the fault and the scarplet are overlain by unit 13e. The base of unit 13e also corresponds to a lateral equivalent of EH-C.

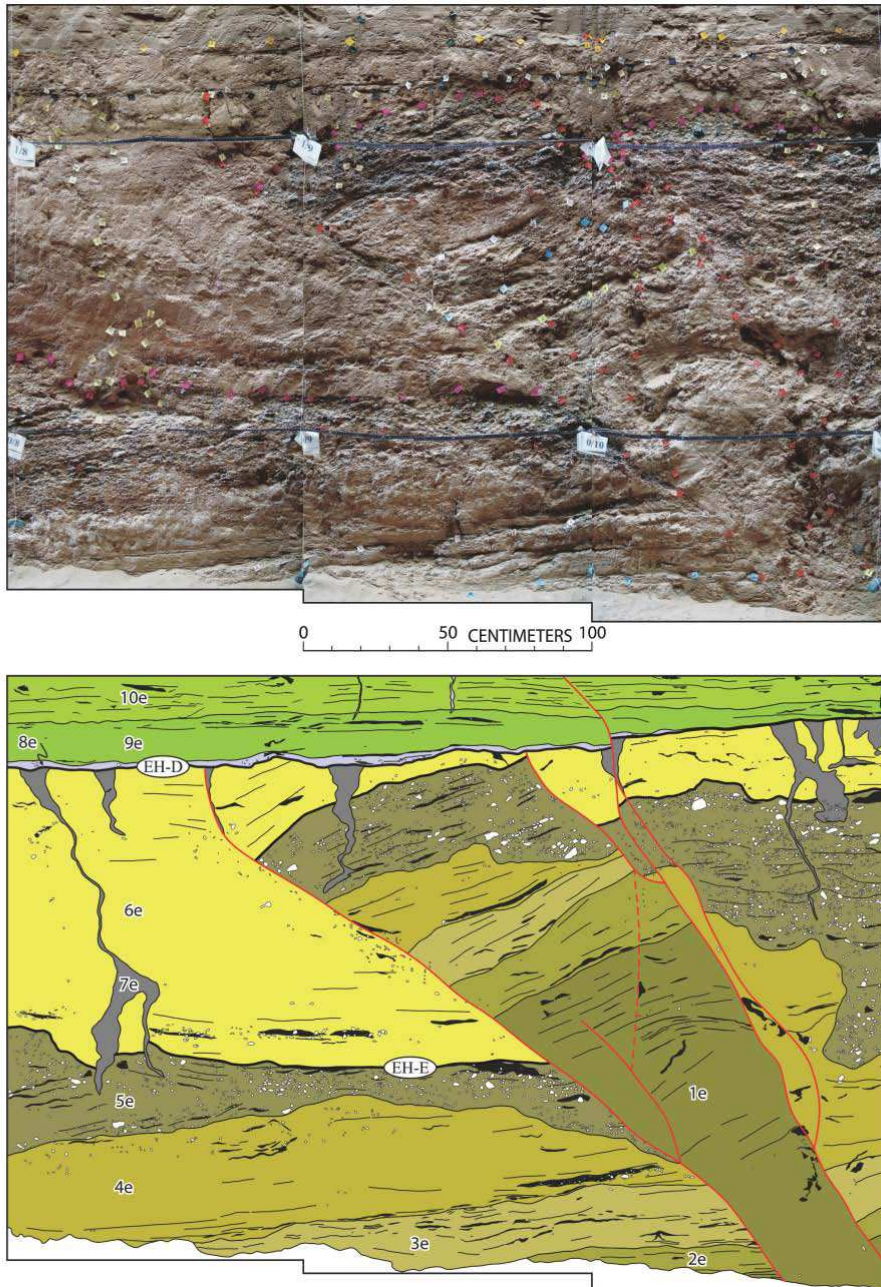


**Figure 27.** Evidence for the fourth paleoearthquake (event D), eastern section of the trench exposure deposits between meters 8 and 11. Photomosaic (top) and interpretive sketch (bottom) showing two west-dipping faults displacing units 1e to 6e, abruptly terminating at the same stratigraphic level, and overlain by a thin layer of sandy-gravelly material (unit 8e). All the layers between these two faults are tilted 25° eastward and unconformably sealed by flat-lying units 8e to 10e. Several liquefied sandy features (unit 7e), likely originated from unit 5e, are injected upward into the fine-grained pond sediments (unit 6e) and covered by the

same stratigraphic level as the fault terminations, at the base of unit 8e (EH-D). Note also the small displacements of EH-D, unit 8e, and subsequent layers by a fault splay reactivated during a younger event (Event B).

Accepted Article

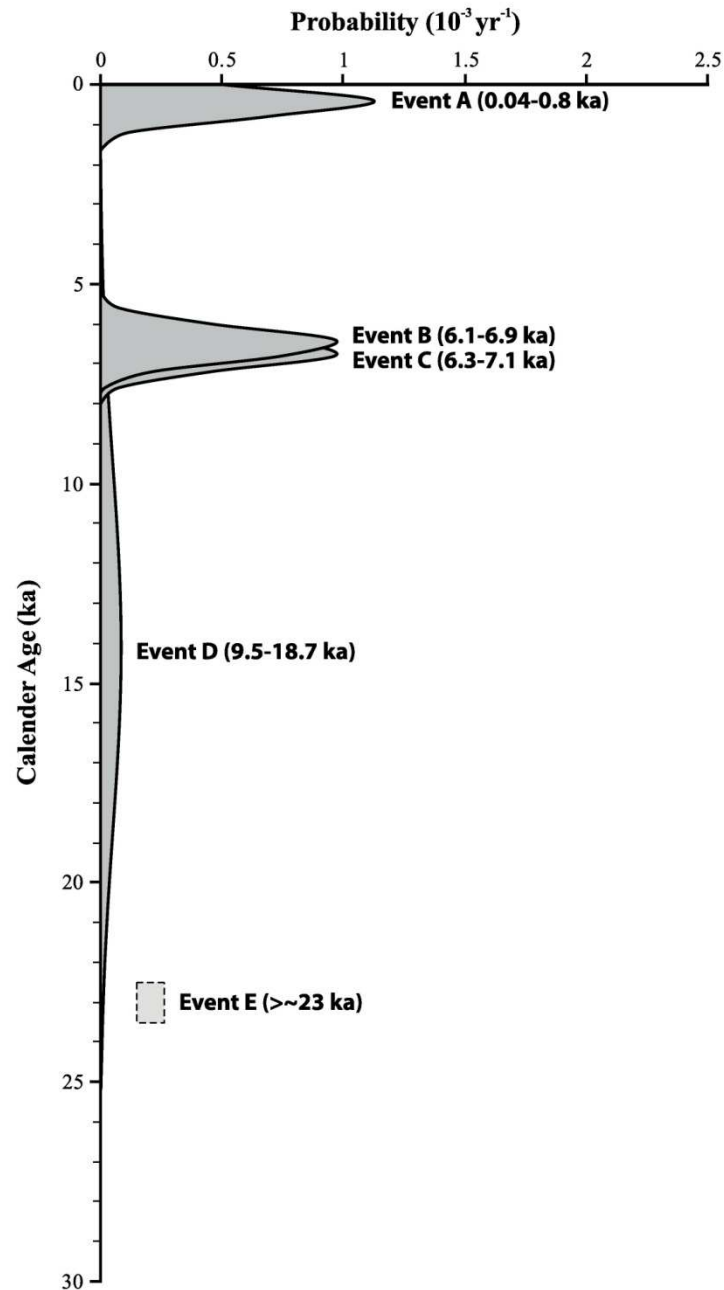


**Figure 28.** Probability density functions of four past earthquakes identified along the Nayband fault. Each of the peaks corresponds to a large earthquake and represent the error in the age assessment of each event. Dashed-lines and light gray box represent the possible time window for an older earthquake (event E, see section 4.4).

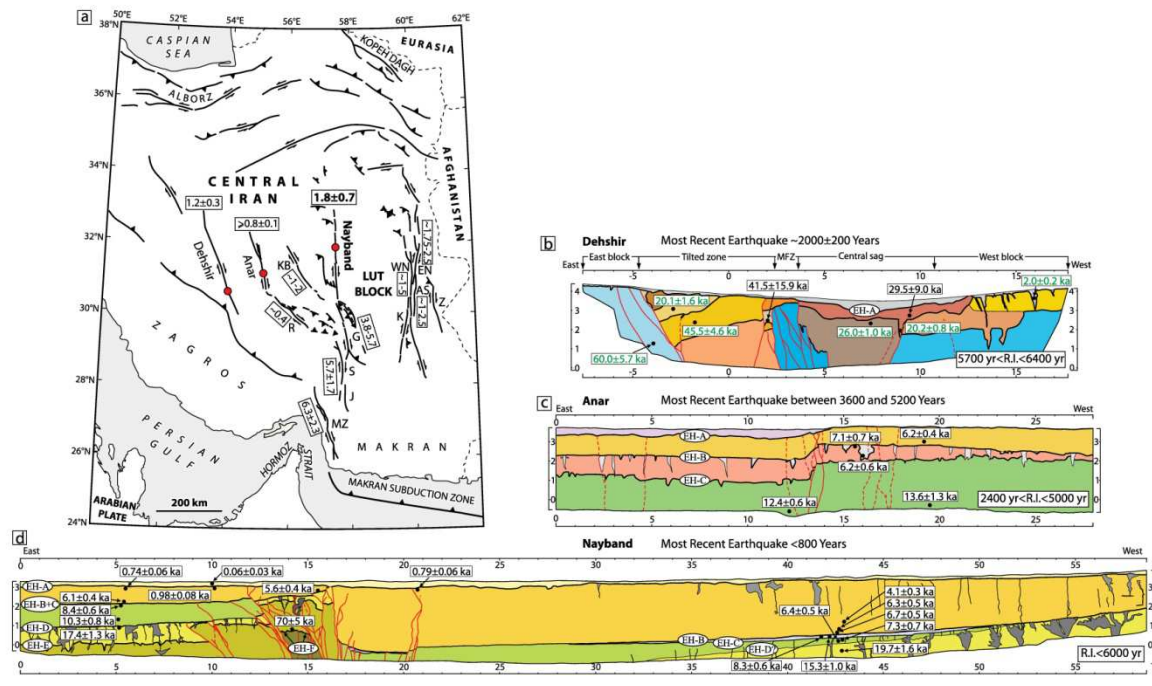


**Figure 29.** Summary of late Quaternary slip rates and paleoseismic data presently available across Central Iran. (a) Map of the major active faults in Central and Eastern Iran. AS, Assaghi fault; EN, East Neh fault; G, Gowk fault; J, Jiroft fault; K, Kahourak fault; KB, Kuh Banan fault; MZ, Minab-Zendan fault system; R, Rafsanjan fault; S, Sabzevaran fault; WN, West Neh fault; and Z, Zahedan fault. Numbers in boxes refer to right-slip rates averaged over the last 270 ka for the Dehshir fault [Le Dortz *et al.*, 2011], ~120 ka for the Rafsanjan fault [Fattahi *et al.*, 2011], ~120 ka for the Minab-Zandan fault system [Regard *et al.*, 2005], 100 ka for the Nayband fault [this study], ~42 ka for the Sabzevaran and Jiroft fault system [Regard *et al.*, 2005], 10 ka for the Anar fault [Le Dortz *et al.*, 2009; Foroutan *et al.*, 2012], ~8 ka for the Gowk [Walker *et al.*, 2010b; Fattahi *et al.*, 2014], and estimated over the Holocene for the Kuh Banan [Allen *et al.*, 2011; Walker and Allen, 2012], West Neh, East Neh, and Assaghi [Meyer and Le Dortz, 2007] faults. Red circles locate paleoseismic sites along the Dehshir (b, modified from Nazari *et al.* [2009] with refined OSL ages indicated in green, see Table 3 of Le Dortz *et al.* [2011] for the OSL age parameters), Anar

(c, *Foroutan et al.* [2012]), and Nayband faults (d, [this study]). Age of the most recent earthquake as well as the average recurrence interval of large earthquakes is indicated for each fault.

**Table 1.** Source parameters of the well-constrained fault-plane solutions of instrumental earthquakes in east-Central Iran. The fault-plane solutions are shown on Figure 1b.

Event	Region	Lat. (°N)	Long. (°E)	Strike	Dip	Rake	Depth (km)	M <sub>w</sub>	Fault	Source
1978 Sept. 16	Tabas	33.25	57.38	355	16	155	9	7.28	Tabas	<i>Walker et al. [2003]</i> *
1979 Feb. 13	Tabas	33.31	57.40	327	28	116	11	5.58	Tabas	<i>Walker et al. [2003]</i> *
1980 Jan. 12	Tabas	33.55	57.23	348	20	137	14	6.0	Tabas	<i>Walker et al. [2003]</i> *
1981 Jun. 11	Golbaf	29.86	57.68	169	52	156	20	6.58	Gowk	<i>Berberian et al. [2001]</i> *
1981 Jul. 28	Sirch	29.99	57.79	177	69	184	18	6.98	Gowk	<i>Berberian et al. [2001]</i> *
1984 Aug. 6	Hur	30.80	57.17	279	35	86	11	5.3	—	<i>Baker [1993]</i>
1989 Nov. 20	South Golbaf	29.90	57.72	145	69	188	10	5.83	Gowk	<i>Berberian et al. [2001]</i> *
1990 Mar. 25	Tabas	33.34	56.99	223	90	-180	15	5.1	Tabas	Harvard CMT
1998 Mar. 14	Fandoqa	30.08	57.58	156	54	195	5	6.57	Gowk	<i>Berberian et al. [2001]</i> *
1998 Nov. 18	Chahar Farsakh	30.32	57.53	174	55	173	15	5.34	Gowk	<i>Berberian et al. [2001]</i> *
2005 Feb. 22	Dahuieh (Zarand)	30.77	56.73	270	60	104	7	6.4	Kuh Banan	<i>Talebian et al. [2006]</i> *

\* Epicenters from *Engdahl et al. [1998]* or subsequent updates to their catalog.

**Table 2.** Concentrations of *in-situ* produced  $^{36}\text{Cl}$  and corresponding CRE ages. The chemical extraction of chlorine by precipitation of silver chloride has been adapted from the protocol of *Stone et al.* [1996]. The samples were picked with a known quantity of stable chlorine carrier [e.g., *Desilets et al.*, 2006] to simultaneously determine  $^{36}\text{Cl}$  and chlorine concentrations by isotope dilution accelerator mass spectrometry (AMS). The chemical treatment of the samples and the measurements were performed at the CEREGE laboratory (Aix-en-Provence, France), using KNSTD1600 standard. The Excel spreadsheet provided by *Schimmelpfennig et al.* [2009] was used to calculate all  $^{36}\text{Cl}$  ages with a  $^{36}\text{Cl}$  spallation production rate of  $42 \pm 0.2 \text{ at.}^{36}\text{Cl} (\text{g Ca})^{-1} \cdot \text{a}^{-1}$  [*Braucher et al.*, 2011] similar to the one of *Schimmelpfennig et al.* [2011]. A  $^{36}\text{Cl}$  half-life of 301 ka [*Gosse and Phillips*, 2001], a density of  $2 \text{ g cm}^{-3}$ , and a neutron attenuation length of  $160 \text{ g.cm}^{-2}$  [*Gosse and Phillips*, 2001] are used.

Sample	Sample description	Latitude (°N)	Longitude (°E)	Elevation (m)	Cl (ppm)	Measured $^{36}\text{Cl}$ ( $10^6 \text{ at/g rock}$ )	$^{36}\text{Cl}$ CRE age (ka) no erosion
Site South							
<i>Eastern Fan</i>							
N09S1	Cobble (10 cm)	31.98406	57.52886	654	29	$2.28 \pm 0.05$	$87.05 \pm 7.53$
N09S2	Cobble (10 cm)	31.98407	57.52885	657	26	$2.28 \pm 0.05$	$89.65 \pm 7.97$
N09S3	Cobble (10 cm)	31.98405	57.52883	658	77	$1.72 \pm 0.05$	$58.44 \pm 4.88$
N09S4	Cobble (5 cm)	31.98406	57.5289	657	40	$2.42 \pm 0.07$	$91.71 \pm 8.06$
N09S5	Fragment of a cobble (25 cm)	31.98406	57.52882	657	36	$1.73 \pm 0.07$	$63.49 \pm 5.70$
N09S6	Cobble (10 cm)	31.98409	57.52887	658	29	$2.29 \pm 0.05$	$88.11 \pm 7.58$
<i>Western Fan</i>							
N09S7	Cobble (10 cm)	31.98592	57.52728	645	21	$1.73 \pm 0.05$	$66.52 \pm 5.77$
N09S8	Cobble (10 cm)	31.98585	57.52728	644	29	$0.66 \pm 0.02$	$23.78 \pm 2.02$
N09S9	Cobble (10 cm)	31.98564	57.52729	644	30	$0.87 \pm 0.03$	$31.49 \pm 2.65$
N09S10	Fragment of a boulder	31.98586	57.5272	645	27	$1.07 \pm 0.04$	$38.88 \pm 3.38$
N09S11	Cobble (10 cm)	31.98615	57.52719	645	31	$3.01 \pm 0.06$	$121.11 \pm 10.77$
N09S12	Cobble (5 cm)	31.98614	57.52714	645	45	$0.66 \pm 0.02$	$22.55 \pm 1.82$
Site North							
<i>Northern Fan</i>							
N09S13	Cobble (5 cm)	32.04174	57.52525	652	48	$2.15 \pm 0.07$	$79.81 \pm 6.94$
N09S14	Cobble (10 cm)	32.04186	57.52517	652	19	$0.45 \pm 0.02$	$15.91 \pm 1.36$

N09S15	Cobble (10 cm)	32.04191	57.5251	650	15	1.10 ± 0.04	41.57 ± 3.67
N09S16	Cobble (10 cm)	32.04171	57.52504	650	45	0.73 ± 0.02	26.27 ± 2.09
N09S17	Cobble (10 cm)	32.04222	57.52492	652	17	0.84 ± 0.02	30.74 ± 2.55
N09S18	Cobble (10 cm)	32.04238	57.5249	653	37	1.99 ± 0.07	74.72 ± 6.75
<i>Southern Fan</i>							
N09S19	Cobble (10 cm)	32.03525	57.52539	640	28	0.65 ± 0.02	23.75 ± 2.04
N09S20	Cobble (10 cm)	32.03531	57.52539	640	29	2.32 ± 0.07	93.05 ± 8.35
N09S21	Cobble (5 cm)	32.03533	57.52537	640	25	0.87 ± 0.02	33.14 ± 2.70
N09S22	Cobble (10 cm)	32.03537	57.52535	640	27	0.75 ± 0.03	27.75 ± 2.37
N09S23	Cobble (10 cm)	32.03539	57.52535	640	34	4.88 ± 0.12	221.45 ± 22.56
N09S24	Cobble (10 cm)	32.03548	57.52536	641	29	4.06 ± 0.09	177.03 ± 16.96

---

Accepted Article

**Table 3.** Chemical composition of the samples collected for  $^{36}\text{Cl}$  dating. Measurements of the major elements were undertaken by ICP-OES technique at the CNRS SRM facility (CRPG Nancy). The radiogenic  $^{36}\text{Cl}$  contribution has been obtained by measuring the concentrations of U and Th in the target mineral [Zreda *et al.*, 1991; Stone *et al.*, 1996, 1998; Gosse and Phillips, 2001].

Sample	H <sub>2</sub> O (%)	Al <sub>2</sub> O <sub>3</sub> (%)	CaO (%)	Fe <sub>2</sub> O <sub>3</sub> (%)	K <sub>2</sub> O (%)	MgO (%)	MnO (%)	Na <sub>2</sub> O (%)	P <sub>2</sub> O <sub>5</sub> (%)	SiO <sub>2</sub> (%)	TiO <sub>2</sub> (%)	Th (%)	U (%)
Site South													
<i>Eastern Fan</i>													
N09S1	0.32	0.14	54.45	0.16	0.01	0.49	0.01	0	0	0.49	0.00	0.14	1.67
N09S2	0.32	0.10	54.76	0.07	0.00	0.45	0.01	0	0	0.00	0.00	0.07	2.30
N09S3	0.32	0.14	54.45	0.16	0.01	0.49	0.01	0	0	0.49	0.00	0.14	1.67
N09S4	0.32	0.17	54.13	0.26	0.03	0.53	0.01	0	0	0.98	0.01	0.21	1.04
N09S5	0.32	0.14	54.45	0.16	0.01	0.49	0.01	0	0	0.49	0.00	0.14	1.67
N09S6	0.32	0.14	54.45	0.16	0.01	0.49	0.01	0	0	0.49	0.00	0.14	1.67
<i>Western Fan</i>													
N09S7	0.31	0.10	54.40	0.11	0.00	0.50	0.01	0	0	0.43	0.00	0.09	5.36
N09S8	0.27	0.09	54.48	0.06	0.00	0.34	0.01	0	0	0.86	0.00	0.05	1.25
N09S9	0.31	0.10	54.40	0.11	0.00	0.50	0.01	0	0	0.43	0.00	0.09	5.36
N09S10	0.31	0.10	54.40	0.11	0.00	0.50	0.01	0	0	0.43	0.00	0.09	5.36
N09S11	0.34	0.12	54.32	0.16	0.00	0.65	0.01	0	0	0.00	0.01	0.12	9.47
N09S12	0.31	0.10	54.40	0.11	0.00	0.50	0.01	0	0	0.43	0.00	0.09	5.36
Site North													
<i>Northern Fan</i>													
N09S13	0.29	0.12	53.96	0.08	0.02	0.99	0.01	0	0	0	0.00	0.10	3.06
N09S14	0.25	0.06	54.89	0.04	0.00	0.46	0.00	0	0	0	0.00	0.04	4.39
N09S15	0.29	0.12	53.96	0.08	0.02	0.99	0.01	0	0	0	0.00	0.10	3.06
N09S16	0.32	0.18	53.04	0.12	0.03	1.53	0.01	0	0	0	0.01	0.16	1.74
N09S17	0.29	0.12	53.96	0.08	0.02	0.99	0.01	0	0	0	0.00	0.10	3.06
N09S18	0.29	0.12	53.96	0.08	0.02	0.99	0.01	0	0	0	0.00	0.10	3.06
<i>Southern Fan</i>													
N09S19	0.38	0.12	53.63	0.05	0.01	1.09	0.01	0	0	0	0.00	0.09	1.65
N09S20	0.39	0.15	53.46	0.06	0.02	1.20	0.01	0	0	0	0.01	0.13	1.84
N09S21	0.38	0.12	53.63	0.05	0.01	1.09	0.01	0	0	0	0.00	0.09	1.65
N09S22	0.38	0.12	53.63	0.05	0.01	1.09	0.01	0	0	0	0.00	0.09	1.65
N09S23	0.36	0.09	53.80	0.04	0.00	0.98	0.00	0	0	0	0.00	0.06	1.46
N09S24	0.38	0.12	53.63	0.05	0.01	1.09	0.01	0	0	0	0.00	0.09	1.65

**Table 4.** Summary of the OSL ages for the samples collected from the trench site (NT-samples) and the site North (NA-samples) along the Nayband fault. Burial depth, radionuclide concentrations and estimated water content used to calculate the dose rates are given. The number of multi-grain aliquots (grain size 180-250  $\mu\text{m}$ ) contributing to the equivalent dose is denoted by ' $n$ '. Samples were opened under subdued red light. The light-exposed ends of each of tube samples were reserved for dose rate measurements using high resolution gamma spectrometry [Murray *et al.*, 1987]. The radionuclide activity concentrations were converted to dose rates using the factors given by Guérin *et al.* [2011] and the cosmic ray contribution to dose rate derived from Prescott and Hutton [1994]. One sample, NT-XXIII was sufficiently close to the surface for the conversion from concentration to gamma dose rate using these factors to be overestimated by  $\sim 12\%$ , but this only affects the total dose rate by 4%. This is unimportant compared to other uncertainties in the age calculation for this sample, and is neglected. The remainder of the samples not used for radionuclide measurements were wet sieved (180-250 $\mu\text{m}$ ) and acid cleaned in the usual manner, finally using concentrated HF for 40 min to give a clean quartz-rich fraction. Luminescence measurements used a Risø TLDA20 reader equipped with a blue LED (470 nm,  $\sim 80 \text{ mW.cm}^{-2}$  at the sample) stimulation source and photon detection through  $\sim 7 \text{ mm}$  U-340 glass filter [Bøtter-Jensen *et al.*, 2010]. The reader was equipped with a calibrated beta source delivering  $\sim 0.1 \text{ Gy.s}^{-1}$  to quartz mounted on stainless steel. Quartz was prepared for measurement by mounting as a  $\sim 8 \text{ mm}$  diameter monolayer of grains on stainless steel discs (9.7 mm diameter) using silicone oil. The luminescence purity of the quartz-rich fraction was confirmed using IR stimulation, no significant IR luminescence (compared to the blue-stimulated quartz signal) was detected. Measurement of quartz dose used a SAR protocol [Murray and Wintle 2000, 2003] with a 260°C preheat for 10 s, and a cut heat of 220°C. The sample was held at 125°C during optical stimulation. Standard dose recovery test undertaken on 14

samples, following blue light resetting room temperature, yielded an average ratio of measured to given dose (recycling ratio) of  $1.03 \pm 0.05$  ( $n=41$ ).

Sample	Risø code	Latitude (°N)	Longitude (°E)	Depth (cm)	Water content (%)	$^{238}\text{U}$ (Bq.kg $^{-1}$ )	$^{226}\text{Ra}$ (Bq.kg $^{-1}$ )	$^{232}\text{Th}$ (Bq.kg $^{-1}$ )	$^{40}\text{K}$ (Bq.kg $^{-1}$ )	Annual dose rate (Gy.ka $^{-1}$ )	$n$	Equivalent dose (Gy)	Age (ka)
NT-I	122910	31.91234	57.53061	31	0	16 ± 5	20.5 ± 0.4	23.6 ± 0.5	318 ± 8	2.06 ± 0.10	24	2.02 ± 0.14	0.98 ± 0.08
NT-II	112901	31.91234	57.53066	35	0	29 ± 8	25.9 ± 0.7	34.2 ± 0.8	510 ± 13	2.94 ± 0.14	22	2.18 ± 0.14	0.74 ± 0.06
NT-III	112902	31.91234	57.53066	103	0	24 ± 6	21.0 ± 0.5	25.5 ± 0.6	398 ± 10	2.30 ± 0.11	22	14.1 ± 0.4	6.1 ± 0.4
NT-IV	112903	31.91234	57.53066	121	0	19 ± 4	18.7 ± 0.4	22.1 ± 0.4	337 ± 8	2.00 ± 0.10	23	16.9 ± 0.7	8.4 ± 0.6
NT-V	112904	31.91234	57.53056	47	0	27 ± 5	17.9 ± 0.4	17.4 ± 0.4	258 ± 7	1.73 ± 0.08	24	9.7 ± 0.5	5.6 ± 0.4
NT-VI	112905	31.91234	57.53066	242	1	35 ± 5	22.3 ± 0.5	23.8 ± 0.6	388 ± 10	2.25 ± 0.11	23	39 ± 2	17.4 ± 1.3
NT-VII	112906	31.91234	57.53050	40	0	12 ± 5	21.8 ± 0.5	28.6 ± 0.6	423 ± 9	2.43 ± 0.11	26	1.92 ± 0.10	0.79 ± 0.06
NT-IX	112907	31.91234	57.53057	252	1	23 ± 4	23.2 ± 0.5	19.9 ± 0.4	218 ± 7	1.62 ± 0.08	18	114 ± 5	70 ± 5
NT-XI	112908	31.91234	57.53027	232	4	36 ± 8	29.1 ± 0.7	37.0 ± 0.8	659 ± 15	3.29 ± 0.15	22	13.4 ± 0.6	4.1 ± 0.3
NT-XII	112909	31.91234	57.53027	292	0	30 ± 6	22.9 ± 0.5	26.6 ± 0.6	440 ± 11	2.46 ± 0.12	26	16.6 ± 0.9	6.7 ± 0.5
NT-XIV	112910	31.91234	57.53027	322	0	16 ± 5	17.6 ± 0.4	18.3 ± 0.5	239 ± 7	1.56 ± 0.08	23	9.9 ± 0.5	6.4 ± 0.5
NT-XV	112911	31.91234	57.53027	314	0	25 ± 4	22.7 ± 0.4	20.7 ± 0.4	239 ± 6	1.70 ± 0.08	23	26.0 ± 1.0	15.3 ± 1.0
NT-XVIII	122911	31.91234	57.53066	197	1	32 ± 9	20.1 ± 0.7	22.4 ± 0.8	335 ± 11	2.06 ± 0.10	30	21.2 ± 1.3	10.3 ± 0.8
NT-XIX	122912	31.91234	57.53027	382	0	15 ± 5	17.0 ± 0.5	16.6 ± 0.4	212 ± 7	1.44 ± 0.07	36	28.4 ± 1.7	19.7 ± 1.6
NT-XX	132901	31.91234	57.53026	287	0	47 ± 6	26.6 ± 0.5	29.9 ± 0.5	470 ± 10	2.66 ± 0.13	15	16.8 ± 1.1	6.3 ± 0.5
NT-XXI	132902	31.91234	57.53028	308	0	19 ± 6	21.9 ± 0.6	22.0 ± 0.6	299 ± 9	1.83 ± 0.09	22	15.2 ± 0.7	8.3 ± 0.6
NT-XXII	132903	31.91234	57.53026	318	0	21 ± 5	18.0 ± 0.4	18.4 ± 0.5	240 ± 6	1.55 ± 0.08	28	11.3 ± 0.9	7.3 ± 0.7
NT-XXIII	132904	31.91234	57.53061	7	1	20 ± 6	21.1 ± 0.5	26.3 ± 0.6	379 ± 10	1.95 ± 0.09	12	0.13 ± 0.06	0.07 ± 0.03
NA-1	122905	32.03694	57.51797	170	0	16 ± 4	18.7 ± 0.4	20.2 ± 0.4	346 ± 9	2.00 ± 0.10	24	15.3 ± 0.6	7.7 ± 0.5
NA-2	122907	32.03638	57.52505	47	0	27 ± 5	24.1 ± 0.5	2.2 ± 0.4	35 ± 4	0.85 ± 0.05	39	18 ± 2	22 ± 3
NA-3	122906	32.04193	57.52502	50	0	26 ± 7	23.3 ± 0.6	15.0 ± 0.6	177 ± 7	1.50 ± 0.08	23	10.1 ± 0.8	6.8 ± 0.6

**Table 5.** Detailed description of stratigraphic units in Nayband trench. Units are designated from oldest (smaller number) to youngest (larger number); the letters e, f, w, and s refer to units exposed in the eastern section, the main fault zone, the western section, and sheared deposits, respectively.

Set	Unit	Eastern Section	Set	Unit	Main Fault Zone	Set	Unit	Western Section
		26 Cream to buff laminated clays with sparse sub-angular pebbles (2 per cent, 1-3 cm), with distributed mud-cracks on top.						
								25w Similar to 22w but without caliche fragments.
V e	1 6	Light brown, stratified, compact laminated clays in the upper part, including a laminated silty layer (5-6 cm thick) at the base, with few sub-angular pebbles (2 per cent, 1-2 cm).	IV	13f	Grey, laminated loose sands and silts thinning westward, scattered millimeter-thick caliche fragments in the upper part.	VI	24w	Light brown, liquefied coarse sands, including sandy dikes, with scattered fine pebbles (<1 cm).
		12f		Similar to 15e.	23w		Grey sandy dikes, with 1- to 7-cm width, containing coarse sands and scarce pebbles (<3 cm).	
		11f		Similar to 13e and 14e.	22w		Grey to light brown, stratified, sub-angular poorly-sorted pebbles and cobbles (75 per cent, 0.5-4 cm up to 12 cm), few inter-beds of laminated silts and clays in the middle, millimeter-thick caliche fragments in the upper 20 cm, loose clay, sand and silt matrix.	
V e	1 5	Light brown, stratified alternations of laminated loose silts and compact clays, with millimeter-thick caliche fragments as pale-colored fine grained calcite.	IV	10f	Grey to dark grey lenses of laminated coarse sands to fine pebbles (<1 cm).	VI		
	1 4	Similar to 13e but with caliche fragments in the upper part.		EROSION				
V e	1 3	Buff to light grey, laminated silty layer (5-7 cm) at the base overlain by compact clays.	III	9f	Similar to 7e.	VI	21w	Light brown to beige, stratified, sub-rounded, poorly- to moderate-sorted pebbles and cobbles (60 per cent, 0.5-3 cm up to 7 cm), calcite cement underneath the pebbles, thin inter-beds of laminated silts and clays, including some caliche fragments.
	1 2	Grey poorly- to well-laminated loose sands and silts, with few tiny-sub vertical clay-filled fractures.		8f	Grey, finely-laminated loose sands and silts with sparse pebbles (5 per cent, 0.5 cm).		20w	Light brown, compact silts and clays, fairly stratified, few sub-angular pebbles (2 per cent, 1-2 cm), with a laminated silty layer 5-6 cm (bottom) and compact laminated clays (top).
I V e	1 1	Cream to buff, stratified, a very thin (3-5-cm thick) silty layer at the base overlain by compact clays.	III	7f	Light brown compact clays and silts, fairly stratified, containing poorly-sorted scattered pebbles and cobbles (5 per cent, 0.5-2 cm up to 7 cm).	VI		
	1 0	Light grey laminated sands and silts.		6f	Similar to 5f, containing sub-angular poorly-sorted fining-upward pebbles and cobbles (60			



I I	5e	Grey to buff alluvial deposits, fairly stratified to stratified, sub-angular, poorly- to moderate-sorted pebbles (70 per cent, 0.5-2 cm up to 6 cm), with silt and clay matrix and some carbonate cement, with erosion surface at the base.		2f	Cream to light brown, stratified, alternations of silts and clays, laminated in silty beds, few scattered coarse pebbles (2-4 cm) in the middle part, compact 5-6-cm thick carbonate caliche on top.		9w	Cream to buff, compact beds of silts (6-8-cm thick in the lower part) and clays.
				1f	Cream to light brown, fairly stratified, very compact clays.	EROSION		
I I	4e	Cream to light brown alternations of poorly-laminated loose silts and compact clays.	Sheared Deposits	4s	Light brown to cream, including pieces of units 1f to 5f and 1e to 6e, sub-angular pebbles and cobbles (10 percent, 0.5-1 cm up to 8 cm), oriented thin lenses of clay and silt parallel to the fault planes, with compact clay, silt and sand matrix.	IV	8w	Grey to dark grey alluvial deposits, stratified (thin-bedded to laminated in the upper part), inter-bed of clay (4-5-cm thick) in the middle of the unit, with sub-rounded, poorly- to moderate- sorted fining-upward pebbles (5-30 per cent, 0.5-1 cm up to 2 cm), calcite cement in matrix.
						7w	Grey to dark grey, lens of laminated coarsening upward loose sands to fine pebbles (<1 cm).	
						III	6w	Grey, liquefied sands, with fine pebbles (5-15 per cent, <1 cm) mostly at the pocket's margins.
							5w	Undifferentiated units 3w and 4w.
							4w	Light cream to buff, stratified, compact silt (bottom) and clay (top).
		3e		Cream, laminated loose silts.		3s	Grey to light brown, sub-angular, poorly-sorted coarsening-upward pebbles (40-60 per cent, 0.5-2 cm up to 6 cm), oriented clasts parallel to the bounding fault planes, with clay, silt and sand matrix.	
	2e	Cream to light brown, stratified, alternations of silts and clays, laminated in silty parts, with few scattered coarse pebbles (2-4 cm).		2s	Similar to 1s, with poorly- to moderate-sorted pebbles (10-15 per cent, 0.5-1 cm up to 3cm).	II	2w	Grey, thin-bedded to laminated alluvial deposits, parallel to discontinuous wavy beds (mostly in lower part), containing sub-rounded, moderate- to well-sorted pebbles (70 per cent, 0.5-1 cm), with erosion surface at the base.
	1e	Cream to light brown, fairly stratified, very compact clays, few sparse sub-angular coarse pebbles (up to 5 cm) in the lower part.		1s	Beige, including sub-rounded, poorly-sorted pebbles (20-30 per cent, 0.5-2 cm up to 5 cm), oriented clasts parallel to the bounding fault planes compact sand, clay and silt matrix.	I	1w	Light brown to buff, stratified, fine-grained matrix- supported sediments, containing sub-rounded, poorly- to moderate- sorted pebbles (10 per cent, 0.5-1 cm up to 5 cm), calcite cement in part, with clay, silt and sand matrix.